ABSTRACT

TRICHY, GOPINATH. Growth, Characterization and Magnetic Properties of Epitaxial FePt Nanostructures. (Under the direction of Prof. Jagdish Narayan).

The primary objective of this dissertation was to study the growth, microstructure and magnetic properties of FePt nanostructures so as to demonstrate their suitability for high-density magnetic storage applications. The FePt system is an attractive candidate for high-density storage (greater than 100 Gbits/in^2) due to its extremely high uniaxial magnetocrystalline anisotropy (K_u = 7.0 $\times 10^7$ erg/cm^3). The high magnetocrystalline anisotropy permits the use of smaller particles before the onset of superparamagnetism; this directly leads to larger recording densities. As a part of this study, we have pioneered the epitaxial growth of c-axis FePt on single crystal Si (100) substrates. This holds tremendous future promise in terms of integration of our magnetic structures with the existing Si-based technology. Integration of FePt on Si (100) was achieved by using epitaxial TiN as a template buffer. The TiN template controls the FePt growth along the magnetically hard c-axis and it also acts as an effective diffusion barrier. The FePt/TiN/Si (100) heterostructure was synthesized using pulsed laser deposition. X-ray diffraction results showed strong c-axis growth and significant $L1_0$ order. Transmission electron microscopy revealed the following epitaxial relationship; FePt (001) <001>$\|$TiN (100) <001>$\|$Si (100) <001>. In spite of the large misfit strains (ε) involved ($\varepsilon_{FePt/TiN}$ = 9.5 % and $\varepsilon_{TiN/Si}$ = 22 %), epitaxy was achieved in the FePt/TiN/Si heterostructure by the unified paradigm of domain matching epitaxy (DME).

In this work FePt was synthesized both as continuous thin films and individual discrete nanoparticles. The effect of microstructure on magnetic properties of the epitaxial FePt system was studied in detail. The microstructure was progressively varied from a 9 nm nanoparticle system to a 30 nm thick continuous film. Magnetic hysteresis measurements showed that all the samples were predominantly perpendicularly magnetized with higher coercivity, squareness and remanence when compared to the in-plane loops. The individual nanoparticles, being in a single domain state, showed higher coercivity than the continuous thin film. Within the nanoparticle regime coercivity increased with increasing particle size. The highest coercivity of 13,500 Oe was obtained for a bead-like microstructure, when the individual nanoparticles just begin to merge to form a continuous thin film. The continuous thin film showed least coercivity because of its multi-domain state and lack of defects or pinning sites. The best microstructure in terms of magnetic storage was the 18 nm sized nanoparticle system, with a perpendicular coercivity of 10,000 Oe. For this system, if we assume one bit of information to be stored in each nanoparticle, a storage capacity of 1 Terabit/in^2 can be realized. All the samples under study showed perpendicular hysteresis loops with remarkable squareness (≥ 0.95). The coercivity of the FePt system can also be controlled via the composition. For the 18 nm system, the perpendicular coercivity was decreased from 10,000 Oe to 3,200 Oe by changing the composition from $Fe_{50}Pt_{50}$ to $Fe_{41}Pt_{59}$. A negative magnetoresistance (MR) of 0.57 % was observed at room temperature for the $Fe_{50}Pt_{50}$ bead-like thin-film system. The MR loops showed hysteretic behavior with maximum resistance at H_c. The values of coercivity in the MR and MH measurements were consistent. The presence of MR in the

FePt system was attributed to thin domain walls, whose thickness is comparable to spin diffusion lengths. The negative MR effect was explained based on spin and domain wall dependent electron scattering.

Growth, Characterization and Magnetic Properties of Epitaxial FePt Nanostructures

by

Gopinath R Trichy

A dissertation submitted to the graduate faculty of
North Carolina State University
in partial fulfillment of the
requirements for the Degree of
Doctor of Philosophy

Materials Science and Engineering

Raleigh, North Carolina

2008

APPROVED BY:

Prof. J. Narayan
Chair of Advisory Committee

Prof. J. T. Prater

Prof. R. O. Scattergood

Prof. V. Misra

DEDICATION

Dedicated to my parents

BIOGRAPHY

Gopinath Trichy was born and brought up in Hyderabad, a bustling city in the southern part of India. He completed his primary schooling at the Hyderabad Public School. He later attended the Little Flower Junior College from where he graduated high school with flying colors. His interest in mathematics and sciences prompted him to enroll into the Jawaharlal Nehru Institute of Technology, where he pursued a Bachelor's Degree in Engineering in the field of Metallurgy and Materials Technology. He completed the B.Tech. degree in 2002 with high distinction. In the fall of 2002, he entered a Master of Science program at North Carolina State University in Materials Science and Engineering. For his masters he worked on the mechanical properties of nanostructured materials under the guidance of Prof. Scattergood. In the spring of 2005 he joined the NSF Center for Advanced Materials and Smart Structures at NCSU to work towards his PhD with Prof. Jagdish Narayan.

ACKNOWLEDGEMENTS

First, I would like to thank my research advisor Prof. Jagdish Narayan for his guidance and support during this work. His discipline and commitment towards research have left lasting impressions on me. At times when I was less than motivated, his words of wisdom would always put me back on track. Big thanks to Prof. Narayan for my professional success. I sincerely thank my co-advisor Dr. J. T. Prater. His suggestions and advice during the weekly research group meetings were of immense help and have contributed to the successful completion of this project. I would also want to thank him for his patience in editing and correcting most of my written work. Thanks to Dr. Scattergood for serving on my committee. He was also my master's advisor and association with him has been a pleasant experience throughout. Special thanks to Dr. V. Misra, the minor representative on my committee, her comments were of great help.

I am grateful to Dr. Zhou, this work would not be possible without her help. The decision to work on the FePt system for my PhD was in-part her idea. She even trained me on most equipments in the lab. Special thanks to Dr. Ramachandran, from whom I learnt a lot about magnetic measurements. Scientific discussions with him have always been informative. Dr. Bhosle and Dr. Chugh need a special mention for their help in the lab. I would also like to thank Dr. Chakraborti, collaborations with him have been extremely fruitful. I thank Dr. Sudhakar for useful scientific discussions. I sincerely thank other members of the group, T. Dutta, W. Wei, R. Aggarwal, P. Pant and C. Jin.

I thank Dr. Shultz (Department of Chemistry) for providing access to the SQUID for magnetic measurements. Thanks to Dr. Kumar at NCA&T for providing access to the PPMS required for magnetoresistance measurements. I acknowledge Dr. Parikh at UNC for RBS measurements. Thanks to Dr. Rawdanowicz because of who the TEM was always kept running and readily accessible. Thanks to Ms. Deas for her help with the administrative work.

I would like to thank my parents, Rajagopal Trichy and Mohana Chandrashekar. I acknowledge their unconditional love, support and encouragement. I owe my well-being and success to them. My sister, Soujanya Trichy, has backed me at all times. Special thanks to my brother, Narasimhan Trichy. He has been a constant motivator and I acknowledge his support and advice.

This research was funded by the National Science Foundation.

TABLE OF CONTENTS

LIST OF TABLES

LIST OF FIGURES

Chapter 1

1 Introduction

Over the past couple of decades there has been an ever increasing demand for digital information storage. To cope with this need, hard disks with minimum size are required to store maximum information. With the current technology, that uses CoCrPt as the recording medium and a longitudinal magnetic recording format, one can get to areal densities as high as 100 Gbit/in^2. To get beyond this limit (and up to 1 Tbit/in^2), we have to look for new materials and improved recording techniques. The FePt system is an attractive candidate for high-density storage due to its extremely high uniaxial magnetocrystalline anisotropy (K_u = 7.0 $\times 10^7$ erg/cm^3). The high magnetocrystalline anisotropy permits the use of nano-sized particles before the onset of superparamagnetism; this directly leads to larger recording densities. Additionally, the c-axis aligned FePt system is well suited for perpendicular recording. A four-fold increase in storage density can be realized by employing the perpendicular magnetic recording technique.

Importance of the FePt material system

The $L1_0$ ordered FePt material system is a promising candidate for magnetic storage and recording applications owing to its excellent properties including, high uniaxial magnetocrystalline anisotropy, high coercivity, high saturation magnetization and good chemical stability [1]. In order to achieve areal densities beyond the 100 Gbit/in^2 regime, the grain size has to be reduced to the nano regime. Below a critical size superparamagnetism takes over, i.e. the magnetization of the particle becomes unstable due to thermal fluctuations rendering the system unsuitable for permanent magnetic storage [2]. The high anisotropy of the FePt system increases the anisotropy energy (K_uV) and permits the use of smaller particles (down to 3 nm) before the onset of superparamagnetism. Therefore, use of FePt as a magnetic storage media can improve areal density.

For magnetic storage one requires a square hysteresis loop, with two distinct states of magnetization (0 and 1), that can switch at well defined fields. This is usually achieved by manipulating the magnetic anisotropy of the material. Magnetic anisotropy originates from several factors such as the crystal structure, shape and stress [3]. Since the FePt system has extremely high crystalline anisotropy, this factor is used to achieve good squareness in the hysteresis loops. For the FePt system the crystalline anisotropy is a maximum along the c-axis. Hence to use FePt as a magnetic storage media, one needs to synthesize c-axis oriented single crystalline FePt structures. Texture in any other orientation will yield hysteresis loops that are not square and hence will not switch at well defined fields. If the structure is polycrystalline, the crystalline anisotropies of individual grains will be randomly dispersed and the magnetic loop will be far from square (undesirable for magnetic storage). The c-axis oriented (001) FePt structures are also suitable for perpendicular magnetic recording. Perpendicular recording is characterized by improved areal density and minimal demagnetizing fields [4]. It also provides an approach to grow long columnar grains that have the capability to delay onset of superparamagnetism.

Importance of size reduction

Reducing the size of the magnetic grains improves areal density, i.e. a greater number of bits can be packed in a given area. In recent years considerable attention has been focused on the synthesis and study of magnetic nanoparticles for high-density magnetic recording applications [5-7]. Interesting properties are observed when the dimensions of magnetic particles are tailored to sizes comparable with the characteristic magnetic length scales such as magnetic exchange length and domain-wall width [8,9]. For the purpose of magnetic storage, size reduction and the transition to single domain state manifests favorable changes in coercivity, remanence and domain reversal mechanisms.

In order to be used for storage, magnetic particles are required to have uniformity in size, composition and crystallographic orientation. Also, the magnetic particles need to be well-separated to minimize exchange coupling and improve the signal to noise ratio. In such systems, each particle will have the capability to store one bit of information. In the case of continuous magnetic media, data is stored as bits (zeros and ones) in magnetic patches, which may contain a number of magnetic grains. It is important to realize that the demagnetizing fields of neighboring patches can interfere with each other [3]. When scaled to nanoregime (to improve areal density), the spin of a bit can be flipped by its oppositely aligned neighbor. Hence, the bits need to be magnetically isolated. One approach would be to synthesize physically isolated magnetic nanoparticles. In such a case, each particle will be a single domain and it will have the capability to switch independently, without any interference from its neighbor [10].

Our approach

This dissertation focuses on the growth, characterization and magnetic properties of epitaxial FePt nanostructures for high-density magnetic storage applications. FePt was synthesized both as continuous thin films and individual discrete nanoparticles. Here, it is worth mentioning that in this study the nanoparticles are also referred to as nanoislands or nanodots. As a part this study, we have pioneered the epitaxial growth of c-axis FePt on single crystal Si (100) substrates.

Until now single crystal MgO coupons have been largely used as the substrate for epitaxial growth of FePt [11 and references therein]. However, MgO will be unsuitable from a viewpoint of practical applications, due its high single-crystal cost, limited wafer size, hygroscopic nature and poor mechanical strength. The unique feature of our study stems from the usage of Si (100) as the substrate. This holds tremendous future promise because Si is the base material of the microelectronics industry and its usage facilitates potential integration of our magnetic structures with present day microelectronic/nanoelectronic devices.

The FePt system has been synthesized by a wide variety of processing techniques in various forms including: epitaxial thin films [11,12], textured non-epitaxial films [13] and nanoparticles/islands [5,6]. Some popular synthesizing techniques used are; sputtering [11,12], MBE [14,15] and chemical synthesis [5,16]. Each technique has its own advantages and disadvantages in terms of the resulting morphology and crystallographic orientation. For example, nanoparticles have been successfully synthesized by chemical routes (with uniform size) [5] and ion implantation [17], but such techniques do not offer control over orientation, which is of prime importance if one has to exploit the magnetocrystalline anisotropy of the system. It is important to realize that physical vapor deposition methods based on substrate controlled epitaxy are more suitable for synthesizing crystallographically oriented FePt nanostructures. In this work, pulsed laser ablation was employed to synthesize different forms of FePt nanostructures. Pulsed laser deposition (PLD) is a high energy non-equilibrium processing technique, where the energy of the ablated species can be as high as 10-100 eV [18]. This feature affords several advantages, including the ability to form novel phases, and to reduce processing temperatures. Accordingly, we have shown that we can synthesize FePt with significant $L1_0$ order at a low processing temperature of 500 ° C. It is important to reduce ordering temperature (thermal budget) from an application point of view.

Scientific challenges during growth

Integration of FePt on Si (100) was achieved by using epitaxial TiN as a template buffer. Insertion of TiN as the template buffer leads to FePt growth oriented along the magnetically hard [001]. TiN also acts as a diffusion barrier between FePt and Si. The synthesis of the heteroepitaxial FePt/TiN/Si (100) structure poses a great challenge because of the large lattice misfit strains (ε) involved, ε (FePt/TiN) = 9.5 % and ε (TiN/Si) = 22 %. Epitaxy in such large mismatch systems was achieved by domain matching epitaxy (DME) [19]. Within each domain, integral multiples of lattice planes match across the film-substrate interface and the domains themselves are separated by dislocations. In the case of the FePt/TiN system, 10/9 and 11/10 domains alternate (with a frequency factor of 0.547) to accommodate the 9.5 % misfit. Here, by a 10/9 domain we mean that 10 planes of FePt match with 9 planes of TiN and similarly in the 11/10 domain, 11 planes of FePt match with 10 planes of TiN. Epitaxy of TiN on Si, which has a 22% misfit, was achieved by alternating 3/4 and 4/5 domains with equal frequency [19].

The rest of the dissertation is presented in the following six chapters.

Chapter 2: This chapter presents the background knowledge relevant to this study.

Chapter 3: This chapter outlines the experimental techniques used in this study.

Chapter 4: This chapter presents the growth, characterization and magnetic properties of the off-stoichiometric $Fe_{41}Pt_{59}$ continuous thin films. DME of the FePt/TiN system is discussed in detail. Magnetic properties as a function of growth temperature are also discussed.

Chapter 5: This chapter presents results pertaining to the growth of $Fe_{41}Pt_{59}$ nanoparticles. Extensive TEM results are presented to study the epitaxy, $L1_0$ order, morphology and Volmer-Weber growth of the nanoparticles. Magnetic properties of the nanoparticles are investigated and compared with continuous thin films.

Chapter 6: This chapter discusses the effect of microstructure on the magnetic properties of the $Fe_{50}Pt_{50}$ system. The microstructure was progressively varied from a 9 nm nanoparticle system to a 30 nm thick continuous thin film. Magnetic properties of an equiatomic $Fe_{50}Pt_{50}$ system was compared with an off-stoichiometric $Fe_{41}Pt_{59}$ system.

Chapter 7: The magnetoresistance behavior of the FePt system was investigated in this chapter. Magnetoresistance was studied as a function of temperature and orientation of field and current.

References

1. D. Weller, A. Moser, L. Folks, M. E. Best, W. Lee, M.F. Toney, M. Schwickert, J. U. Thiele, and M.F. Doerner, IEEE Trans. Magn. **36**, 10 (2000).
2. B. D. Cullity, *Introduction to Magnetic Materials*, Addison-Wesley, Readings, MA 1972.
3. N. A. Spaldin, Magnetic materials: Fundamentals and device applications, Cambridge University Press (2003).
4. K. Ouchi and N. Honda, IEEE Trans. Magn. **36**, 16 (2000).
5. S. Sun, C.B. Murray, D. Weller, L. Folks, and A. Moser, Science, **287**, 1989 (2000).
6. J.A. Christodoulides, Y. Huang, Y. Zhang, G. C. Hadjipanayis, I. Panagiotopoulos, D. Niarchos, J. Appl. Phys. **87**, 6938 (2000).
7. Mu-Gyeom Kim, Sung-Chul Shin, Kyongha Kang, Appl. Phys. Lett. **80**, 3802 (2002).
8. R. H. Kodama, J. Magn. Magn. Mater. **200**, 359 (1999).
9. O. Fruchart, J. P. Nozieres, W. Wernsdorfer, and D. Givord, Phys. Rev. Lett. **82**, 1305 (1999).
10. M. Albrecht, C. T. Rettner, A. Moser, M. E. Best, and B. D. Terris, Appl. Phys. Lett. **81**, 2875 (2002).
11. K. Barmak, J. Kim, L.H. Lewis, K.R. Coffey, M.F. Toney, A.J. Kellock, and J.U. Thiele, J. Appl. Phys. **98**, 033904 (2005).
12. F. Casoli, F. Albertini, L. Pareti, S. Fabbrici, L. Nasi, C. Bocchi, and R. Ciprian, IEEE Trans. Magn. **41**, 3223 (2005).

13. H. Zeng, M.L. Yan, N. Powers, D.J. Sellmyer, Appl. Phys. Lett. **80**, 2350 (2002).
14. R.F.C. Farrow, D. Weller, R.F. Marks, M.F. Toney, D.J. Smith, M.R. McCartney, J. Appl. Phys. **84**, 934 (1998).
15. T. Itoh, T. Kato, S. Iwata, S. Tsunashima, IEEE Trans. Magn. **41**, 3217 (2005).
16. Z. Jia, S. Kang, S. Shi, D.E. Nikles, J.W. Harrell, M. Shamsuzzoha, J. Appl. Phys. **99**, 08E904 (2006).
17. C.W. White, S.P. Withrow, K.D. Sorge, J.D. Budai, J.R. Thompson, and L.A. Boatner, J. Appl. Phys. **93**, 5656 (2003).
18. R. K. Singh and J. Narayan, Phys. Rev. B **41**, 8843 (1990).
19. J. Narayan, and B.C. Larson, J. Appl. Phys. **93**, 278 (2003).

Chapter 2

2 Related background knowledge

2.1 Magnetism

2.1.1 Magnetic materials and their classification

Most materials can be classified as ferromagnets, paramagnets and diamagnets depending upon their response in a magnetic field [1,2]. The response to a magnetic field is recorded as a plot of M versus H, called the magnetization curve. Here, M is the magnetization (emu/cm^3) and H is the external magnetic field (Oe). Figure 2-1 shows MH plots for ferromagnetic, paramagnetic and diamagnetic materials [3].

Ferromagnetism

Ferromagnetic materials have the ability to get magnetized due to the presence of an external magnetic field, and importantly they remain magnetized (for a certain period of period of time) even after the external field is removed. In the magnetized state the domains in the material orient themselves along the magnetic field direction and give rise to a net magnetic moment [1,2]. In the unmagnetized state the magnetization vectors of the individual domains are randomly oriented and hence net magnetic moment is zero. It is important to realize that within a domain the individual atomic dipole moments are aligned parallel to each other contributing to a net magnetic moment. Depending upon the distance between individual atomic moments in a lattice, the exchange interaction aligns the atomic moments parallel or anti parallel to each the other. If the individual atomic dipole moments are aligned parallel then it results in ferromagnetism. Antiferromagnetism results from an anti-parallel arrangement. When the temperature is increased thermal agitation destroys the parallel arrangement of the atomic dipole moments. Hence above a certain temperature, called the Curie temperature (T_c), ferromagnets become paramagnets. In case of ferromagnetic materials magnetization increases nonlinearly with field and saturates above a certain field (see Fig 2-1). These materials are associated with large magnetization values and large and positive susceptibility (χ).

$$\chi = M / H \tag{1}$$

Paramagnetism

In paramagnets the atomic moments are weakly coupled to each other. In presence of the magnetic field these individual moments align with the field resulting in a net magnetic moment. When the field is removed the atomic dipoles orient themselves randomly due to thermal agitation and the net magnetic moment becomes zero. Magnetization increases linearly with applied field. Susceptibility is small and positive (see Fig. 2-1). A material in a paramagnetic state follows the Curie-Weiss law [1,2]. This law takes into account both the localized moment theory and the interaction between atomic moments [1,2]. The Curie-Weiss law is given as,

$$\chi = C / (T-\theta) \tag{2}$$

Where C is a material constant called the Curie constant and T is the temperature. For $\theta = 0$, the Curie-Weiss law reduces to the Curie law. According to the Curie law, an increase in temperature causes thermal agitation and alignment of the magnetic moments becomes difficult resulting in reduced susceptibility. When $\theta \neq 0$, there exists interaction between individual magnetic moments and the material is paramagnetic only above the transition temperature θ. Below the transition temperature the material shows ferromagnetism [1,2].

Diamagnetism occurs in materials that have no net magnetic moment as a result of their atomic shells being completely filled. Diamagnets have small and negative susceptibility. In antiferromagnets the individual magnetic moments interact and adjacent moments are aligned anti-parallel to each other. Just like the paramagnets in case of the antiferromagnets, magnetization varies linearly with field and the susceptibility is small and positive. The above discussion is summarized in Fig. 2-1.

Type of Magnetism	Susceptibility	Atomic / Magnetic Behaviour		Example / Susceptibility	
Diamagnetism	Small & negative.	Atoms have no magnetic moment	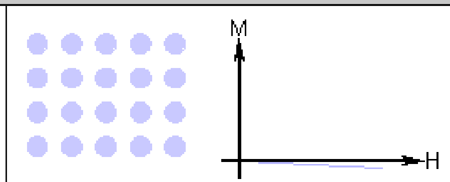	Au Cu	-2.74x10^{-6} -0.77x10^{-6}
Paramagnetism	Small & positive.	Atoms have randomly oriented magnetic moments	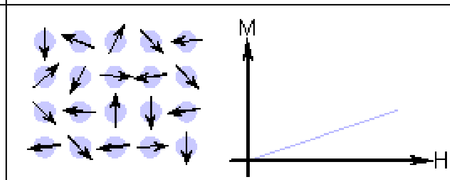	β-Sn Pt Mn	0.19x10^{-6} 21.04x10^{-6} 66.10x10^{-6}
Ferromagnetism	Large & positive, function of applied field, microstructure dependent.	Atoms have parallel aligned magnetic moments	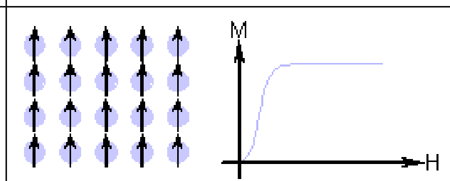	Fe	~100,000
Antiferromagnetism	Small & positive.	Atoms have mixed parallel and anti-parallel aligned magnetic moments	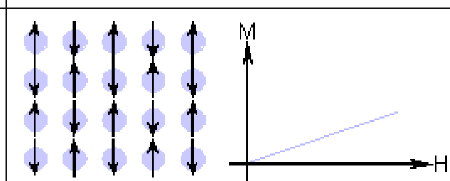	Cr	3.6x10^{-6}
Ferrimagnetism	Large & positive, function of applied field, microstructure dependent	Atoms have anti-parallel aligned magnetic moments	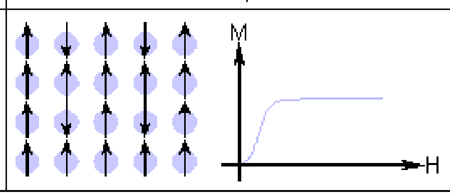	Ba ferrite	~3

Figure 2-1. Classification of materials based on their response to an applied magnetic field [3].

2.1.2 The MH loop: Hysteresis curve

When a magnetic field is applied to a ferromagnetic material, its magnetization increases non-linearly and finally saturates above a certain field. A typical hysteresis curve for a ferromagnetic material is shown in Fig. 2-2. The curve from zero magnetization to saturation is called the virgin curve. In the initial part of the virgin curve, small changes in field lead to large changes in magnetization. Beyond saturation, increase in field does not effect magnetization to a great extent. The saturation magnetization is denoted by the point M_s on the hysteresis curve (see Fig. 2-2). It is important to realize that M_s is a material property and does not change with microstructure [1,2]. But the field at which saturation occurs is microstructure dependent. After saturation, when H is decreased in the opposite direction, the magnetization follows a different path. This implies that the system shows hysteresis. The magnetization that remains at zero field is called remanence. It is denoted by the point M_r on the hysteresis curve (see Fig. 2-2). The reverse field required to bring back the system to zero magnetization is called the coercivity (H_c). When the field is decreased further, saturation is achieved in the negative direction. When the magnetic field is applied through all the five quadrants, the complete hysteresis curve is obtained. Depending upon the coercivity, ferromagnetic materials are generally classified as hard and soft magnets. Hard magnets are associated with large coercivity and they saturate at high fields. Soft magnets saturate at low fields and have low coercivity. The squareness of the hysteresis loop is an important factor for magnetic storage applications. Generally, the squareness is evaluated as the ratio of remanence (M_r) and the saturation magnetization (M_s).

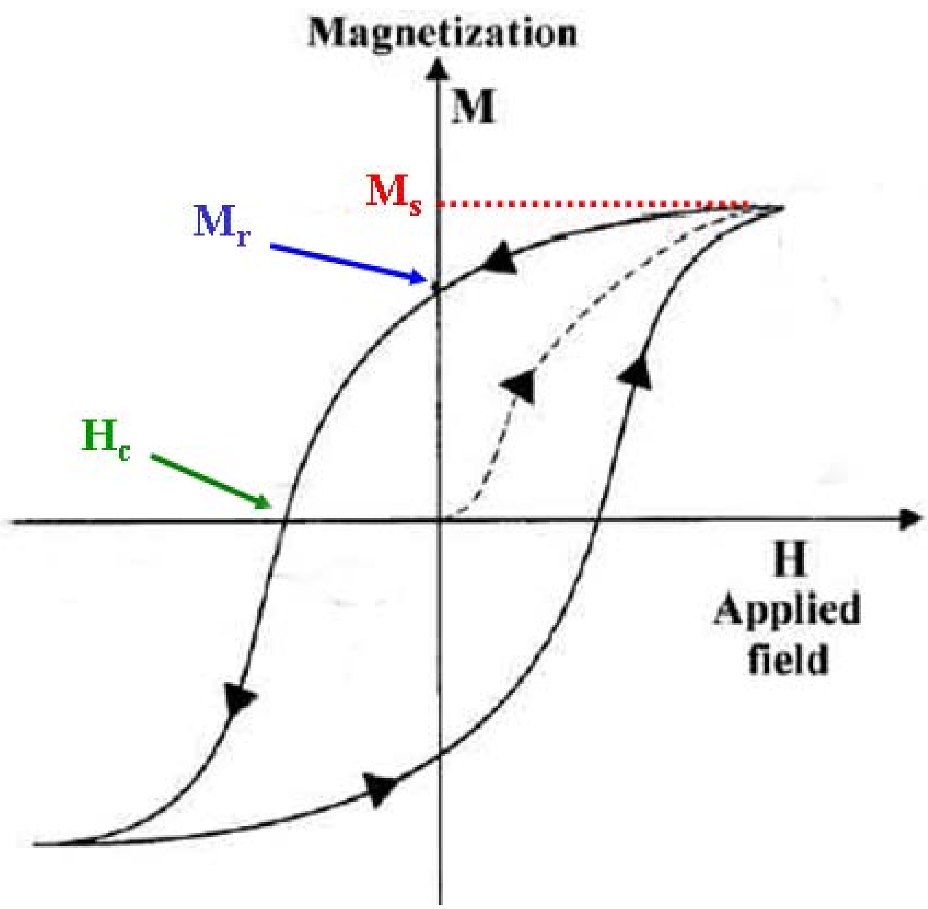

Figure 2-2. Typical hysteresis curve for a ferromagnetic material.

2.1.3 Magnetic domains

Domains are formed in a ferromagnetic system so as to minimize the total magnetic energy [1,2]. The main components of magnetic energy that govern domain formation are the exchange energy, the magnetostatic energy and the magnetocrystalline energy. Exchange energy tends to align the atomic dipole moments (or electron spins) parallel to each other [1,2]. Exchange energy prefers the formation of one large domain with all the dipoles aligned parallely. However, a ferromagnetic material containing one large single domain will have large magnetostatic energy rendering the system unstable. Magnetostatic energy is associated with opposing demagnetizing fields (see Fig. 2-3). Domain formation occurs in order to reduce these demagnetizing fields as shown in Fig. 2-3b and Fig. 2-3c [2]. Figure 2-3c shows a domain pattern with zero magnetostatic energy (i.e. no magnetic poles exist). It is important to realize that at the boundary between two domains the magnetic moments are not parallel to each other. This means an increase in exchange energy. So domain formation involves a balance between competing exchange and magnetostatic energies. The other important factor involved in domain formation is the magnetocrystalline energy. Ferromagnetic crystals have preferred easy axis magnetization directions. The domains tend to form along these easy axis directions in order to minimize the energy of the system. For example, in case of bcc iron which has <100> as the easy axis direction, the domain arrangement shown in Fig. 2-3c will have minimum magnetocrystalline energy [2]. Within the boundaries of the domains the direction of magnetization changes through the hard axis. Hence magnetocrystalline energy prefers large domains, with minimum domain boundaries. It is also important to note that width of the domain wall depends on the balance between exchange energy and the magnetocrystalline energy. Exchange energy prefers wider walls, whereas magnetocrystalline energy prefers narrow walls [1,2].

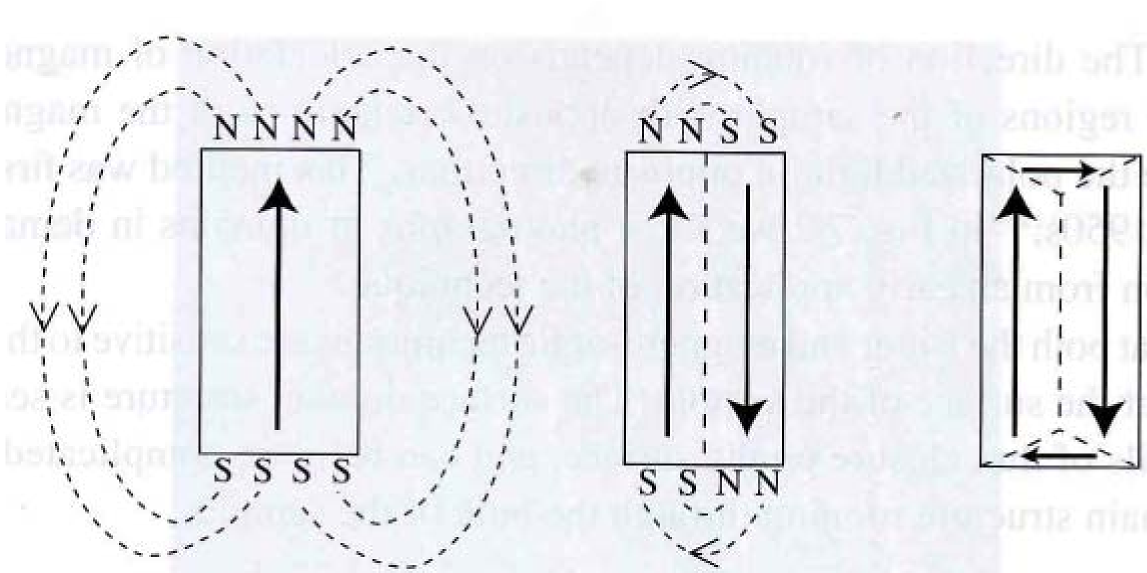

(a) (b) (c)

Figure 2-3. Formation of domains in a magnetized block to minimize the magnetostatic energy [2].

2.1.4 Single domain state

Single domains exist at a critical size below which it is energetically unfavorable to form multi-domains. The balance between exchange energy and magnetocrystalline energy yields typical domain wall widths of about 100 nm [1,2]. So if a system consists of particles sized below 100 nm, they assume single domain character simply because a domain wall cannot fit inside. Interesting properties are observed when the dimensions of magnetic particles are tailored to sizes comparable with the characteristic magnetic length scales like magnetic exchange length and domain-wall width [4-6]. Inherent properties of a magnetic system such as saturation magnetization, Curie temperature, anisotropy and domain reversal are affected due to reduction in size [4]. For the purpose of high density magnetic storage, the most relevant property that is associated with size reduction is the transition to single domain state that manifests changes in coercivity, remanence and domain reversal mechanisms.

Generally, a single domain state is associated with a higher coercivity than the multi-domain state [1,2]. In a demagnetized state, the magnetization of a single domain will be oriented along its easy-axis direction. Now if a field is applied in the opposite direction, magnetization reversal takes place by rotation of the magnetization vector through the hard direction. It is important to realize that this rotation of the magnetization vector through the hard axis is difficult since it has to overcome the strong anisotropic forces that hold the spin along the easy direction. In comparison, magnetization reversal by domain wall motion in a multi-domain state is much easier. Hence a system in a single domain state shows higher coercivity than a multi-domain configuration. Figure 2-4 is a schematic showing the variation of coercivity with particle size [1]. In a multi-domain state the coercivity increases with decreasing particle size. Maximum coercivity is realized when the system changes from a multi-domain to a single domain state, the point D_s in Fig. 2-4. Within the single domain state, coercivity decreases with decrease in particle size. Finally, below particle size D_p, superparamagnetism prevails and the system shows zero coercivity. The phenomenon of superparamagnetism happens when the anisotropy energy (K_uV) of the system becomes less than the thermal energy (kT). In such a situation the spins flip randomly instead of staying fixed. Here, K_u is the anisotropy constant and V the volume of the particle. For the purpose of magnetic storage, one would like to be in the single domain regime so that the system has high coercivity. A high coercivity implies that data can be stored for a longer duration. Also, for high coercivity materials small bit sizes can be stabilized leading to improved areal density [2].

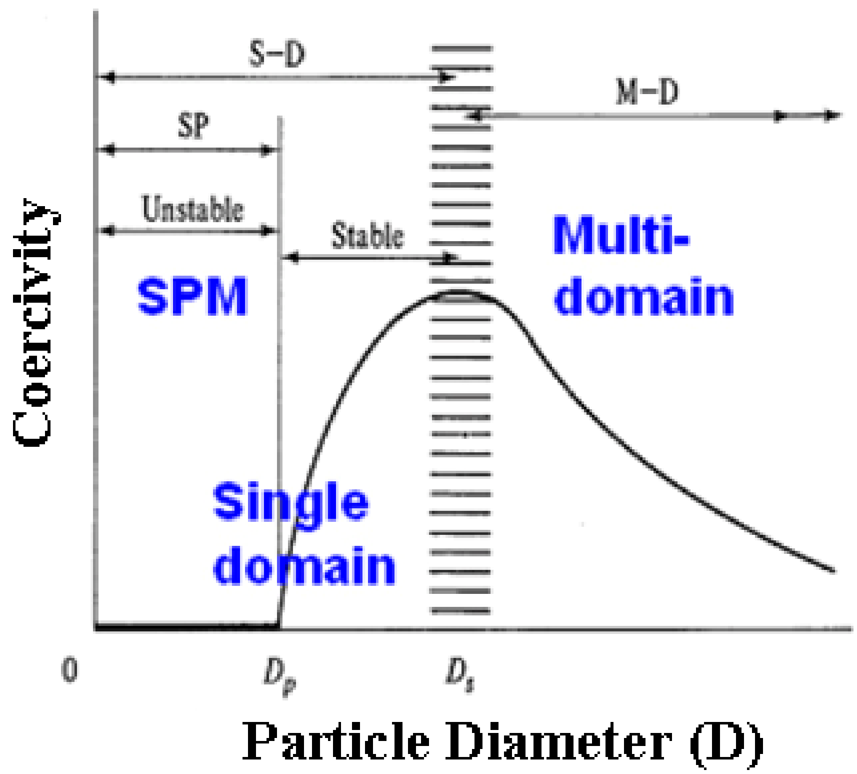

Figure 2-4. Variation of coercivity with particle size [1].

2.1.5 Magnetocrystalline anisotropy

The total energy in a single domain state is dependent on the magnetization vector direction. The system has lowest energy when the magnetization vector is oriented along the easy direction. External energy has to be provided in order to overcome the anisotropic energy barrier and orient the magnetization vector along a hard direction [1,2]. The anisotropic energy for a system is given as,

$$E = -K_u V \cos^2\theta \quad (3)$$

Where K_u is the anisotropy constant, V is the volume, and θ is the angle between magnetization vector and easy direction. From this equation it is clear that the system has least energy when the magnetization vector is parallel to the easy direction. Anisotropy originates in small magnetic particles mainly from the crystal structure, shape and stress [1,2]. In this study we are primarily concerned with the magnetocrystalline anisotropy and will discuss it further.

Magnetocrystalline anisotropy originates from the crystal structure. It can be understood as a tendency of the magnetization vector to align itself along a preferred crystal direction. For example in fcc materials, <111> is the easy axis and <100> is the hard axis direction. For bcc the easy axis direction is <100> and for hcp materials it is <0001> [2]. The magnetocrystalline anisotropy originates from the spin-orbit-lattice coupling. An externally applied field that tries to reorient the electron spin along a hard axis, faces resistance from the orbital state of the spin which is strongly coupled to the neighboring atoms of the lattice [1,2].

The magnetocrystalline anisotropy greatly affects the hysteresis curve. Figure 2-5 shows schematic hysteresis loops along the easy and hard-axis direction for a single domain system. The easy-axis loop has higher coercivity, remanence and squareness when compared to the hard-axis loop. The orientation of the magnetization vectors in the demagnetized and saturation state are also shown in Fig. 2-5. In the demagnetized state, the spins are oriented along the easy axis such that they cancel out each other. When a field is applied along the easy axis we obtain a square hysteresis loop (shown in red color). At saturation the spins are aligned parallel to the field direction which is also the easy direction. Very little energy is required to get from an unmagnetized spin configuration to a saturation spin configuration. Hence the easy-axis loop saturates at low fields. The saturation spin state is a stable configuration and when the applied field direction is reversed the system resists any change from the already existing stable configuration. Hence the easy axis loop has high remanence and coercivity. In comparison the green colored loop or the hard-axis loop is far from square and shows minimal remanence and coercivity. In this case it is very difficult to get from the stable demagnetized state to the unstable saturation state and requires high energy. Hence the system saturates at high fields. Also, the spin configuration in the saturation state is highly unstable (spins are aligned with the hard axis). So when the field is reversed, the system quickly tries to revert back to a stable configuration in which spins are parallel to an easy direction. Hence, the hard axis loop has low remanence and coercivity. Here it is important to realize that for the purpose of magnetic storage square hysteresis loops are preferred. Magnetic storage requires two distinct magnetization states (0 and 1) that flip at well defined fields. Hence most materials used as magnetic media have their easy axis aligned along the magnetization direction [1,2].

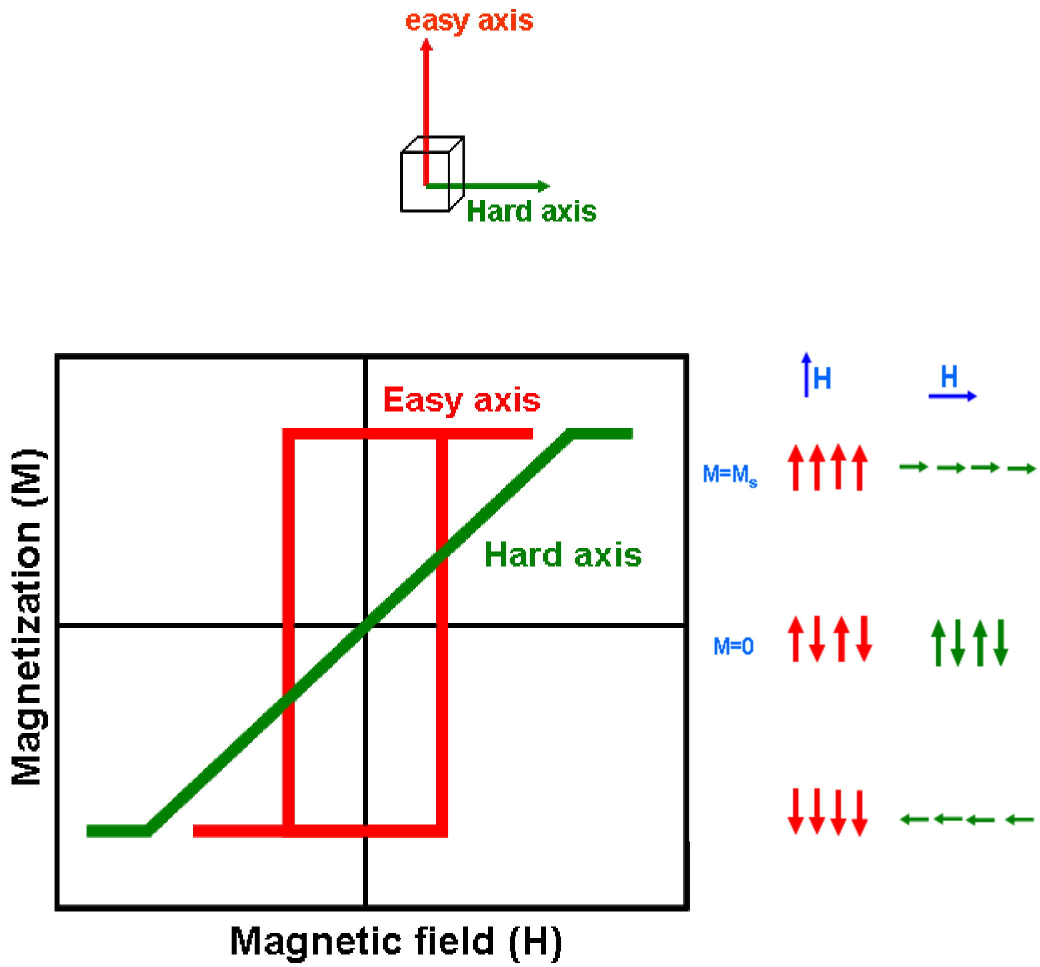

Figure 2-5. Effect of magnetocrystalline anisotropy on the hysteresis curve. The spin configuration in the demagnetized and saturation state is also shown.

2.1.6 Magnetic storage

Over the past couple of decades there has been an ever increasing demand for digital information storage. To cope with this need, hard disks with minimum size are required to store maximum information. Figure 2-6 shows the projected increase in areal density with time [7]. The world's first hard disk drive with an areal density of 2000 bit/in^2 was made in 1956 by IBM. In comparison, the current generation hard disk drives have areal densities close to 80 Gbit/in^2, i.e. a 17 million increase in areal density in 50 years. In the near future one would want to follow the hatched trend shown in Fig. 2-6, leading up to the Terabit/in^2 regime. The hard disk drive has three main components; the storage medium, the write head and the read head. The storage medium is where the data is actually stored in the form of magnetized bits. The write head records data in the storage media (by electromagnetic induction) in the form of ones or zeros. The read head senses the recorded data either by reversal of electromagnetic induction or magnetoresistance [2]. In this study our focus will be on the storage medium.

With the current technology, that uses CoCrPt (K_u = 2×10^6 erg/cm^3) as the recording medium and a longitudinal magnetic recording format, one can get to areal densities as high as 100 Gbit/in^2. Beyond this limit superparamagnetism sets in for the smaller CoCrPt grains. Superparamagnetism causes the spins to flip around randomly and hence the system can no longer be used for magnetic storage [8]. So to get beyond the 100 Gbit/in^2, we have to look for new materials and improved recording techniques. The FePt system is an attractive candidate for high-density storage due to its extremely high uniaxial magnetocrystalline anisotropy (K_u = 7×10^7 erg/cm^3) [9]. The high magnetocrystalline anisotropy permits the use of smaller size particles before the onset of superparamagnetism; this directly leads to larger recording densities. The focus of this study will be to show that FePt is a suitable system for ultra-high density magnetic storage.

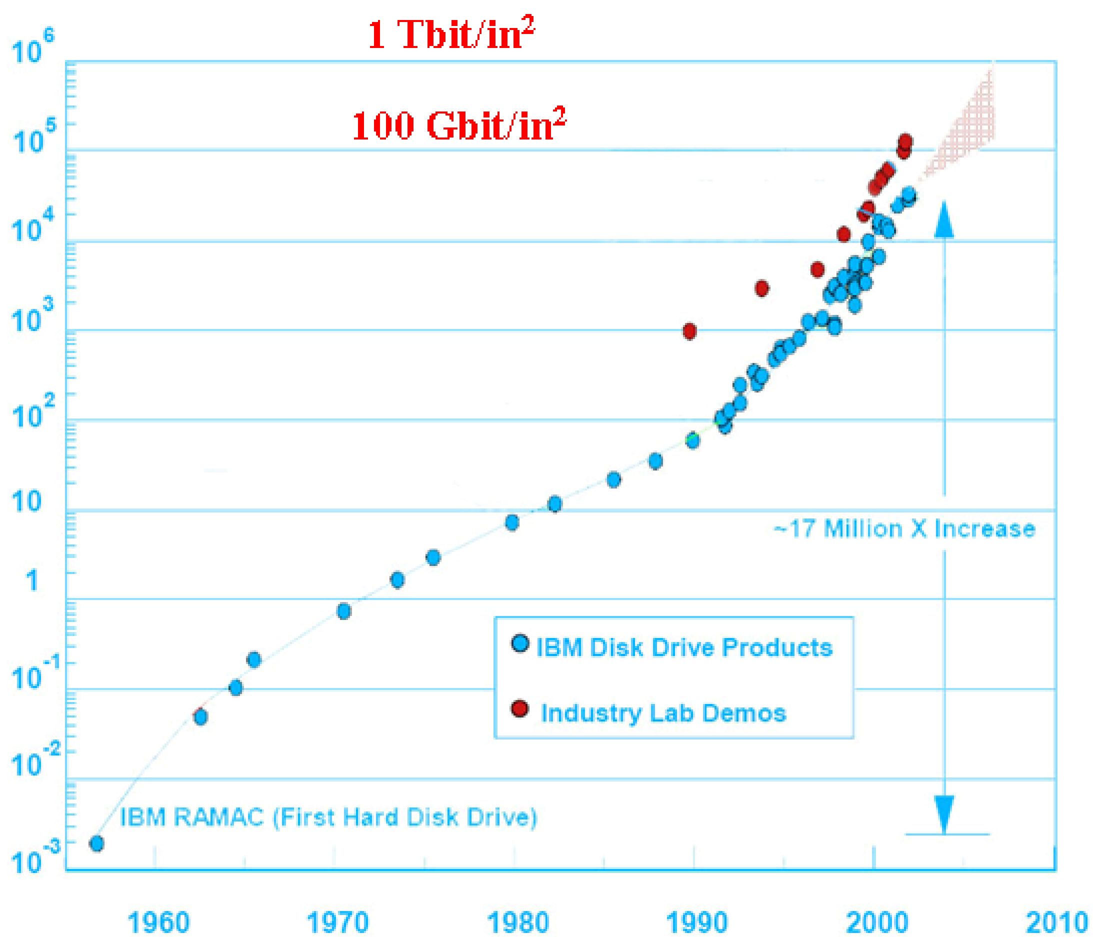

Figure 2-6. Projected increase in areal density with time [7].

Perpendicular recording is another approach used to defeat superparamagnetism and improve areal density [10]. The technique of perpendicular recording is illustrated in Fig. 2-7. A four fold increase in storage density can be realized by employing the perpendicular magnetic recording technique. As shown in Fig. 2-7, in the perpendicular recording scheme the north pole and south pole of neighboring bits are packed next to each other. This causes a reduction in magnetostatic energy and thereby bits can be packed closer to each other leading to improved areal density. In comparison, the longitudinal recording format has an end to end type of bit arrangement. This causes repulsion and hence bits cannot be packed closely. The onset of superparamagnetism can also be delayed by using the perpendicular recording technique. In this approach, by growing long columnar grains the volume of each grain can be increased. Thus, the anisotropy energy (K_uV) improves and remains greater than thermal energy (kT).

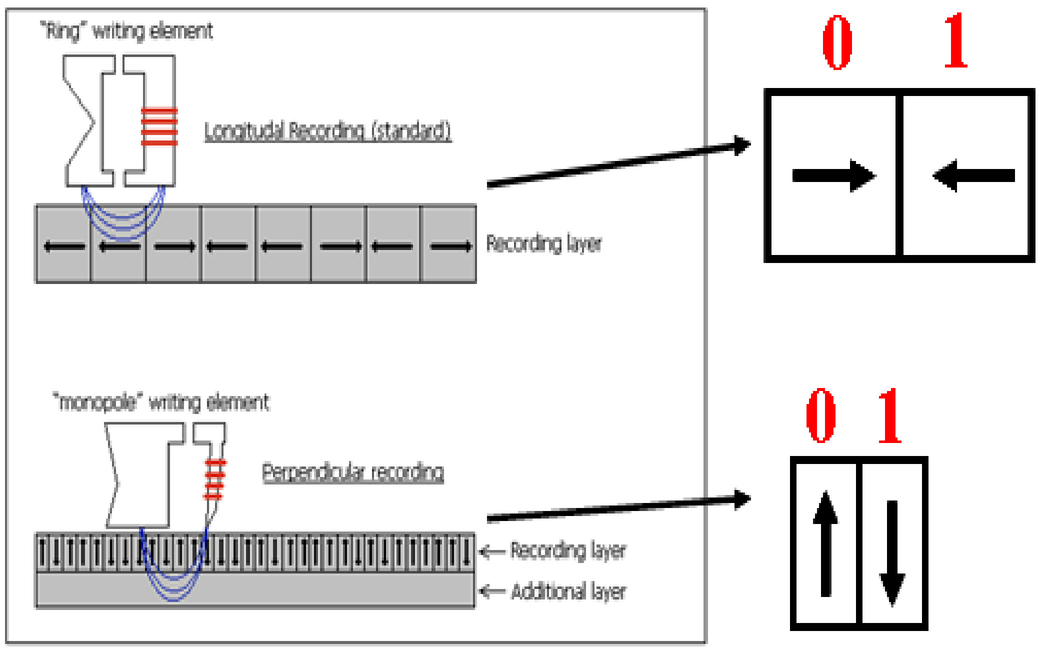

Figure 2-7. Schematic of the perpendicular and longitudinal recording techniques [11].

References

1. B. D. Cullity, Introduction to Magnetic Materials, Addison-Wesley, Readings, MA (1972).
2. N. A. Spaldin, Magnetic materials: Fundamentals and device applications, Cambridge University Press (2003).
3. http://www.aacg.bham.ac.uk/magnetic_materials/type.htm
4. R. H. Kodama, J. Magn. Magn. Mater. **200**, 359 (1999).
5. O. Fruchart, J. P. Nozieres, W. Wernsdorfer, and D. Givord, Phys. Rev. Lett. **82**, 1305 (1999).
6. D. Kumar, J. Narayan, T. K. Nath, A. K. Sharma, A. Kvit, and C. Jin, Solid State Communications, **119**, 63 (2001).
7. http://ed-thelen.org/1401Project/RAMAC-EngProtoType-.jpeg
8. D. Weller and A. Moser, IEEE Trans. Magn. **35**, 4423 (1999).
9. D. Weller, A. Moser, L. Folks, M. E. Best, W. Lee, M. F. Toney, M. Schwickert, J. U. Thiele, and M. F. Doerner, IEEE Trans. Magn. **36**, 10 (2000).
10. K. Ouchi and N. Honda, IEEE Trans. Magn. **36**, 16 (2000).
11. http://en.wikipedia.org/wiki/Perpendicular_recording

2.2 Pulsed laser deposition

2.2.1 Overview

Pulsed laser deposition (PLD) is a versatile non-equilibrium thin film growth technique based on physical vapor deposition. It involves the use of a high-powered laser to vaporize the target material required for thin film deposition. Laser-assisted growth was first demonstrated by Smith et. al. [1] in 1965 using a high power ruby laser. However, it was in the 1980's that PLD gained prominence and was developed as a powerful thin film deposition technique. In 1983, Cheung et. al. [2] successfully synthesized epitaxial $Hg_{0.7}Cd_{0.3}Te$/CdTe and CdTe/GaAs using PLD. Later in the decade, in 1987 Dijkkamp et. al. [3] demonstrated the growth of $YBa_2Cu_3O_7$ superconducting thin films on sapphire. Since then PLD has been widely used to synthesize a variety of high quality thin films of metals, oxides and nitrides.

The PLD system consists of three main components; the laser, the vacuum chamber and the optics that control the laser. Due to this simplicity, the start-up cost for a PLD system is extremely low [4]. In fact, a PLD system can be set up at 1/10 the cost of a MBE system. Some lasers that can be used for PLD are; ruby laser, CO_2 laser, Nd-YAG laser and excimer lasers. The excimer laser is the most widely used, due to its unique characteristics (discussed in the next section). During PLD, the laser is directed into the vacuum chamber and focused onto the target by a set of lenses and mirrors. The vacuum chamber houses the target holder, the substrate holder and the vacuum gauges. The focused laser beam interacts with the target surface creating a luminous plasma plume. Laser-solid interaction and creation/expansion of the plasma is a complicated process and will be discussed in detail in the next section. The ejected species comprising the plume consists of high-energy atoms, electrons, molecules, free radicals and sometimes clusters, particulates and molten globules [4]. These species then deposit on the substrate forming the thin film.

2.2.2 Advantages and disadvantages of PLD

There are several advantages associated with PLD that make it a popular thin film deposition technique. Most advantages arise due to the high energy of the ablated species [5,6]. The energy of the ablated species can be as high as 10 to 100 eV (i.e. about 100-1000 kT). In comparison, the energy of the ejected species in an evaporation technique (thermal or e-beam) is about 0.1 eV at 1200 K [5,6]. Listed below are some advantages and salient features of the PLD technique.

1. The high energy of the plume makes PLD a highly non-equilibrium processing technique. Using PLD complex metastable phases can be formed that would otherwise be difficult to form by equilibrium synthesizing routes. For example, $L1_0$ ordered FePt (superlattice structure) can be synthesized using PLD at a low processing temperature of 500 °C [7].

2. In case of a multi-component system (like YBCO) the high energy of the plume helps to reproduce the stoichiometry of the target in the film [8]. The forward directed nature of the plume in PLD is responsible for maintaining stoichiometry [5,6]. Due to the high energy density of the laser, the material removal from the target is so fast that vapor pressures of the individual components do not play a role.
3. The high energy of the plume reduces processing temperatures. For example, epitaxial TiN can be grown on Si (100) at 600 °C by PLD [9]. On the other hand CVD growth of TiN requires temperatures as high as 900 °C.
4. Multi-layered heterostructure thin films can easily be synthesized using PLD. The target carousel can be suitably manipulated to hold multiple targets (4 to 6 targets). This means multi-layered films can be deposited without breaking the vacuum. For example, using PLD epitaxial growth of PZT/YBCO/STO/MgO/TiN/Si(100) was demonstrated by Sharma et. al [10]. Here, the idea was to integrate PZT with Si (100). The rest of the layers act as template buffer layers.
5. Conceptually, any material can be ablated to form a thin film as long as it has a large enough absorption coefficient for the laser used [4].
6. Depending on the repetition rate of the laser the deposition rate of the film can be controlled. In fact, in PLD the number of nucleation sites can be controlled such that they are much higher than those formed in MBE or sputter deposition. By controlling the impingement rate and increasing nucleation site density the smoothness of the film can be improved [4-6].

7. It is important to realize that in the PLD system the energy source, which is the laser, is placed externally. The vacuum chamber in itself is devoid of filaments and other sources of contamination, thereby resulting in a clean process environment. The interaction between the laser and gas species in the vacuum chamber is minimal. This means that the dynamic range of deposition pressures could be high, resulting in less stringent vacuum requirements. Also, the spatial confinement of laser-solid interaction and the subsequent plume render PLD a clean process. The deposited films are thus relatively contamination free [4].

On the other hand, PLD also suffers from some disadvantages. The area of deposited material obtained by PLD is relatively low (typically 1 cm x cm). In the case of large substrates, non-uniformity in film thickness is observed due to the forward directed nature of the plume [4]. Deposition on larger substrates and uniformity of film thickness can be achieved to some extent by rastering the laser beam over a large target and/or rotation and translation of the substrate [11]. The other important drawback of PLD is the formation of chunks during ablation, which can prove to be detrimental to the quality of the film [12]. Chunks are nothing but large (few microns) particulates or globules of molten material. These undesirable chunks are formed due to improper ablation that involve various mechanisms such as subsurface boiling, expulsion of the liquid layer by shock wave recoil and exfoliation [4, 5, 6, 12]. By careful manipulation of the laser parameters, the size and number of chunks can be minimized to some extent [4,12]. Chunk control is also possible by increasing the absorption coefficient and thermal conductivity of the target material. A compact target with better cohesion of the grains also reduces the emission of chunks.

2.2.3 Types of lasers used for PLD

The term LASER stands for light amplification by stimulated emission of radiation. A laser emits coherent light, with a well defined wavelength, in a narrow low divergent beam. Hence, lasers can be focused and directed effectively to be used for material processing. The most important lasers used for PLD are the Nd:YAG [13,14] and the excimer laser [15,16]. Nd:YAG is a solid state neodymium doped yttrium aluminum garnet laser. The fundamental frequency for this laser is 1064 nm. But these lasers can be doubled, tripled or quadrupled to produce 532 nm, 355 nm and 262 nm wavelengths. The more popular laser used for PLD is the excimer laser. The excimer laser is a type of chemical laser that uses a combination of an inert gas and a reactive gas. Typically the inert gases used are Argon, Krypton and Xenon. The reactive gases typically used are fluorine and chlorine. The excimer lasers are pulsed and operate in the ultra-violet range. They typically operate with pulse duration in the nanosecond regime and repetition rates up to 100 Hz. They can have output energy as high as 1 J/pulse. Various excimer lasers with their corresponding wavelengths are listed in table 2-1. The term excimer is a short form of excited dimer. In these systems lasing action is possible due the population inversion that develops between a bound excited state and a repulsive ground state. The excited state is formed from the inert gas (Kr) that forms temporarily bound molecules either with themselves or the halide (KrF). The excited state is usually induced by an electric discharge. The excited state then gives up its energy via stimulated emission to form the dissociated ground state molecules. This happens very rapidly (within picoseconds), resulting in a population inversion between the excited and ground state molecules. The lasing equations for a KrF excimer laser are shown below [17].

$$2Kr_{(g)} + F_{2(g)} \xrightarrow[\text{electric discharge}]{\text{External energy by}} 2KrF_{(g)} \qquad \text{(excited state)}$$

$$2KrF_{(g)} \longrightarrow 2Kr_{(g)} + F_{2(g)} + \text{energy} \qquad \text{(dissociated state)}$$

Table 2-1. Various excimer lasers with operating wavelengths.

Excimer laser	**Wavelength (nm)**
F_2	157
ArF	193
KrCl	222
KrF	248
Cl_2	259
XeCl	308
XeF	351

2.2.4 Physics of the laser-solid interaction

Although the PLD system in itself is easy to build and operate, the underlying physics involving the laser-solid interaction is quite complex. At energy densities above the threshold for vaporization the laser solid interaction was analyzed and modeled by Singh et. al. [5,6]. Depending upon the interaction of the laser with the target material, Singh et. al. [5,6] divided the laser ablation process into three important regimes:

1. Interaction of the laser beam with the bulk target resulting in evaporation of the surface layers. This regime can be termed as the evaporation regime.
2. The interaction of the laser beam with the evaporated material resulting in the formation of a high-temperature isothermal expanding plasma. This regime prevails when the target starts to evaporate and continues until the end of the pulse.
3. The anisotropic three-dimensional adiabatic expansion of the plume giving rise to the characteristic forward directed nature of the deposition. It is important to realize that this regime starts after the termination of the laser pulse.

Each of these regimes are discussed below in brief.

Laser target interaction:

When a laser beam strikes the target, the electromagnetic energy is used to excite free electrons in the target material. The thermal energy generated by the electron-phonon coupling then evaporates the target material. It is important to realize that the reaction time for this process to occur is on the order of picoseconds [4-6]. In order to have better laser-solid coupling the target must be suitably prepared. A target with high roughness, low reflectivity (R) and high absorption coefficient (α_t) allows for efficient laser-solid coupling and thus provides a low threshold energy for vaporization. Depending on the laser wavelength and the porosity and surface roughness of the target, typical values of threshold energy vary from 0.11 to 0.40 J/cm^2 [5]. It is important to realize that the energy deposited by the laser beam comprises, the energy required to evaporate the target material, conduction heat loss in the target and energy loss due to laser absorption by the expanding plasma. Using these concepts of energy balance, the thickness of the target for which evaporation (ΔX_t) takes place can be calculated as [5,6],

$$\Delta X_t = (1\text{-}R)\ (E\text{-}E_{th})\ /\ (\Delta H + C_v \Delta T) \qquad (4)$$

Where R is the reflectivity, E_{th} is the threshold energy, ΔH is the latent heat, C_v is the volume heat capacity and ΔT is the maximum rise in temperature. It is important to realize that this equation is valid when the thermal diffusion length $(2Dt)^{0.5}$ is larger than the light penetration depth ($L = 1/\alpha_t$) [6]. Here D is the thermal diffusion constant and t is the pulse duration of the laser. This validation is true for most metallic and semiconducting targets. However, for low thermal diffusivity materials (non-metallic targets), i.e. $(2Dt)^{0.5} < 1/\alpha_t$ a second regime is relevant,. Here, thermal diffusivity does not play an important role and evaporation depth mainly depends on the attenuation distance of the laser beam [4-6].

Plasma formation and initial isothermal expansion:

The laser interaction with the target material yields surface temperatures in the range of 2000-3200 K [5,6]. This results in the emission of positive ions and electrons from the free surface. Generally, the ablation of the target is accompanied by the formation of a plasma (bright glow) extending normal to the target surface. The plasma contains charged and neutral species of atoms and molecules. The plasma also interacts with the incoming laser; this produces temperatures higher than the vaporization temperature in the plasma. The absorption of laser energy by the plasma occurs due to electron-ion collisions. This absorption primarily occurs by an inverse Bremsstrahlung process that involves absorption of a photon by a free electron [5,6,18]. The absorption coefficient (α_p) of the plasma is given as [5,6],

$$\alpha_p = 3.69 \times 10^8 \, (Z^3 n_i^2 / T^{0.5} \nu^3) \, [1 - \exp(-h\nu/KT)] \tag{5}$$

Where, Z is the average charge, n_i is the ion density, T is the temperature of the plasma, h is Planks constant, K is the Boltzmann constant and ν is the free energy of the laser light. Since the absorption coefficient (α_p) is proportional to n_i^2, the laser light is heavily absorbed close to the target surface, where the density of the ionized species is high. In comparison the leading edge of the plume, is associated with high expansion velocities and low electron and ion densities. Hence, the outer edge of the plasma is transparent to the laser beam. The [1- exp(-hν/KT)] term takes into account the losses that occur due to stimulated emission depending upon the plasma temperature and laser wavelength [5,6]. A variety of processes such as impact ionization, photo ionization, thermal ionization and electronic ionization effect the extent of ionization of the laser generated species.

Figure 2-8 is a schematic that shows the different regimes that are present during the laser-solid interaction [6]. Region A is the unaffected bulk target and B is the thickness of the target material that is evaporated. Region C is the plasma region close to the target that absorbs the laser heavily. In this region, evaporated particles are continuously injected into the plasma. Region D depicts the outer region of the plasma that expands rapidly. In the region near the target surface, a dynamic self-regulating equilibrium exists between the plasma absorption coefficient and the rapid transfer of thermal energy into kinetic energy (due to injection of evaporated particles of the target into the plume). These compensating mechanisms govern the isothermal temperature attained by the plasma near the target surface [5,6].

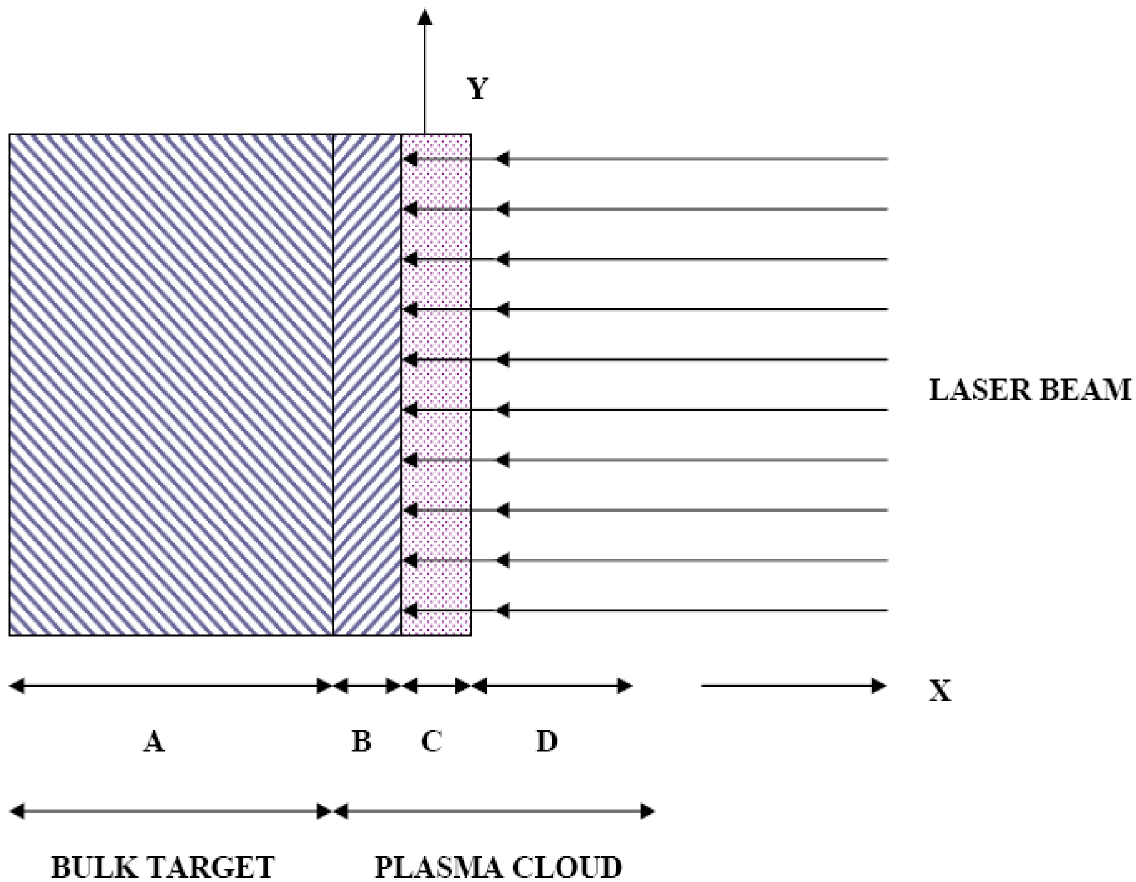

Figure 2-8. Schematic illustration showing different regimes during laser irradiation of the target: (A) Bulk target that remains unaffected, (B) Thickness of the target material that evaporates, (C) region in which the plasma absorbs the laser heavily and (D) the expanding plasma region that is transparent to the laser [5,19].

Singh et. al.[5,6] have come up with expressions that determine the variation of density, pressure and velocity along the direction perpendicular to the target surface. Figure 2-9 is a summary of their results. It should be noted that the direction perpendicular to the target surface is the x direction. It is clear from the figure that the density of particles is a maximum in the near-target regions, where as the velocity is minimum. The particle density in the plasma in the near surface regions can be approximated as a Gaussian. It has also been observed that the initial dimensions of the plasma are larger in the transverse direction when compared to the longitudinal direction. During the initial stages the velocity is low and acceleration is relatively high. After a while, when the expansion velocity increases, the acceleration decreases and eventually reaches zero. This aspect governs the elongated shape of the plasma.

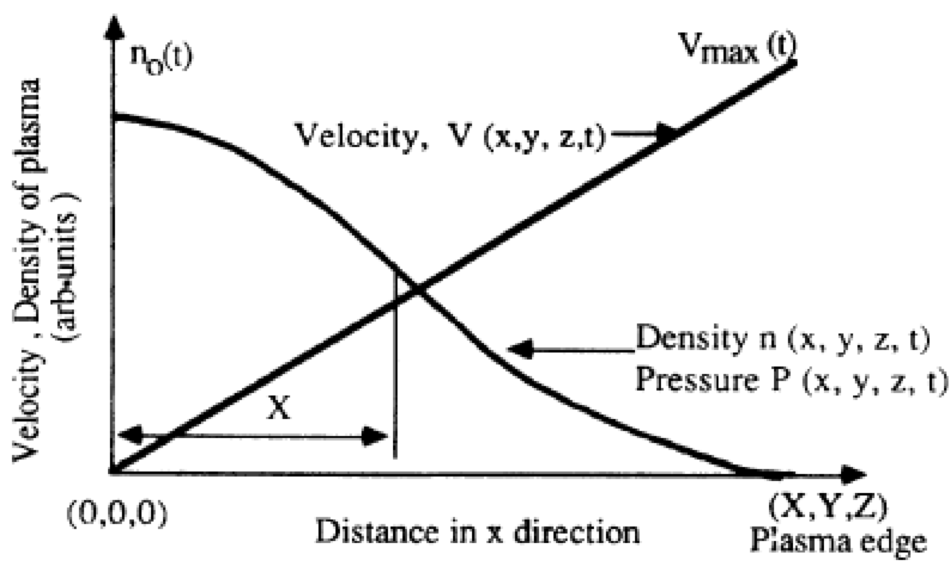

Figure 2-9. Schematic illustration showing the variation of the pressure (P), velocity (V) and density (n) with the distance (moving out of the plasma) [6].

Adiabatic expansion of the plasma:

After the plasma formation and isothermal regime, the plasma plume expands adiabatically into the vacuum. The adiabatic expansion regime initiates after the termination of the laser pulse [6]. It is important to realize that in this regime, there is no injection of particles from the target into the plume and also the laser is no longer being absorbed by the plume. Singh et. al. [5,6] have developed equations that explain the adiabatic expansion in relation to the dimensions of the plume. They have come up with the following inferences. In this regime, the expanding plasma is associated with very high velocities arising from the thermal energy being converted to kinetic energy. The loss in thermal energy leads to a drop in temperature determined by a balance between cooling due to expansion and energy gain due to recombination of ions in the plasma. Figure 2-10 shows a schematic of the developing shape of the plume in the adiabatic regime. The initial dimensions of the plasma are larger in the transverse directions, i.e. in the y and z direction (see Fig. 2-10). In the longitudinal x direction the expansion is minimal. The transverse dimensions are in the order of a few millimeters as opposed to 20-100 microns in the longitudinal direction. It is also important to note that the plasma is elliptically shaped with y axis being the major axis (see Fig. 2-10a). During the adiabatic expansion regime, the longitudinal x dimension expands rapidly resulting in the characteristic PLD plume. The plasma pressure drops rapidly until most of the thermal energy is converted to kinetic energy. Then the plume has no more energy for expansion and the plasma elongates in the shorter dimension. Eventually, an elliptical shape is retained but with the z dimension being the major axis (see Fig. 2-10b). This theory was confirmed from the shape of the deposited YBCO film on Si, as shown in Fig. 2-10c.

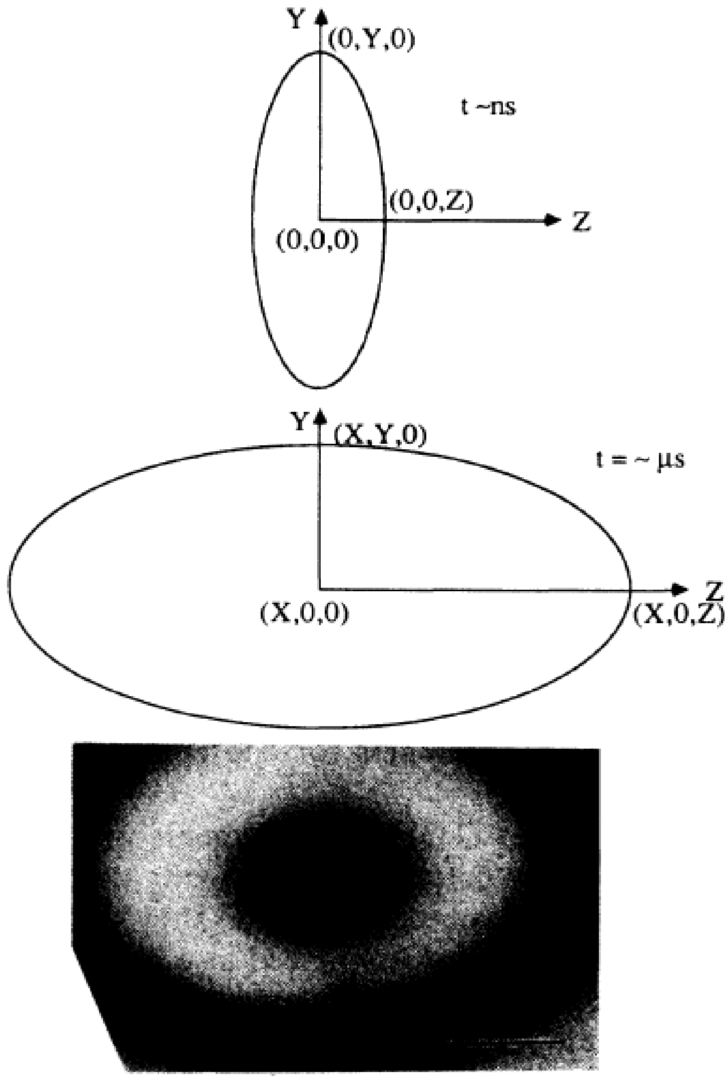

Figure 2-10. (a) Schematic illustration showing the initial elliptical shape of the plasma just after the laser pulse is terminated. (b) Final shape of the plasma when it hits the substrate. (c) Shape of a YBCO film deposited on a Si substrate [6].

References

1. H. M. Smith and A. F. Turner, Appl. Opt. **4**, 147 (1965)
2. J. T. Cheung and T. Magee, J. Vac. Sci. Technol. A **1**, 1604 (1983).
3. D. Dijkkamp, T. Venkatesan, X. D. Wu, S. A. Shaheen. N. Jisrawi, Y. H. Min-Lee, W. L. McLean, and M. Croft, Appl. Phys. Lett. **51**, 619 (1987).
4. Pulsed Laser Deposition of Thin Films, edited by D. B. Chrisey and G. K. Hubler, Wiley-Interscience, New York, 1994.
5. R. K. Singh, O. W. Holland, and J. Narayan, J. Appl. Phys. 68, **233** (1990).
6. R. K. Singh and J. Narayan, Phys. Rev. B **41**, 8843 (1990).
7. G. R. Trichy, D. Chakraborti, J. Narayan, and J. T. Prater, J. Phys. D: Appl. Phys. **40**, 7273 (2007).
8. J. Narayan, N. Biunno, R. Singh, O. W. Holland, and O. Auciello, Appl. Phys. Lett. **51**, 1845 (1987).
9. J. Narayan, P. Tiwari, X. Chen, J. Singh, R. Chowdhury, and T. Zheleva, Appl. Phys. Lett. **61**, 1290 (1992).
10. A. K. Sharma, J. Narayan, C. Jin, A. Kvit, S. Chattopadhyay, and C. Lee, Appl. Phys. Lett. **76**, 1458 (2000).
11. J. A. Greer and M. D. J. Tabat, Vac. Sci. Technol. A **13**, 1157 (1995).
12. R. K. Singh, D, Bhattacharya, and J. Narayan, Appl. Phys. Lett. **57**, 2022 (1990).
13. M. Y. Chen and P. T. Muryay, J. Mater. Sci. **25**, 4929 (1990).
14. P. Macquart, F. Bridou, and B. Pardo, Thin Solid Films **203**, 77 (1991).

15. X. D. Wu, A. Inam, T. Venkatesan, C. C. Chang, E. W. Chase, P. Barboux, J. M. Tarascon, and B. Wilkens, Appl. Phys. Lett. **52**, 754 (1988).
16. J. J. Kingston, F. C. Wellstood, P. Lerch, A. H. Miklich, and J. Clarke, Appl. Phys. Lett. **56**, 189 (1990).
17. http://en.wikipedia.org/wiki/Krypton_fluoride_laser
18. P. R. Willmott and J. R. Huber, Rev. Mod. Phys. **72**, 315 (2000).
19. Amit Chugh, PhD Thesis, North Carolina State University (2005).

2.3 Growth

Thermodynamic understanding of thin film growth identifies three basic modes of growth [1]. The surface energy of the substrate (γ_s), the surface energy of the film (γ_f) and the interfacial energy (γ_{sf}) govern the growth mode for a given system. The three growth modes are illustrated in Fig. 2-11.

1. Frank-van der Merwe (FM):

In this mode, deposition proceeds by two dimensional layer-by-layer growth. Complete wetting of the substrate surface occurs, i.e. the first set of atoms condense to form a monolayer on the substrate, after which the second layer comes in and builds on the first layer to form the film [1]. For this reason the FM growth mode is also referred to as the 2D growth mode. The FM growth mode is illustrated schematically in Fig. 2-11a. The following condition favors FM growth;

$$\gamma_f + \gamma_{sf} < \gamma_s \tag{6}$$

This equation suggests that the system gains energy when totally covered by the thin-film layer. Equality in equation (6) explains FM growth mode in the case of homoepitaxy, i.e. the substrate and the film material is the same. It is also important to realize that for FM growth to occur γ_f should be much less than γ_s and the interfacial energy (γ_{sf}) should be low. Most metal on metal and semiconductor on semiconductor systems follow the FM mode of growth. In the context of this study, TiN grows on Si (100) by FM growth.

2. Volmer-Weber (VW):

The VW growth mode is associated with the formation of 3D islands. Instead of wetting the surface, individual cluster-like islands are formed. This type of growth is illustrated in Fig. 2-11b. VW growth happens when the following equation is valid,

$$\gamma_f + \gamma_{sf} > \gamma_s \tag{7}$$

i.e. the surface energy of the substrate is less than sum of the surface energy of the film and the interfacial energy [1]. Here, as shown in the Fig. 2-11b, the interfacial energy is high and the surface energies of the film and substrate are low. So the system adjusts itself so that the high-energy interface formed is minimal and in doing so 3D islands are formed instead of a continuous wetting layer. It is important to realize that for longer growth times, the islands keep growing in size and finally neighboring islands coalesce to form a continuous thin film. This type of growth can be observed in systems where metals are grown on insulators, example Ni on amorphous Al_2O_3. In the context of this research, FePt grows on TiN via the VW growth mode.

3. Stranski-Krastanov (SK):

This mode combines the 2D and the 3D growth modes as illustrated in Fig. 2-11c. Initially, a continuous wetting layer is formed over the substrate. Due to the lattice mismatch, strain accumulates in the 2D film and in order to relieve this strain 3D islands are formed [3,4]. It is important to note that the islands grown in the SK mode are coherently strained and dislocation free, i.e., the accumulated strain that switches the growth mode from 2D to 3D is relieved by forming coherently strained islands rather than by introducing dislocations [2-4]. This type of strain relaxation is called the volume elastic relaxation and it competes with the formation of dislocations [5]. SK growth also follows equation (6). But in this case the interfacial energy and the surface energy of the substrate are high and the surface energy of the film is low.

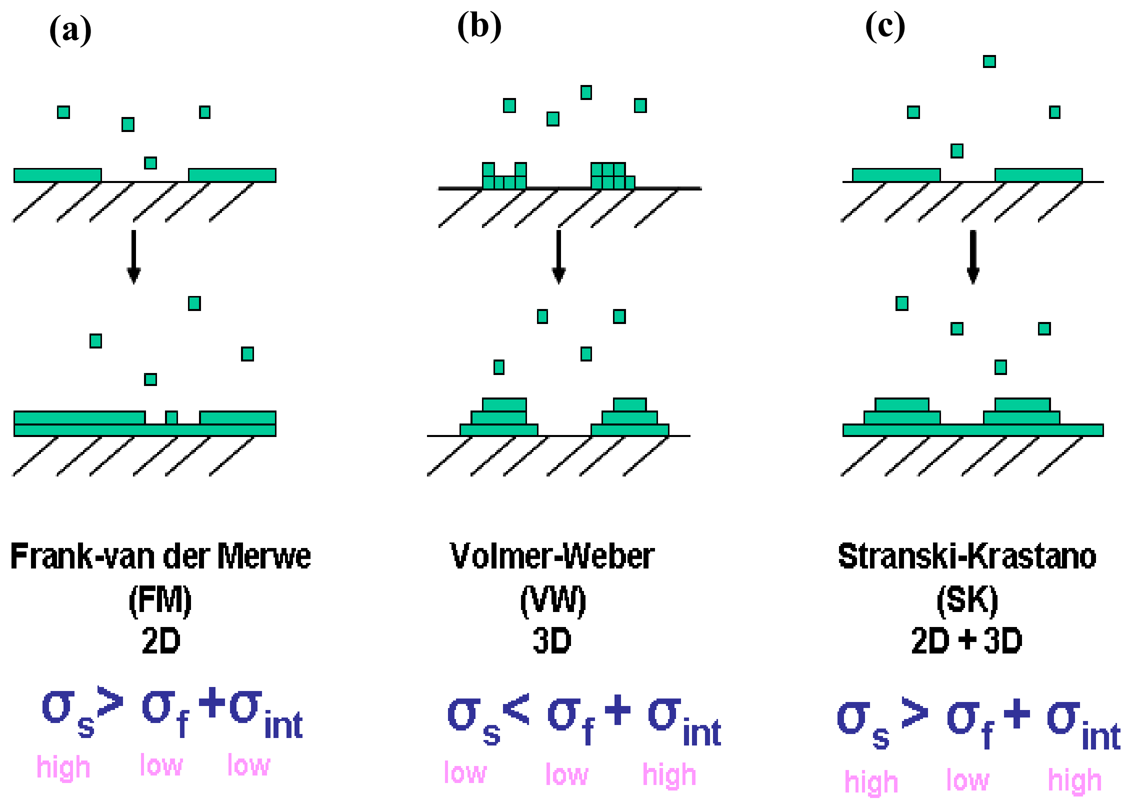

Figure 2-11. Schematic illustration of the three crystal growth modes [6].

2.3.1 Island growth

In the previous section we have looked at the thermodynamical aspect of thin-film growth. In the actual practice of thin-film growth, in addition to thermodynamics, kinetics plays a very important role. The kinetic aspect looks at local factors in the system such as the density of arriving atoms (determined by the deposition rate) and surface mobility of the deposited adatoms (governed by substrate heating and local defects such as kinks, steps or vacancies). The literature shows several studies that report growth of nanoscale islands with a narrow size distribution and no Ostwald ripening. These include material systems like GeSi/Si (100) [7], InAs/GaAs (001) [8] and Ni/Al_2O_3/Si (001) [9]. It is important to understand that thermodynamic stability corresponds to a global minimum in the free energy of the system. Kinetic theories would suggest that after forming the 3D islands they would tend to grow to seek thermodynamic stability. But this unwanted process can be controlled kinetically. By controlling the kinetics we seek a local minimum in the system free energy as shown in Fig. 2-12 [2]. Figure 2-12 is a plot between the total energy of the system and the island size. One example of controlling the kinetics to prevent Ostwald ripening would be to cap the 3D islands with a suitable material immediately after growth [10]. Another technique would be to cool down the system immediately after the formation of the islands [11].

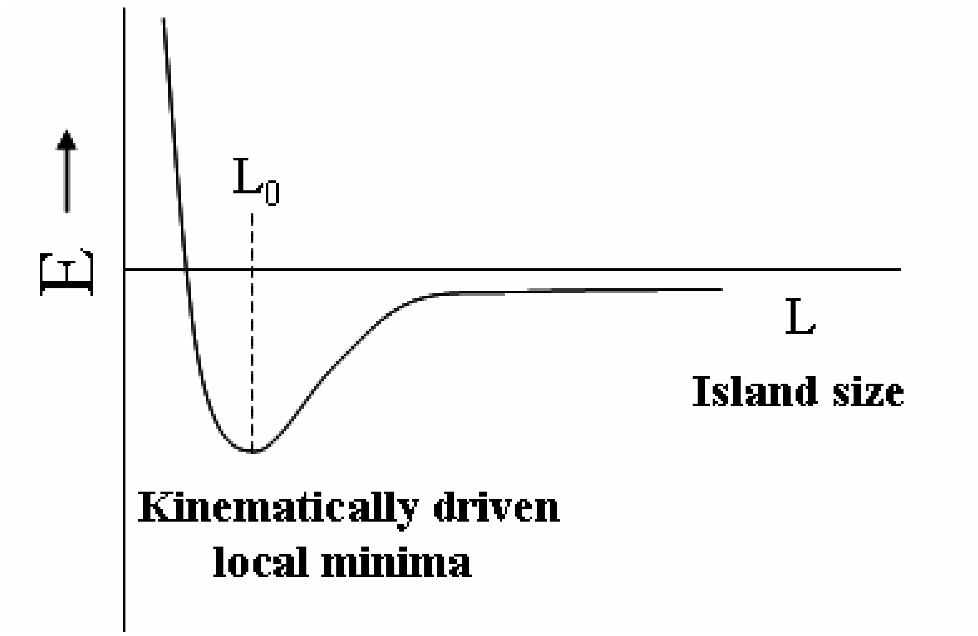

Figure 2-12. Kinetically obtained local minima in energy [2].

An accepted model described in references 2, 12 and 13 takes into account the total energy of the system governed by the island energy, the interaction energy and the surface energy. The energy of the island comprises the lattice mismatch and the edge energy. The interaction energy arises from the elastic interactions between neighboring islands. The surface energy arises due to the discontinuity in the surface tensor at each island edge [13]. This model shows that for a certain growth parameter regime the equilibrium state for a system of 3 dimensional coherently strained islands corresponds to a periodically ordered array of islands in 2D, with no Ostwald ripening. The ordering in terms of size is explained taking into account the driving forces. Two important driving forces have been identified, the elastic relaxation due to discontinuity of the intrinsic surface stress tensor at the island edges and the strain induced renormalization of the surface energies [12, 13]. It is important to note that although the total surface area is increasing owing to the formation of 3D islands, the renormalization results in a decrease in the total surface energy. Hence in terms of energy Ostwald ripening is unfavorable and it does not occur. The derivation of the total energy of the system leading to Fig. 2-12 is briefly described below.

$E_T = E_{island} + E_{interaction} + E_{surface}$

E_{island} = energy from lattice mismatch + edge energy

$E_{interaction}$ = elastic interaction energy

$E_{surface}$ = energy due to discontinuity in the surface stress tensor

Assuming the condition for equilibrium to be the total energy minimization, the model comes up with following set of equations. The total energy (E_T) of the system as a function of island size (L) is given as,

$$\Delta E_T = E_0\left[-2\left(\frac{L_0}{L}\right)^2 \ln\left(\frac{e^{1/2}L}{L_0}\right) + \frac{2\alpha}{e^{1/2}}\left(\frac{L_0}{L}\right)\right] \tag{8}$$

Where E_0 is the characteristic energy per atom defined as;

$$E_0 = \frac{1}{2} \frac{\Omega f_2(\phi_0)(6\cot\phi_0)^{2/3} \tau^2}{\lambda L_0^{\ 2}} \tag{9}$$

L_0 is the characteristic length given as;

$$L_0 = 2\pi a \exp\left[\frac{f_3(\varphi)\eta\lambda}{f_2(\varphi)\tau^2} + \frac{1}{2}\right] \tag{10}$$

And α is the control parameter, defined as the ratio of the change in surface energy due to island formation and the contribution of the edges to the elastic relaxation energy. It is given as;

$$\alpha = \frac{1}{2} \frac{e^{1/2} \lambda L_0}{f_2(\phi_0)(6\cot\phi)^{1/3} \tau^2} (\Delta\Gamma) \tag{11}$$

The parameters involved in the above equations are defined below;

λ = elastic modulus

φ = tilt angle of the side facets of the island that shows up during surface renormalization of the surface stress tensor and the edge energy

f_2, f_3 are geometric factors depending on the island shape

η = characteristic energy per unit length of the edge

τ = surface stress tensor

a = lattice parameter

Ω = atomic volume

$\Delta\Gamma$ = change in the renormalized surface energy due to island formation per unit volume

From the above analysis, it was inferred that for $\alpha < 1$, the plot between the total energy and island size gives a local minimum in energy around the characteristic length L_0 (see Fig. 2-12). This plot shows that for the system to be in a kinetically driven metastable state one needs to choose an appropriate island size close to L_0. For $\alpha > 1$, there exists a thermodynamic preference towards clustering, which is undesirable.

References

1. P. Moriarty, Rep. Prog. Phys. **64**, 297 (2001).
2. V.A. Shchukin and D. Bimberg, Rev. Mod. Phys. **71**, 1125 (1999).
3. Serge Luryi and Ephraim Suhir, Appl. Phys. Lett. **49**, 140 (1986).
4. D.J. Eaglesham and M. Cerullo, Phys. Rev. Lett. **64**, 1943 (1990).
5. D. Vanderbilt, L.K. Wickham, in Evolution of Thinfilm and Surface Microstructure, ed. By C.V. Thompson, J.Y. Tsao, and D.J. Srolovitz, MRS Proceedings, Vol. 202, p555 (1991).
6. Honghui Zhou, PhD Thesis, North Carolina State University (2004).
7. R. Apetz, L. Vescan, A. Hartmann, C. Dieker, and H. Luth, Appl. Phys. Lett. **66**, 445 (1995).
8. A. Ponchet, A. Le Corre, H.L. Haridon, B. Lambert, and S. Salaun, Appl. Phys. Lett. **67**, 1850 (1995).
9. J. Narayan and A. Tiwari, J. NanoSci. and Nanotech. **4**, 726 (2004).
10. R. Leon, S. Fafard, D. Leonard, J. L. Mertz, and P. M. Petroff, Appl. Phys. Lett. **67**, 521 (1995).
11. J. M. Moison, F. Houzay, F. Barthe, L. Leprince, E. Andre, and O. Vatel, Appl. Phys. Lett. **64**, 196 (1994).
12. V.A. Schukin, N.N. Ledentsov, P.S. Kopev, and D. Bimberg, Phys. Rev. Lett. **75**, 2968 (1995).
13. V.A. Schukin, N.N. Ledentsov, M. Grundmann, P.S. Kopev, and D. Bimberg, Surf. Sci. **352**, 117 (1996).

2.4 Domain matching epitaxy

2.4.1 Thin film growth by DME

Epitaxial growth of thin films with minimal defects is the key for the optimized performance of modern day microelectronic, optical and magnetic devices [1-3]. Epitaxy is the growth of a single crystal film on top of a single crystal substrate [4]. Traditionally, it was understood that both the film and the substrate would have the same crystal structure and orientation. Homoepitaxy refers to the case where the grown film is made up of the same material as the substrate. In this case the lattice parameters of the film and the substrate are the same, i.e. no misfit strain exists and there are no missing interfacial bonds. Heteroepitaxy refers to the case where the film and the substrate are composed of different materials. In this case film properties largely depend on the mismatch between the film and substrate lattice parameter, the difference in the film and substrate chemistry and the difference in the thermal expansion coefficient of the film and the substrate. Thin-film growth in the case of heteroepitaxial systems can occur via the formation of a coherently strained lattice [4]. Due to the mismatch in lattice constants, the epilayer tries to assume the lattice constant of the substrate and in doing so the epilayer becomes strained [5-7]. With increase in thickness the strain energy in the system keeps increasing. Finally, dislocations or missing half planes are formed to relieve the built-in strain in the system [5-7].

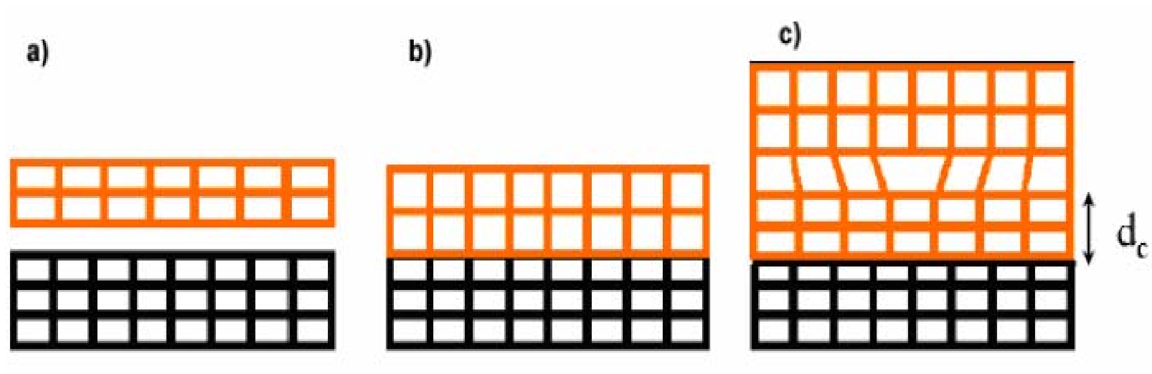

Figure 2-13. Schematic illustration of lattice matching epitaxy (a) film and substrate shown individually before growth, (b) pseudomorphic or coherent growth below critical thickness, (c) formation of dislocation or missing half plane beyond the critical thickness [8].

The conventional lattice matching epitaxy explains heteroepitaxial growth for lattice misfit strains less than 7-8 %. The misfit strain in this case is calculated from the following expression,

$$\varepsilon = a_f / a_s - 1 \tag{12}$$

This misfit strain is accommodated by the coherently strained layer below a critical film thickness. Thus as shown in Fig. 2-13b, the film grows pseudomorphically until the critical thickness is reached. Beyond the critical thickness it becomes energetically favorable to form dislocations (see Fig. 2-13c) [5-7]. These dislocations relieve the remaining strain in the system. The dislocations that are formed at the film surface glide to the interface. The burgers vector and planes of the dislocation are governed by the active slip systems and glide planes are determined by the crystal structure of the film [1,5,9]. In the case of VW or 3D growth, the edge of the islands that are associated with dislocations have Burgers vectors dictated by geometrical constraints [7]. As an example, 90° dislocations at the edge of Ge islands on Si have a/2<110> as the Burgers vector and lie in the (001) film-substrate interface [10]. It is important to note that smaller misfits are associated with smaller interfacial energy and coherent epitaxy conditions [1,5]. Above the 7-8 % misfit regime, it was understood that textured or poly-crystalline films would form. This notion was changed when Narayan et. al. [5] proposed the concept of domain matching epitaxy (DME).

DME is a new paradigm of thin film growth, where integral multiples of lattice planes match across the film-substrate interface and the size of the domain equals integral multiples of planar spacing [5,11,12,13]. This idea is fundamentally different from the conventional lattice matching epitaxy where lattice constants are matched one-to-one across the film-substrate interface to grow epitaxial films with less the 7-8 % misfit. By invoking the concept of DME, epitaxy can be explained in systems with high misfit, i.e. beyond the 7-8 % misfit regime [5]. It is important to realize that when the film and the substrate have similar crystal structure the matching of planes is the same as matching of lattice constants. Hence for low misfit systems (less than 7-8 %) with the same crystal structure, DME reduces to the conventional lattice matching epitaxy.

In DME, the large misfit between the film and the substrate is accommodated by a series of interface dislocations. Due to the large misfit, the dislocations are introduced within the first few monloayers and the rest of the film can be grown defect free. It is important to note that at misfit strains greater than 8 % we are looking at critical thicknesses less than a monolayer [5]. The atomic steps formed within the second monolayer provide nucleation sites for the dislocations. The dislocations have to travel only a monolayer before they reach the interface. If the growth mode is FM or 2D, then the dislocations propagate to the sides of the wafer and in doing so they are confined to the interface. In this case the formation of undesirable threading dislocations is minimal [5]. On the other hand, if initial growth of the monolayer is a mixture of 2D and 3D growth (VW growth) then the dislocation segments may not propagate throughout the entire length and threading dislocations form. So using DME one can control the dislocation density and confine dislocations to the interface depending on the growth characteristics and number density of surface steps [5].

The oxide systems form a critical example where DME can be used to grow high quality films. In general, in oxide systems such as LSMO, LCMO and PZT the nucleation and propagation of a dislocation is difficult. And when these oxide thin films are grown on low misfit substrates like STO only a part of the strain is relieved by dislocations and this strain builds up with increasing thickness. This could prove detrimental to the film properties. However, by invoking the concept of DME, one can get strain-free oxide films by growing them on high-misfit substrates like MgO [14]. In a large misfit condition, the critical thickness is less then a monolayer. Additionally, during the initial stages of growth there are a lot of steps formed that make dislocation nucleation easy. In this condition once the dislocation nucleates it does not have to propagate far (only a monolayer) to reach the interface. So for oxide growth via DME, the dislocations are set at the interface and the entire strain is relieved within a monolayer. The rest of the film then grows strain free.

The conventional lattice matching epitaxy for low misfit systems suffers from some critical disadvantages. Firstly, complete strain relief can be difficult to achieve via the conventional lattice matching epitaxy. This is particularly true in systems where nucleation and propagation of dislocations is difficult. Secondly, there is a high probability of forming threading dislocations that ruin the device. For low misfit systems the critical thickness is large. The dislocations nucleate only after the critical thickness is reached and must then glide across the film thickness to the interface. This process results in the formation of half-loops that are composed of two threading segments and a straight segment along the interface.

In the following section mathematical concepts governing the DME framework will be described. Domain matching epitaxy, as the name suggests is based on the idea of matching lattice planes of the film and the substrate [5]. Within a domain integral planes of the film and substrate match and the domains themselves are separated by missing half-planes (dislocation). The film and the substrate can have either a fixed or same orientation depending on the kind of misfit [5]. The planes that are matched in DME can be different as long as they maintain similar crystal symmetry. In comparison, in the case of conventional lattice matching epitaxy for low misfit systems (< 7-8 %) only the same planes of the film and substrate are matched. In DME the initial misfit strain (ε) can be very large and it is given as [5],

$$\varepsilon = \frac{d_f}{d_s} - 1 \tag{13}$$

Where d_f and d_s are the planar spacing of the film and substrate, respectively. This misfit can be relaxed by matching m planes of the substrate with n planes of the film. So the residual misfit (ε_r) can be calculated as [5],

$$\varepsilon_r = \frac{md_f}{nd_s} - 1 \tag{14}$$

If $md_f = nd_s$ and $\varepsilon_r = 0$, then perfect matching occurs. This means a single m/n domain repeats itself throughout the system to relax the misfit strain. On the other hand if ε_r is non-zero and has a finite value, then two domains exist that alternate with a certain frequency to provide for a perfect matching. So by introducing the frequency factor α we arrive at the following equation [5],

$$(m + \alpha)\, d_f = (n + \alpha)\, d_s \tag{15}$$

To understand this concept let us proceed with an example where $\alpha = 0.5$. In this case there exist two domains m/n and m+1/n+1, that alternate with equal frequency to relieve the misfit strain in the system. If we assume that $d_f > d_s$, then it implies that n > m. Hence,

$$n-m = 1 \text{ or } f(m) \tag{16}$$

where f(m) is a function of m. From the above equations we arrive at

$$(m + \alpha)\, \varepsilon = 1 \text{ or } f(m) \tag{17}$$

This equation governs the concept of DME and is plotted in Fig. 2-14 [5]. In this figure the misfit strain is plotted versus the inverse of the integral multiple of planes matching across the interface. It provides a unified framework encompassing both the LME and DME with misfit strains ranging from 2 – 50 %. In this plot, n-m = 1 for ε = 0 to 50 % and n-m = f(m) for ε = 50 to 100 %. Table 2-2 is a summary of various heteroepitaxial systems that can be grown by DME [5]. Included in the table are the m/n ratio, planar spacing and misfit strain. This table provides a clear picture of the number of planes that are involved in domain matching for a particular misfit strain.

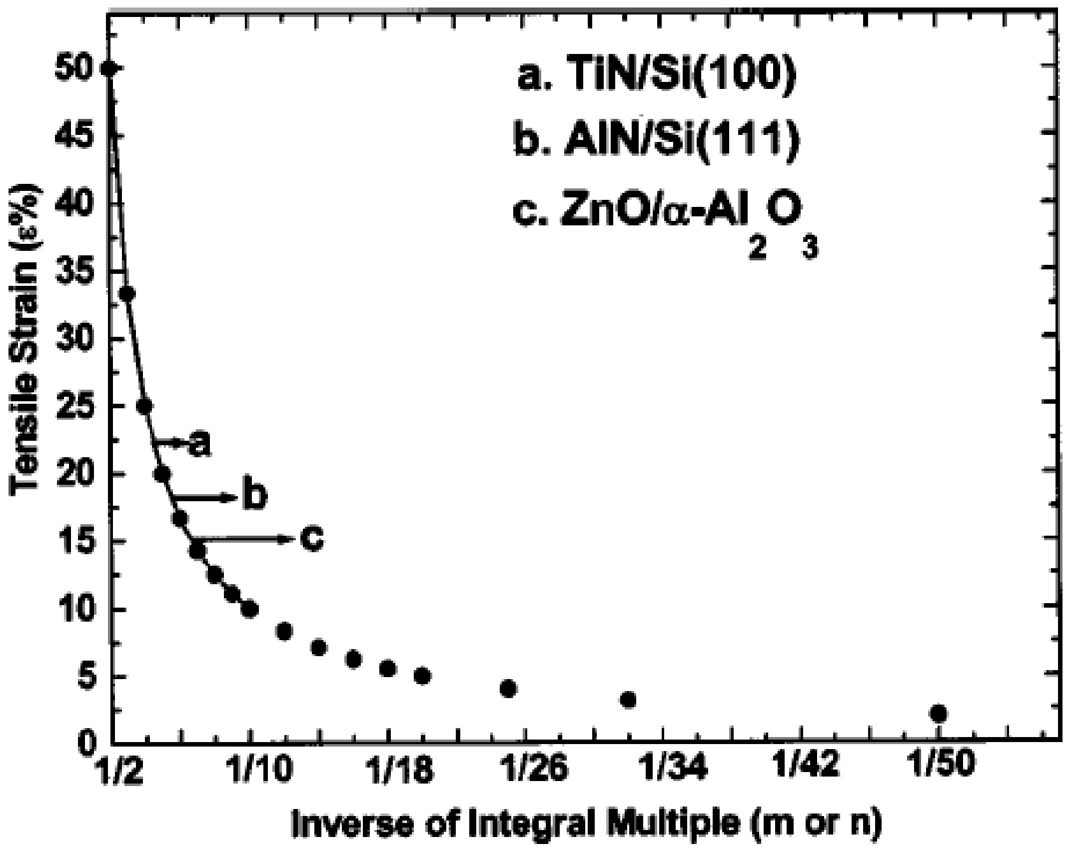

Figure 2-14. Unified plot of misfit strain vs film-substrate planar spacing ratio showing both the LME (< 7 % strain) and DME regions [5].

Table 2-2. Domain matching epitaxy details for various heteroepitaxial systems [5].

m/n	Planar spacing ratio	Experimental examples	Strain ε%
1/10	0.1		90.0%
1/9	0.11		88.8%
1/8	0.125		87.5%
1/7	0.143		85.7%
1/6	0.166		83.3%
1/5	0.20		80.0%
1/4	0.25		75.0%
1/3	0.33		66.7%
1/2 and 1/3	0.33−0.50	Mo, Nb, Ta, W/Si; Ni_3Al/Si(100)	50.0%
1/2	0.50	Fe/Si, Cr/Si, NiAl//Si(100)	
2/3	0.666	Cu/Si(100)	33.33%
3/4	0.750	TiN/Si(100)	25.00%
4/5	0.80	AlN/Si(111)	20.00%
5/6	0.83	$\alpha-Al_2O_3$ /ZnO(0001)	16.67%
6/7	0.857	$\alpha-Al_2O_3$ /ZnO(0001), Cu/TiN(100)	14.29%
7/8	0.8750	$\alpha-Al_2O_3$ /GaN(0001)	12.50%
8/9	0.888	$\alpha-Al_2O_3$ /AlN(0001),	11.11%
9/10	0.90	$YBa_2Cu_3O_{7-}\delta$/MgO(001)	10.0%
11/12	0.9166	$YBa_2Cu_3O_{7-}\delta$/MgO(001)	8.33%
12/13	0.9230	STO/MgO(001)	7.69%
13/14	0.3286		7.14%
14/15	0.9333		6.67%
16/17	0.9412		5.88%
17/18	0.9444		5.55%
18/19	0.9474		5.26%
19/20	0.9500		5.00%
20/21	0.9524		4.76%
22/23	0.9556		4.35%
24/25	0.96	Ge/Si(100)	4.0%
31/32	0.9687		3.13%
49/50	0.98	Ge−Si/Si(100)	2.0%

2.4.2 DME of the TiN/Si (100) system

In the context of this dissertation there is a concomitant need to understand the growth of epitaxial TiN on Si (100). In our study TiN is used as a template buffer to control growth of FePt along the [001] direction. It also acts as an excellent diffusion barrier between FePt and the underlying Si (100) substrate. The quality of the c-axis oriented FePt thin films depends directly on the quality of the TiN buffer layer. A perfectly epitaxial TiN buffer layer is a must for desired [001] growth of FePt. The growth of epitaxial TiN on Si (100) is a major scientific challenge because of the 22 % misfit strain involved. The lattice parameter of TiN is 4.24 Å and for Si the lattice parameter is 5. 43 Å.

Epitaxial growth of TiN on Si can be achieved by domain matching epitaxy [11,15]. Growth was performed by pulsed laser deposition using a KrF excimer laser with wavelength = 248 nm and pulse duration = 25 ns. Ideal conditions for TiN growth are as follows; temperature = 600-620 °C, pressure = 10^{-7} torr and laser density = 2-3 J/cm^2. Figure 2-15 shows a high-resolution cross-section TEM image of TiN/Si(100) interface [5]. The diffraction pattern (inset) shows a cube-on-cube epitaxy, with all three <100> planes of the film parallel to the substrate. The missing half-planes or dislocations are clearly marked between the domains. We observe the presence of two domains in this figure. The larger domain involves matching of 5 planes of TiN with 4 planes with of Si. In the smaller domain 4 planes of TiN match with 3 planes of Si. The 4/5and 3/4 domains alternate with a frequency factor $\alpha = 0.5$ to accommodate the 22 % misfit in the system. This means perfect matching occurs for $\alpha = 0.5$, as the following analysis shows,

$$(m+\alpha)\, d_{Si} = 3.5a_{Si} = 19.01 \tag{18}$$

$$(n + \alpha)\, d_{TiN} = 4.5a_{TiN} = 19.08 \tag{19}$$

Therefore $(m+\alpha)\, d_{Si} = (n + \alpha)\, d_{TiN}$ indicates perfect matching with no residual strain left in the system. Energy conditions also favor the concept of DME. As described in ref. [12], there is a significant reduction in energy for epitaxial growth of TiN on Si(100) by DME, when compared to the unrelaxed state.

Detailed analysis of HRETEM images reveal the burgers vector as a/2<110> lying in the {111} planes. Two sets of a/2<110> dislocations interact at the interface to produce a/2<110> dislocations lying in the {001} interface.

$$a/2[101](11\text{-}1) + a/2[10\text{-}1](111) = a/2[110](001) \tag{20}$$

The finding of a/2<110> dislocations in the {111} planes in TiN is significant and can impact mechanical and physical properties of TiN. Usually, the slip system requirement dictates a/2<110> burgers vector in the {110} plane for TiN (NaCl type crystal structure).

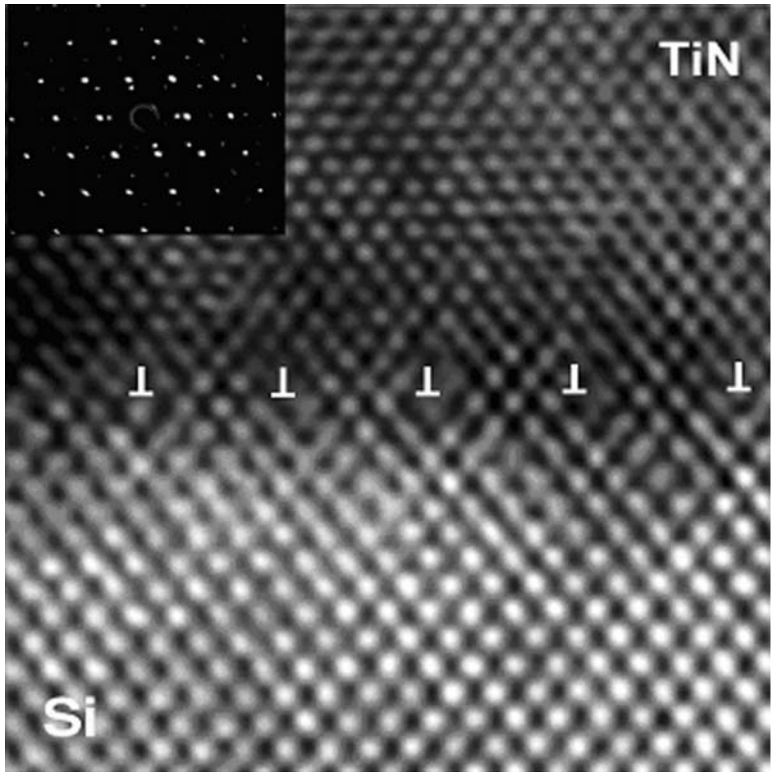

Figure 2-15. Cross section HRTEM image of the TiN/Si interface showing domain matching. The inset is a SAD pattern in a <110> zone showing cube-on-cube epitaxy [5].

References

1. J. Narayan, Metallurgical and Materials Transactions A, **36A**, 277 (2005).
2. H. J. Queisser and E. E. Haller, Science **218**, 945 (1998).
3. S. Mahajan, Acta. Mater. **48**, 137 (2000).
4. M. Ohring, The Materials Science of Thin Films, Academic Press, Inc. (1992).
5. J. Narayan and B. C. Larson, J. Appl. Phys. **93**, 278 (2003).
6. J. W. Mathews, J. Vac. Sci. Technol. **12**, 126 (1975).
7. J. W. Mathews and A. E. Blakeslee, J. Cryst. Growth **27**, 188 (1974).
8. Amit Chugh, PhD Thesis, North Carolina State University (2005).
9. J. Narayan and S. Sharan, Mater. Sci. Eng. **B10**, 261 (1991).
10. F. K. LeGoues, M. C. Reuter, J. Tersoff, M. Hammer, and R. M. Tromb, Phys. Rev. Lett. **73**, 300 (1994).
11. J. Narayan, P. Tiwari, X. Chen, J. Singh, R. Chowdhury, and T. Zheleva, Appl. Phys. Lett. **61**, 1290 (1992).
12. T. Zheleva, K. Jagannadham, and J. Naryan, J. Appl. Phys. **75**, 860 (1994).
13. J. Narayan, U.S. Patent No. 5406, 123 (April 11, 1995).
14. J. Narayan and N. Sudhakar, private communication.
15. A. Gupta, H. Wang, A. Kvit, G. Duscher, and J. Narayan, J. Appl. Phys. **93**, 5210 (2003).

2.5 The FePt system

2.5.1 Introduction and magnetic properties of the FePt material system

The FePt system has been the focus of numerous research studies over the past decade [1-27]. Such extensive study has been motivated mainly because of the superior magnetic properties of FePt. The $L1_0$ ordered FePt phase is a hard magnet with excellent magnetic properties as reported in [1] and references therein. Most importantly, FePt has very high uniaxial magnetocrystalline anisotropy. The bulk value is $K_u = 7 \times 10^7$ erg/cm^3. It also has reasonably high saturation magnetization ($M_s = 1140$ emu /cm^3). The Curie temperature which is as high as 750 °C [1] allows for room temperature ferromagnetic applications [1]. It is also chemically very stable. These properties render the FePt system very attractive for high-density magnetic storage and recording applications. Table 2-3 from ref. [1] compares the magnetic properties of the FePt system with other hard magnetic systems that are potentially suitable for magnetic storage. In addition to the properties discussed above, FePt has high domain wall energy and narrow domain walls. A system with high domain wall energy prefers the formation of single domains. A single domain system is highly effective for magnetic storage (see section 2.1.4). The domain wall width (δ_w) can be evaluated using,

$$\delta_w = \pi \left[\frac{A}{K_u} \right]^{0.5} \tag{21}$$

Considering the stiffness constant A = 10^{-6} ergs/cm and anisotropy constant K_u = 6 x 10^7 ergs/cm^3, the domain wall width (δ_w) was calculated to be 3.9 nm. The domain wall energy (γ_w) was calculated to be 39 erg/cm^2 using the following equation.

$$\gamma_w \cong 4(AK_u)^{0.5} \tag{22}$$

Table 2-3 also lists the single domain particle size (D_c) for various systems. This value is calculated from the following equation.

$$D_c = \frac{1.4\gamma_w}{M_s^2} \tag{23}$$

Where γ_w is the domain wall energy and M_s is the saturation magnetization. Considering γ_w = 39 erg/cm^2 and M_s = 1140 emu/cm^3, D_c is calculated to be 340 nm. This means that a FePt particle as large as 340 nm in size can still remain in a single domain state. Another important parameter shown in Table 2-3 is the minimal stable grain size D_p. If one assumes a storage time constant of 10 years, then the stability criterion is given as [1],

$$K_uV > 60\ kT \tag{24}$$

Where K_u is the anisotropy constant, V is the volume of the grain, k is the Boltzmann constant and T is the temperature. For room temperature storage, T = 300 K and assuming cubic grains, the minimal stable grain size D_p can be calculated as,

$$D_p = (60\ kT/K_u)^{1/3} \tag{25}$$

This value for FePt is about 3 nm. This means that a 3 nm FePt particle will be stable and will have the capacity to store data up to 10 years. FePt particles smaller than 3 nm will be unstable i.e., thermal energy (kT) will become larger than anisotropy energy (K_uV). In this case spins will be inclined towards random flipping rendering the system unsuitable for permanent date storage.

Table 2-3. The properties of the FePt system in comparison with other hard magnetic materials (see text for more description) [1].

- anisotropy field: $H_K = 2K_u/M_S$;
- domain wall width: $\delta_W = \pi\,(A/K_u)^{1/2}$
- domain wall energy: $\gamma_W \cong 4\,(A\cdot K_u)^{1/2}$
- single particle domain size: $D_C = 1.4\,\gamma_W/M_S^2$
- exchange coupling constant $A=10^{-6}$ erg/cm
- minimal stable grain size: $D_p = (60\,k_BT/K_u)^{1/3}$ (τ=10 years)

alloy system	material	K_u (10^7erg/cm^3)	M_S (emu/cm^3)	H_K (kOe)	T_C(K)	δ_W (Å)	γ (erg/cm^2)	D_C (μm)	D_p (nm)
	CoPtCr	0.20	298	13.7	--	222	5.7	.89	10.4
Co-alloys	Co	0.45	1400	6.4	1404	148	8.5	.06	8.0
	Co_3Pt	2.0	1100	36	--	70	18	.21	4.8
	FePd	1.8	1100	33	760	75	17	.20	5.0
$L1_0$	FePt	6.6-10	1140	116	750	39	32	.34	3.3-2.8
phases	CoPt	4.9	800	123	840	45	28	.61	3.6
	MnAl	1.7	560	69	650	77	16	.71	5.1
rare-earth	$Fe_{14}Nd_2B$	4.6	1270	73	585	46	27	.23	3.7
transition metals	$SmCo_5$	11-20	910	240-400	1000	22-30	42-57	.71-.96	2.7-2.2

2.5.2 Crystal structure

The equilibrium phase diagram of FePt is shown in Fig. 2-16 [2,3]. Three important phases exist in the FePt system: $FePt_3$, FePt and Fe_3Pt. The $FePt_3$ and Fe_3Pt phases have the face centered cubic $L1_2$ ordered structure. These phases are magnetically soft. Our interest lies in the magnetically hard FePt phase. As seen from the phase diagram FePt exists in two important phases: the ordered phase (γ_1) and the disordered phase (γ). The ordered phase has a $L1_0$ type of crystal structure [4], which is also known as the face centered tetragonal structure or the CuAu type crystal structure. The space group is P4/mmm. Figure 2-17a shows the $L1_0$ ordered FePt unit cell. The Fe and Pt atoms occupy specific locations in the unit cell and under an equiatomic composition the Fe and Pt atomic planes are stacked alternatively along the c-axis. It is important to realize that ordering tends to make the FePt unit cell slightly tetragonal in nature. The lattice parameters for a bulk crystal are a = 3.838 Å and c = 3.715 Å. The $L1_0$ structure is responsible for the superior magnetic properties of FePt. The uniaxial magnetocrystalline anisotropy is maximum along the c-axis and its value is about $K_u = 7 \times 10^7$ ergs/cm^3 [1]. In comparison the disordered FePt phase is magnetically soft with a much lower cubic anisotropy constant ($K_1 = 6 \times 10^4$ ergs/cm^3) [5]. It has a FCC crystal structure and as shown in Fig. 2-17b the Fe and Pt atoms are located randomly in the unit cell. The disordered phase exists above the transformation temperature. For an equiatomic composition the transformation temperature is about 1550 °C. It is also important to note that the $L1_0$ ordered phase can be formed in the composition regime that varies from about $Fe_{38}Pt_{62}$ to $Fe_{62}Pt_{38}$.

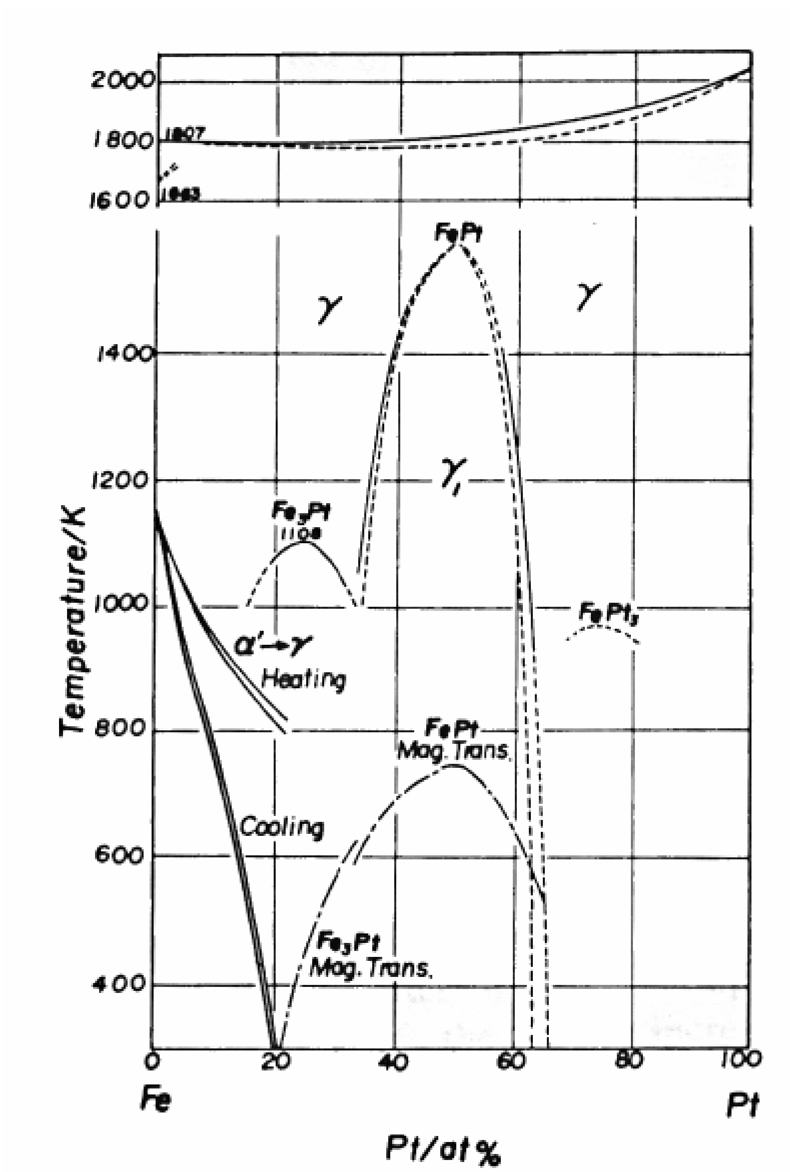

Figure 2-16. Equilibrium phase diagram of the FePt system [2].

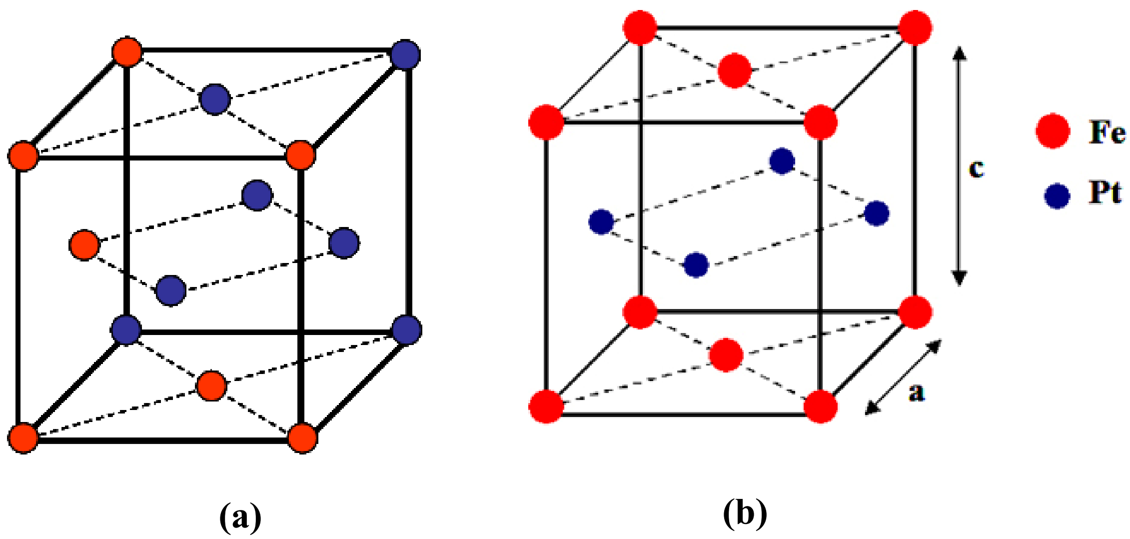

Figure 2-17. Schematic illustration of the unit cell for the (a) disordered and (b) $L1_0$ ordered $Fe_{50}Pt_{50}$ system.

2.5.3 FePt thin films and their properties

Early work on the magnetically hard FePt system in the bulk form was done by Magat et. al. [6]. Over the past few years FePt has been studied mainly in the thin-film form because of potential magnetic storage applications. The magnetic properties of the FePt system depend largely on its microstructure, which mainly depends mainly on the growth process and processing temperature. The FePt system has been synthesized in various forms including epitaxial thin films [7-9], textured non-epitaxial films [10] and nano structures/particles/islands [11-13] using a wide variety of processing techniques. Some popular synthesis techniques used are; sputtering [7-9], MBE [14,15] and chemical synthesis [11,13]. Each technique has its own advantages and disadvantages in terms of the morphology and crystallographic orientation obtained. For example, FePt nanoparticles have been successfully synthesized by chemical routes [11] and ion implantation [12], but such techniques do not offer control over orientation, which is of prime importance if we have to exploit the magnetocrystalline anisotropy in the system. The chemical routes offer excellent control over size and spatial resolution but require an additional annealing step to impart texture and desired order in the nanostructures [11,13]. However, the annealing process can be detrimental, as it can cause interfacial diffusion, destroy self-assembly and induce unwanted nanoparticle coarsening and agglomeration. It is important to realize that physical deposition methods based on substrate controlled epitaxy are more suitable for synthesizing crystallographically orientated FePt nanostructures. Growth processes such as MBE, sputtering and PLD fall into this category. Until now single crystal MgO substrates have been used to synthesize c-axis oriented epitaxial FePt thin films [7,8,9,14]. However, MgO is hygroscopic and high costs are incurred in using MgO single-crystal substrates. This makes MgO an unattractive candidate for the magnetic recording industry. The unique feature of our study stems from the use of single crystal Si (100) substrates. Silicon is cheap and readily available, but most importantly, by using Si (100) we potentially provide for direct integration with the present day microelectronic devices.

The magnetic properties of the FePt system depend on its morphology, i.e. continuous films exhibit different properties when compared to nanoparticles. Size reduction to the nanoregime can lead to a huge change in magnetic properties. Some properties that are associated with the size reduction are: transition to single domain state, large coercivity, low saturation magnetization and high Curie temperature [16-19]. Individual nanoparticles can attain single domain state, which affects the domain reversal mechanisms [16-19]. For the FePt system increase in growth temperature changes the growth mode from 2D to 3D, i.e. at lower temperatures continuous thin films are formed and at higher temperatures individual nano islands are formed [20]. Takahashi et. al. [20] have reported the growth of isolated 30 nm thick FePt particles on MgO at 700° C. These particles are completely ordered and have single domains. This unique microstructure gives rise to magnetically isolated FePt particles with a coercivity of 4 T. Magnetic properties of the FePt system also depend on the film thickness [8,21]. In general, the coercivity decreases with increasing thickness. Thick films (300-400 nm) behave much like the bulk system [22].

Researchers have also found that twins and anti phase domains (APD) in the FePt system affect the magnetic properties [23-25]. The twins and APDs are formed to relieve the strain that builds up in the system due to the disorder-order transformation. During growth the disorder-order transformation can occur from multiple nucleation sites and when these domains grow and come together an anti phase boundary is formed [26].

Defects such as twins and anti phase domains can act as domain pinning sites and lead to improved coercivity values [24,25].

The extent of ordering also determines the magnetic properties of the FePt system [7,9,16]. The order parameter (S) quantifies the extent of ordering. The order parameter is calculated from X-ray diffraction experiments, depending upon the ratio of intensities of the fundamental and superlattice peaks. This procedure is described in chapter 4. Usually the coercivity increases with an increase in the order parameter [7,9,16]. The order parameter is a function of growth temperature. A higher temperature provides enough energy to drive the Fe and Pt atoms to the right locations in the unit cell and thus leads to improved ordering. Ordering is also dependent to some extent on the composition of the FePt system. Shima et. al. [27] have found that a Pt rich off-stoichiometric system orders at lower temperatures. The composition of the Fe_xPt_{1-x} system also affects magnetic properties such as coercivity and anisotropy constant [7,28].

References

1. D. Weller, A. Moser, L. Folks, M. E. Best, W. Lee, M.F. Toney, M. Schwickert, J. U. Thiele, and M.F. Doerner, IEEE Trans. Magn. **36**, 10 (2000).
2. K. Watanabe and H. Masumoto, Trans. Jap. Inst. Met. **24**, 627 (1983).
3. Binary Alloy Phase Diagrams, edited by T. B. Masslaski, H. Okamoto et. al. 2nd edition, ASM International (1993).
4. H. Lipson, D. Schoenburg, and G. V. Stupart, J. Inst. Metals, **67**, 333 (1941).
5. V. G. Pynko, A. S. Komalov, and L. V. Ivaeva, Phys. Stat. Sol. **63a**, K127 (1981).
6. L. M. Magat, G.V. Ivanova, L. V. Solina, N. N. Schgoleva, and Y. S. Shur, Fiz. Jap. Inst. Met. **29**, 400 (1970).
7. K. Barmak, J. Kim, L.H. Lewis, K.R. Coffey, M.F. Toney, A.J. Kellock, and J.U. Thiele, J. Appl. Phys. **98**, 033904 (2005).
8. J.U. Thiele, L. Folks, M.F. Toney, D.K. Walker, J. Appl. Phys. **84**, 5686 (1998).
9. F. Casoli, F. Albertini, L. Pareti, S. Fabbrici, L. Nasi, C. Bocchi, and R. Ciprian, IEEE Trans. Magn. **41**, 3223 (2005).
10. H. Zeng, M.L. Yan, N. Powers, D.J. Sellmyer, Appl. Phys. Lett. **80**, 2350 (2002).
11. S. Sun, C.B. Murray, D. Weller, L. Folks, and A. Moser, Science, **287**, 1989 (2000).
12. C.W. White, S.P. Withrow, K.D. Sorge, J.D. Budai, J.R. Thompson, and L.A. Boatner, J. Appl. Phys. **93**, 5656 (2003).
13. Z. Jia, S. Kang, S. Shi, D.E. Nikles, J.W. Harrell, M. Shamsuzzoha, J. Appl. Phys. **99**, 08E904 (2006).

14. R.F.C. Farrow, D. Weller, R.F. Marks, M.F. Toney, D.J. Smith, M.R. McCartney, J. Appl. Phys. **84**, 934 (1998).

15. T. Itoh, T. Kato, S. Iwata, S. Tsunashima, IEEE Trans. Magn. **41**, 3217 (2005).

16. N. A. Spaldin, Magnetic materials: Fundamentals and device applications, Cambridge University Press (2003).

17. R. H. Kodama, J. Magn. Magn. Mater. **200**, 359 (1999).

18. O. Fruchart, J. P. Nozieres, W. Wernsdorfer, and D. Givord, Phys. Rev. Lett. **82**, 1305 (1999).

19. D. Kumar, J. Narayan, T. K. Nath, A. K. Sharma, A. Kvit, and C. Jin, Solid State Communications, **119**, 63 (2001).

20. Y. K. Takahashi, K. Hono, T. Shima, and K. Takanashi, J. Magn. Magn. Mater. **267**, 248 (2003).

21. Y. Ide, T. Goto, K. Kikuchi, K. Watanabe, J. Onagawa, H. Yoshida, and J. M. Cadogan, J. Magn. Magn. Mater. **177-181**, 1245 (1998).

22. J. A. Aboaf, T. R. McGuire, S. R. Herd, and E. Klokholm, IEEE Trans. Magn. **20**, 1642 (1984).

23. B. Zhang, M. Lelovic, and W. A. Soffa, Script. Met. Mat. **25**, 1577 (1991).

24. M. H. Hong, K. Hono, and M. Watanabe, J. Appl. Phys. **84**, 4403 (1998).

25. Z. R. Dai, S. Sun, and Z. L. Wang, Nano Letters, **1**, 443 (2001).

26. D. A. Porter and K. E. Easterling, Phase transformation in Metals and Alloys, 2^{nd} edition, (1992).

27. T. Shima, T. Seki and, K. Takanashi, J. Magn. Soc. Jpn. **28,** 501 (2004).

28. T. Seki, T.Shima, K. Takanashi, E. Matsubara, and K. Hono, Appl. Phys. Lett. **82**, 2461 (2003).

Chapter 3

3 Experiments

3.1 Growth

Thin film and nanostructure growth in this study was performed by pulsed laser deposition. The theory and principle involved in this process has been discussed in detail in the previous chapter (section 2.2). This section will deal with the experimental parameters involved during thin film growth by pulsed laser deposition. The experimental setup of the PLD system is illustrated schematically in Fig. 3-1. The KrF excimer laser source used was the LPX 210 from Lambda Physik. The laser wavelength was 248 nm and pulse duration was 25 ns. The laser can operate at a maximum energy of 674 mJ at 24 KV. The laser beam is directed into the vacuum chamber using an aperture, mirror and a lens. The mirror is used to control the position at which the laser strikes the target inside the chamber. The lens is used to focus the laser beam on the target. Essentially, the lens offers control over the spot size. The laser beam enters into the vacuum chamber through the laser window. A quartz laser window with a CaF_2 coating is used for this purpose. The CaF_2 coating minimizes losses due to reflection. The laser beam is directed such that it strikes the target at an incident angle of 45°. Due to laser-solid interaction a plume is formed and deposition occurs onto the substrate.

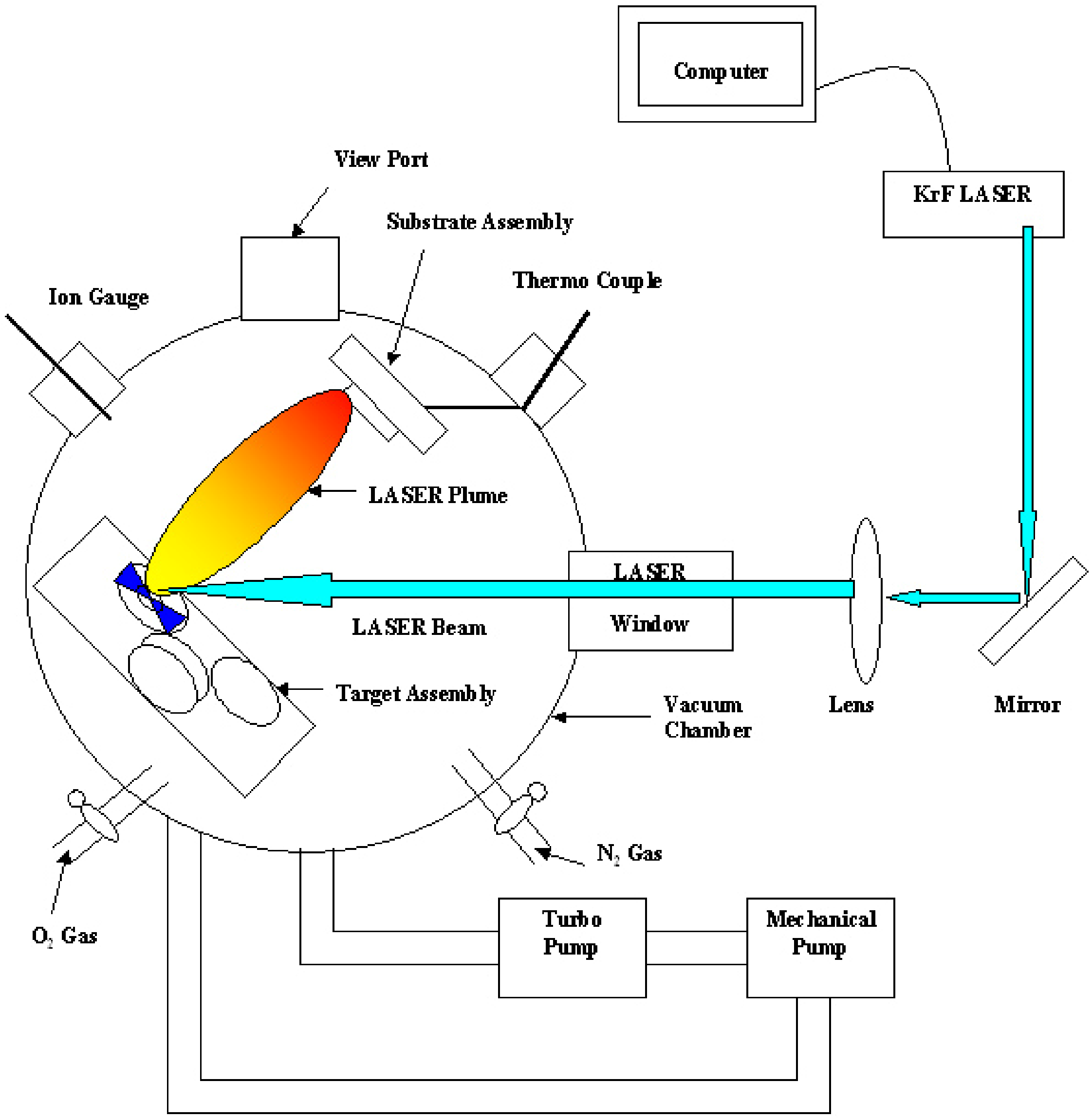

Figure 3-1. Schematic illustration of the PLD setup.

The PLD chamber holds a target assembly that can be mounted and detached from the top. The target carrousel is designed to hold up to four targets. The target carousel is connected to a hand-driven motion controller in order to position any required target in the path of the laser beam. The multi-target assembly enables easy growth of multi-layered thin films. The individual targets themselves are designed to rotate by using a small driving motor. By rotating the target we ensure that the laser beam strikes the target at different locations. Thus uniform ablation of the target occurs and exfoliation is reduced.

The substrate assembly is located parallel to the target surface at a distance of 4.5 cm. It has been found that with increase in substrate target distance, the maximum thickness at the center of the film decreases rapidly [1,2]. However, the uniformity of film in terms of its thickness improves with increase in substrate target distance. Singh et. al. [1,2] have reported the variation of the maximum thickness of the film with the substrate-target distance (d) as d^{-p}. Here p is the expansion coefficient, with a value of 3 for three dimensional spherical expansion and a value of 1 for linear expansion in one dimension. The value of p is also a function of spot size [1,2]. Larger spot sizes make the plume more forward directed, i.e. a more linear type of expansion. For smaller spot size the plume is spherical. This can be explained in terms of a $(\cos \theta)^n$ type of dependence [1,2]. For a forward directed plume n = 8-12. For a point source, like in the case of e-beam evaporation, n will be equal to 1. In such a case the plume will be largely spherical with minimal forward directedness.

In our study, the spot size for TiN growth is usually large (0.1 cm^2) and hence the plume is relatively more forward directed. The forward directed TiN plume helps maintain stoichiometry and nullifies the effect of the high vapor pressure of nitrogen. Kinetic calculations from the oxidation reaction of SiO_2 reveals that, at base pressure of 10^{-7} torr and temperature of 600 °C a monolayer of SiO_2 can be formed. During PLD, the forward directed TiN plume is highly energetic and will sputter away any SiO_2 formed on the Si surface. Additionally, due to the high energy of the plume the impurities get pushed out and TiN forms on a bare and pure Si surface. Due to these reasons, epitaxial growth of TiN on Si is possible at a relatively low temperature of 600 °C by PLD.

For FePt growth, a smaller spot size (0.06 cm^2) is used, mainly to increase the energy density. Generally, laser ablation of metals requires a larger energy density [3]. In the case of metals, laser-solid coupling may be difficult when the surface is shiny. A smooth shiny surface causes losses due to reflection. In this study, both the Fe and Pt targets were mechanically polished with a large grit size paper (240-400) to roughen the surface. The TiN target also needs maintenance. After 3 to 4 growths the TiN target shows a shiny silver color deviating from the usual golden yellow color. This color change is attributed to Ti enrichment. To remove this Ti enriched layer, the target is polished with a 600 grit paper until a yellow colored surface shows. The polished TiN target has to be cleaned thoroughly (with methanol and dry nitrogen gas) to remove any grit particles that are sticking on the surface.

It is important to realize that a clean Si surface is absolutely essential for epitaxial growth. So special care is taken to clean the Si substrate. The Si substrate is first ultrasonically degreased using acetone for 2-3 minutes. This is followed by a methanol rinse. The spotless Si surface is then etched with HF for 40-50 seconds. This removes the native oxide layer and forms a hydrogen terminated surface. The cleaned Si substrate is then loaded into the vacuum chamber as soon as possible. The substrate temperature is slowly heated up to 200 °C. Once the required vacuum is reached, the temperature is quickly ramped to 600 °C and film deposition initiated in order to minimize oxidation of the Si surface.

Ablation and deposition rates of Fe and Pt were studied individually. It was found that growth rate of Pt was greater than Fe. Accordingly, a segmented geometry was used consisting of two individual pieces of Fe and Pt with respective areas crossed to produce FePt with compositions varying from $Fe_{40}Pt_{60}$ to $Fe_{50}Pt_{50}$. The growth parameters for TiN and FePt used in this study are listed in Table 3-1. The base pressure was maintained at 10^{-7} torr.

Table 3-1. Growth parameters for TiN and FePt.

	Energy density	Temperature (°C)	Repetition rate	Growth time
TiN	2 J/cm^2	600-620	10 Hz	4-6 min
FePt	4-5 J/cm^2	500-600	5-15 Hz	25-300 sec

3.2 Structural characterization

The microstructural characterization of the PLD grown samples were done by X-ray and TEM. Compositional analysis was done by RBS. The following sections describe these techniques in brief.

3.2.1 X-ray diffraction (XRD)

X-ray diffraction (XRD) was used to study the crystal structure and orientation of our samples. This technique also provides information about the phase composition, lattice parameter, grain size and lattice strain. Specifically, in this study XRD was used to determine the presence of $L1_0$ order in the FePt system. The extent of ordering can be quantified by the order parameter (S). The procedure to calculate the order parameter is described chapter 4.

The XRD technique is based on diffraction governed by the Bragg's law [4]. Diffraction typically occurs when waves interact with a periodic structure. It is important to realize that the wavelength of the wave should be about the same as the repeat distance of the periodic structure for diffraction to occur [4]. Inter-atomic distances are of the order of a few angstroms. X-rays have wavelengths of the same order and hence they are used to investigate the crystals. When an X-ray beam is incident on a crystal it interacts with the parallel plane of atoms either constructively or destructively depending upon the path difference. Bragg's law is satisfied when the waves interfere constructively and the following condition is met [4].

$$n\lambda = 2d \sin\theta \tag{1}$$

Where n is an integer indicating the order of reflection, λ is the wavelength of the X-ray beam, d is the inter-planar spacing and θ is the incident angle. X-ray diffraction is carried out using a diffractometer. For this study we used a Rigaku Geigerflex diffractometer with Cu Kα radiation (λ = 1.54 Å). Essentially, a diffractometer consists of an X-ray source, a monochromator, a slit, a sample holder and a detector. The schematic of an XRD system is shown in Fig. 3-2. The X-ray source is a tube consisting of a tungsten filament (cathode) and a Cu target (anode). A huge potential difference (~30 KV) causes the filament to emit electrons, which are accelerated to collide with the cathode in order to produce X-rays. Slits are used to adjust the shape and size of the beam. The detector measures the intensity of the diffracted beam through an angle of 2θ. Generally in a θ-2θ scan, the sample moves by θ and the detector moves by 2θ.

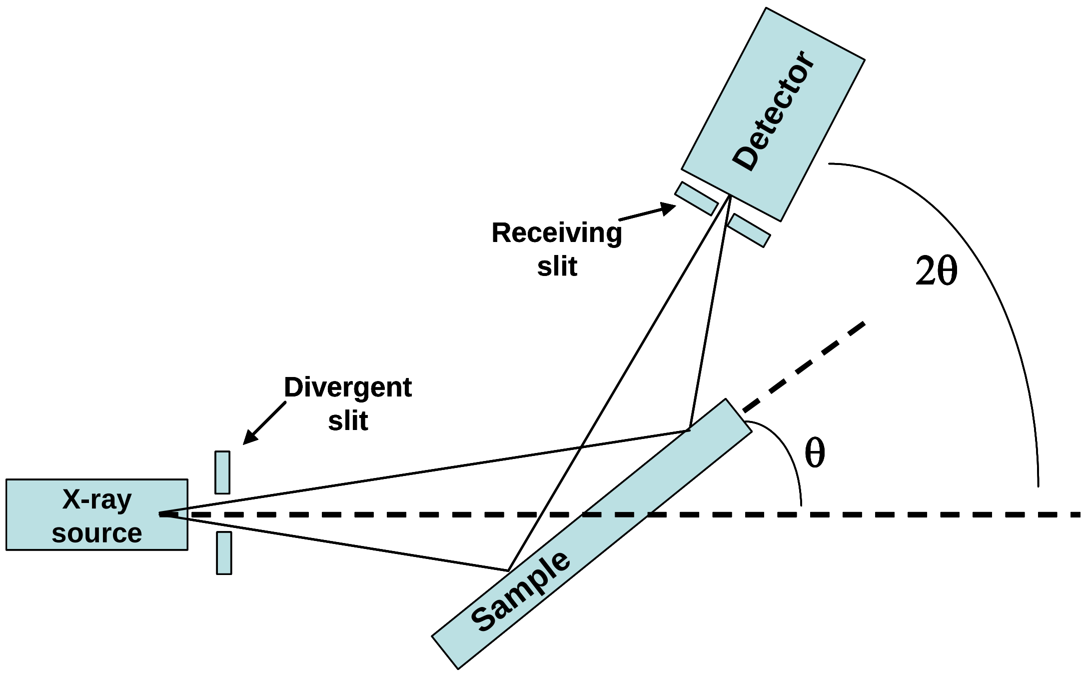

Figure 3-2. Schematic illustration of the XRD θ-2θ scan.

The X-ray diffraction technique provides crystal information from a relatively large area of the sample. It is a non-destructive technique and requires minimal sample preparation. The X-ray holder used in this study is shown in Fig. 3-3. The sample is mounted onto the holder using clay. Care needs to be taken to mount the sample such that it is in the plane of the sample holder with no tilt. The sample surface should be relatively clean. It is important to realize that in the XRD technique only the planes parallel to sample surface contribute to the signal. For a single crystalline sample only one set of planes are parallel to the surface. So an XRD scan of a single crystal should have only one peak and higher order peaks of the same family. In the case of a poly crystalline film, several planes belonging to different grains will be parallel to the sample surface. Hence the XRD scan of a poly sample will have numerous peaks representing various planes. An amorphous sample will have a wide diffused peak at about 20°.

Figure 3-3. Sample holder used for XRD.

Although, the XRD technique provides easy and quick information about crystal orientation and phase composition it suffers from its own disadvantages. Importantly, it gives information about texturing only in the growth direction. If the amount of material is less than 10 % by weight, detection by X-ray becomes difficult. Particles or precipitates with sizes in the nano-regime may not be detected. For exact orientation relationship and atomic resolution characterization transmission electron microscopy is necessary.

3.2.2 Transmission electron microscopy (TEM)

For atomic scale characterization and exact orientation relationship TEM is the most effective and direct technique available. TEM can also be used to investigate defects such as dislocations and their burgers vectors, stacking faults, twins and precipitates. Chemical composition and subsequent qualitative analysis can be done using electron energy loss and X-ray spectroscopy. Specifically, in our study TEM was used to study the size, shape and spatial orientation of the FePt islands. Selected area diffraction patterns in the <110> and <001> zones were compared and analyzed to study the $L1_0$ order in the FePt system. High resolution cross section imaging was used to study domain matching epitaxy at the FePt/TiN interface. For this purpose we used a JEOL 2010F transmission electron microscope with a point-to-point resolution of 1.8 Å. A Gatan imaging filtering system was used for HRTEM.

The TEM uses an electron beam as a probe. Typically, a TEM operating at 200 KV generates an electron beam with wavelength $\lambda = 0.03$ Å [5]. According to the Raleigh criterion (shown below) resolution is directly proportional to wavelength [5].

$$\delta = 0.61\lambda / \beta \qquad (2)$$

Here δ is the resolution, λ is the wavelength and β is the semi-angle of collection of the magnifying lens. The smaller the wavelength the better the resolution. Hence resolution obtained in a TEM is in the order of few angstroms, i.e. atomic level resolution. Essentially, a TEM consists of two main components; the illumination system and the imaging system. The illumination system consists of the electron gun and electromagnetic lenses that focus the beam onto the sample [5,6]. The electron beam interacts with the specimen. The imaging system detects the scattered electrons to form the image/diffraction pattern. The important TEM techniques used in this study were; diffraction, bright field and dark field imaging and high resolution TEM.

Diffraction: The TEM operates in two modes; the diffraction mode and the image mode. Diffraction patterns can be formed on the screen by placing the back focal plane on the objective plane of the intermediate and projector lens [5,6]. For thin samples information obtained in the diffraction mode is mainly from elastically scattered electrons. Since the electron wavelength is small, the Ewald sphere will have a large radius. Consequently, almost a plane section of the reciprocal lattice (zero order Laue zone) is observed during electron diffraction [5,6]. Generally, a parallel beam of electrons is used for diffraction (selected area diffraction). If information from a smaller area is required, then a convergent beam of electrons can be used (convergent beam electron diffraction) [5]. Single crystal samples scatter the electron coherently and thus produce a spot diffraction pattern. Polycrystalline samples produce ring-like patterns. Sample with nano-sized grains produce spotty discontinuous rings. The diffraction pattern of an amorphous sample will show a diffused ring.

Imaging: Bright field imaging is done using the transmitted beam of electrons. This is done by inserting the objective aperture in the back focal plane (the plane where the diffracted image is formed) [5,6]. The objective aperture then allows only the transmitted beam through for bright field imaging. The dark field imaging is done when the diffracted beam is allowed to pass and the transmitted beam is blocked. The best contrast is obtained in a two beam condition [5,6]. In this condition the sample is titled such that only one diffracted beam is strong enough to remain. Essentially, two spots remain in the diffraction pattern the central transmitted spot and another strong diffraction spot with a known g-vector. If the objective aperture is placed on the central spot we obtain a bright field image. If the sample is tilted such that the diffracted beam passes through the aperture then we obtain a dark field image.

HRTEM: This technique allows lattice imaging of the sample. Here, atomic level resolution is obtained by allowing many beams to pass through the objective aperture. The diffracted beams interfere with the direct beam resulting in a phase contrast [5,6]. This phase contrast contributes to a high resolution TEM image. For proper analysis of a HRTEM image the sample should tilted to an exact zone. Choosing the proper defocus condition (based on the contrast transfer condition) is also of prime importance for good resolution of a HRTEM image. A first Scherzer defocus condition with minimal objective lens astigmatism is used to obtain a good HRTEM image.

TEM sample preparation

The cross section TEM samples were prepared by a series of steps including mechanical polishing, dimpling and ion-milling. To begin with, two small sample pieces (about 4 x 4 mm) were stuck together with the film side facing each other. An M-Bond 610 adhesive was used to stick the samples together. The sample was then mounted onto a pyrex stub. Then the sample was mechanically polished until a mirror like surface was obtained. For this purpose, a series of emery papers with reducing grit sizes were used. Final polish was done using a 0.1 and 0.05 micron alumina slurry. The sample was then flipped over. Now the sample was thinned down to a thickness of about 100 microns from the rough side. A smooth grit paper (1200-4000) was then used to bring down the thickness of the sample from 100 to 70 microns. The sample was then dimpled using a Gatan dimpling machine. Dimpling involved grinding with a Cu wheel and further polishing with a cloth wheel. Diamond pastes of 6, 3 and 1 micron sizes were used during dimpling. After dimpling up to a thickness of 15-20 microns, ion-milling was performed. For this purpose a precision Gatan 691 PIPS ion milling machine was used. A small hole at the interface was formed by sputtering the sample with Ar ions. The energy of the Ar ion beam was maintained at ~ 5 KeV with a tilt angle of 5°. For plane view TEM samples, the sample was stuck onto the stub with film side facing down. The sample was then mechanically thinned, dimpled and ion milled until electron transparency was achieved.

3.2.3 Rutherford backscattering (RBS)

Rutherford backscattering spectroscopy (RBS) is a powerful characterization technique used to investigate the composition, concentration and depth profiles in thin films. It also gives information about epitaxial quality and thickness of the film. In our study, RBS was used to determine the composition of the FePt film. The RBS system at UNC Chapel Hill (under the care of Prof. N. Parikh) was used for this purpose. The RBS system essentially consists of three main components; an ion source (usually He^{2+} ions), a linear accelerator (that accelerates the ions to energies as high as 1-3 MeV energy) and a detector (that detects backscattered ions). The system in this study uses a van de Graaff accelerator to produce 1.6 MeV He^{2+} ions. The incident ions are elastically scattered via columbic interactions with the nuclei of the atoms in the sample. The ions that are backscattered at angles greater than 165° are captured by the detector. The number and energy of the ions that are backscattered are recorded and analyzed to derive the required information. The data processed by the RBS technique is usually plotted in terms of the yield and energy (see figure 3-4). The concentration of an element is directly proportional to the yield and and inversely proportional to the square of the atomic number. Figure 3-4 is an RBS spectrum obtained for the FePt/TiN/Si system. The composition of FePt from this spectrum can be calculated using the following equation.

$$\frac{Pt}{Fe} = \left(\frac{A_{Pt}}{A_{Fe}}\right)\left(\frac{Z_{Fe}}{Z_{Pt}}\right)^2 \qquad (3)$$

Where A represents the area under the corresponding peak and Z is the atomic number. In this case the composition was calculated to be $Fe_{50}Pt_{50}$.

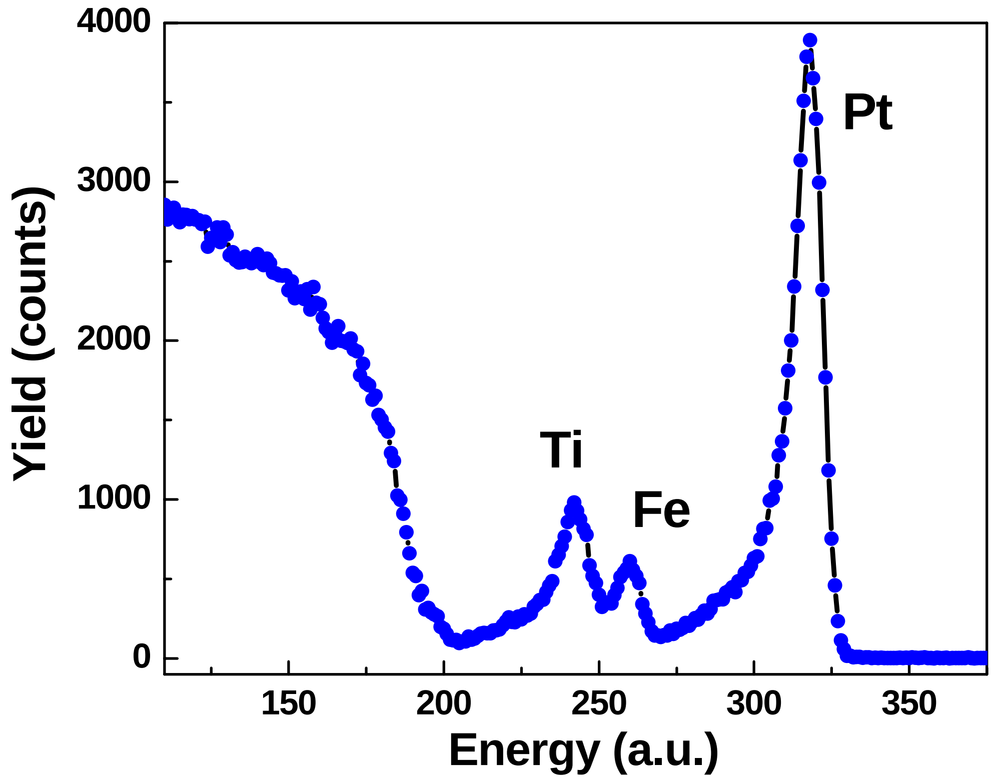

Figure 3-4. RBS spectrum of the $Fe_{50}Pt_{50}$ system.

3.3 Magnetic characterization

Magnetic characterization was performed by using a superconducting quantum interference device (SQUID). A 4 Tesla Quantam Design MPMS system was used for this purpose. A SQUID is designed based on the principle of the Josephson effect and it can detect extremely small magnetic signals in the range of 10^{-10} Oe [7]. It consists of a Josephson junction made from a superconducting ring with a gap that is filled with an insulating material (see Fig. 3-5). In the presence of a small magnetic field superconducting electrons tunnel thorough the insulating barrier creating small changes in the critical current density that are recorded and analyzed for the output signal.

Before measuring the MH loops, the samples were demagnetized by oscillating the magnetic field around the zero value. MH measurements were done over five quadrants. In most cases the MH loops were corrected for a substrate contribution. This was done by fitting the diamagnetic slope and subtracting it from the raw magnetic moment values.

The magnetoresistance measurements were performed using the Quantum Design physical property measurement system (PPMS). The transport measurements were done using a four probe measurement configuration. The MR measurements were done in two different configurations. In the in-plane configuration, the magnetic field was parallel to the current and the sample surface. In the perpendicular configuration, the magnetic field was perpendicular to current and the perpendicular to sample surface. In other words the current direction remains parallel to sample surface in both cases, while the field is switched perpendicular and parallel to the sample surface.

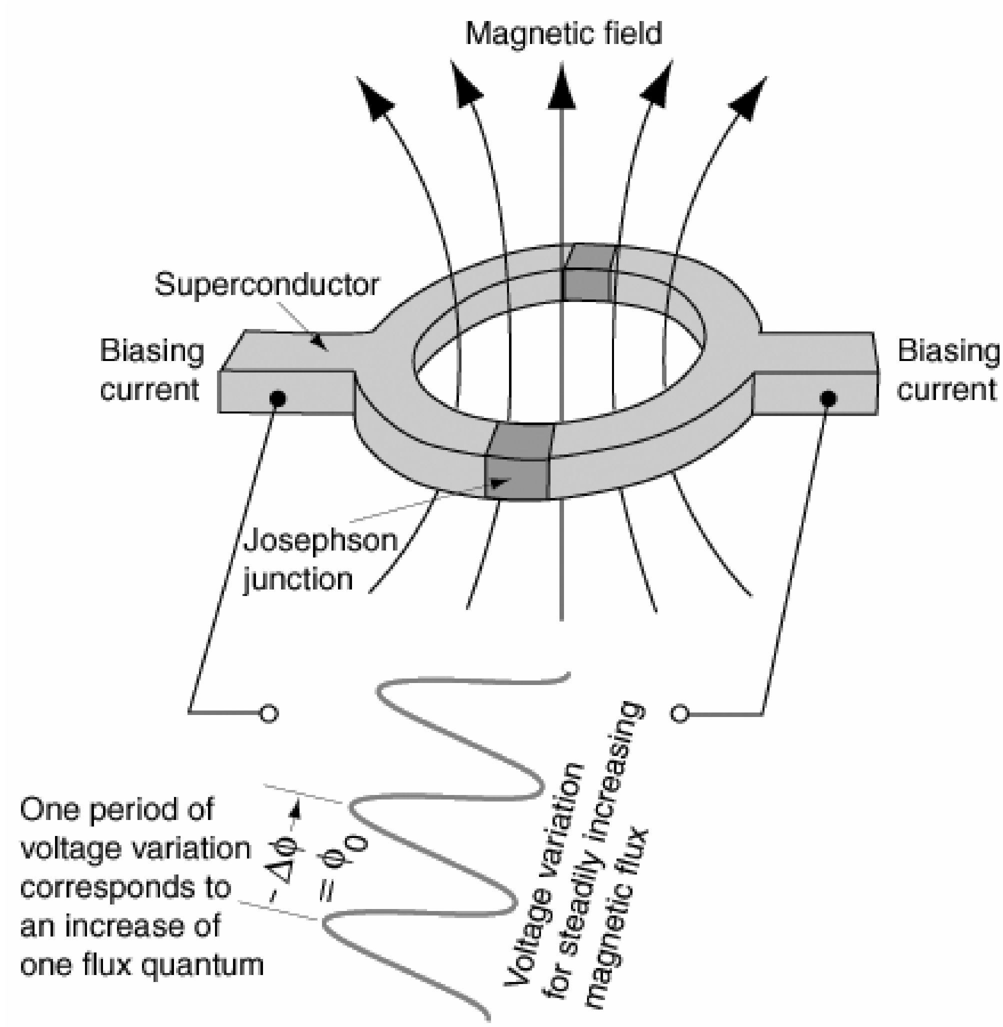

Figure 3-5. Schematic illustration of a Josephson junction in a SQUID [8].

References

1. R. K. Singh and J. Narayan, Phys. Rev. B **41**, 8843 (1990).
2. R. K. Singh, O. W. Holland, and J. Narayan, J. Appl. Phys. 68, **233** (1990).
3. Pulsed Laser Deposition of Thin Films, edited by D. B. Chrisey and G. K. Hubler, Wiley-Interscience, New York, 1994.
4. B. D. Cullity, Elements of X-Ray Diffraction, Addison-Wesley Publishing Co. Inc. (1982).
5. D. B. Williams and C. B. Carter, Transmission Electron Microscopy, Plenum Press, New York (1996).
6. G. Thomas and M. J. Goringe, Transmission Electron Microscopy of Materials, John Wiley and Sons, Inc (1981).
7. N. A. Spaldin, Magnetic materials: Fundamentals and device applications, Cambridge University Press (2003).
8. http://hyperphysics.phy-astr.gsu.edu/hbase/solids/squid.html

Chapter 4

4 $L1_0$ ordered epitaxial FePt (001) thin films on TiN/Si(100) by pulsed laser deposition

4.1 Abstract

Epitaxially oriented magnetic FePt (001) thin films were grown on Si (100) substrates with TiN as a template buffer by using pulsed laser deposition. The epitaxial relationship and presence of $L1_0$ order were studied by X-ray diffraction and further confirmed by detailed transmission electron microscopy. The effectiveness of using TiN as a template, for an epitaxial magnetic FePt heterostructure integrated with silicon and for inducing $L1_0$ order in the FePt films, has been demonstrated. The following epitaxial relationship was obtained in the FePt thin film: FePt (001) <001>‖ TiN (100) <001> ‖ Si (100) <001>. The 9.5 % misfit strain between FePt and TiN is relaxed by domain matching epitaxy where 10/9 and 11/10 domains alternate across the interface. The composition of the FePt system, as determined by Rutherford backscattering, was $Fe_{41}Pt_{59}$. Magnetic measurements show that the ordered FePt films are predominantly perpendicularly magnetized and have high values of coercivity and squareness suitable for magnetic recording devices.

4.2 Introduction

Synthesis and study of magnetic FePt thin films has received considerable attention in recent years owing to its potential use in the high-density recording media [1-3]. The FePt material system exhibits excellent magnetic properties such as high uniaxial magnetocrystalline anisotropy (7×10^7 erg/cm^3), high coercivity, high saturation magnetization and good chemical stability [4]. The superior magnetic properties of the FePt system arise due to its ordered $L1_0$ structure and under equiatomic composition the ordered structure has Fe and Pt atomic planes stacked alternatively along the c-axis. Naturally, the motivation here is to synthesize ordered (001) epitaxial FePt thin films, so that we can take advantage of the high degree of magentocrystalline anisotropy along the [001] direction and put it to use for perpendicular magnetic recording.

To date, in most studies single crystal MgO substrates have been used to synthesize epitaxial (001) FePt thin films [1,2,3,5]. However, MgO is hygroscopic and high costs are incurred in using MgO single-crystal substrates. This makes MgO an unattractive candidate for the magnetic recording industry. The unique feature in the present study stems from the usage of single crystal Si (100) substrates. Silicon is cheap and readily available, but most importantly, by using Si (100) we achieve integration with the present day microelectronic devices. In our study, we have synthesized $L1_0$ structured epitaxial (001) FePt thin films on Si (100) using TiN as a template buffer. It is important to note that growth of FePt directly on Si is not desirable due to various issues including the diffusion of Fe and Pt into Si and the preferred (111) growth of FePt. Hence, the need of a buffer layer arises to control the growth orientation of FePt. Insertion of TiN as the template buffer leads to FePt growth oriented along the magnetically hard [001]. Additionally, TiN is metallic (ρ = 15 $\mu\Omega$.cm) and it provides an excellent diffusion barrier [6]. Sputter deposition and molecular-beam epitaxy have been the most common processing techniques to form $L1_0$ ordered FePt films, as reported in [1] and references therein. In the present work, we have shown that pulsed laser deposition can also be used to synthesize high quality epitaxial FePt thin films. Keeping in mind that the processing temperatures need to be low in the magnetic recording industry [7], an intermediate growth temperature of 500° C, with no further post-annealing treatments, has been optimized to grow the ordered FePt (001) thin films.

4.3 Experiment

A KrF excimer laser with a wavelength of 248 nm and pulse width of 25 ns was used for pulsed laser deposition. Prior to deposition, the Si (100) substrates were taken through a cleaning procedure that involved ultrasonic degreasing with acetone, rinsing with methanol and finally etching with hydrofluoric acid (HF) to remove any native oxide layer and to form a hydrogen terminated surface. A clean Si surface is absolutely essential for growth of the epitaxial TiN template buffer. The TiN buffer layers were grown at a temperature of 600° C and an energy density of 2 J/cm^2. Growth parameters used for the FePt films were as follows; base pressure 10^{-7} torr, energy density ~5 J/cm^2

and growth temperature 500-600 °C. The growth rate for FePt was about 0.08 nm/s. X-ray diffraction (XRD) experiments were done using a Rigaku Geigerflex Diffractometer with Cu K_{α} radiation and a graphite monochromator. Transmission electron microscopy was done using a JEOL 2010F TEM, operating at 200 KV, with a resolution of 0.18 nm. Magnetic property measurements were done using a superconducting quantum interference device (SQUID). The composition of the FePt thin film was determined by Rutherford backscattering spectrometry (RBS), where scattering yield is proportional to Z^2 (Z is the atomic number). Figure 4-1 shows the RBS yield as a function of 1.6 MeV incident helium ions. From the fit to the yield curve, the composition was determined to be $Fe_{41}Pt_{59}$.

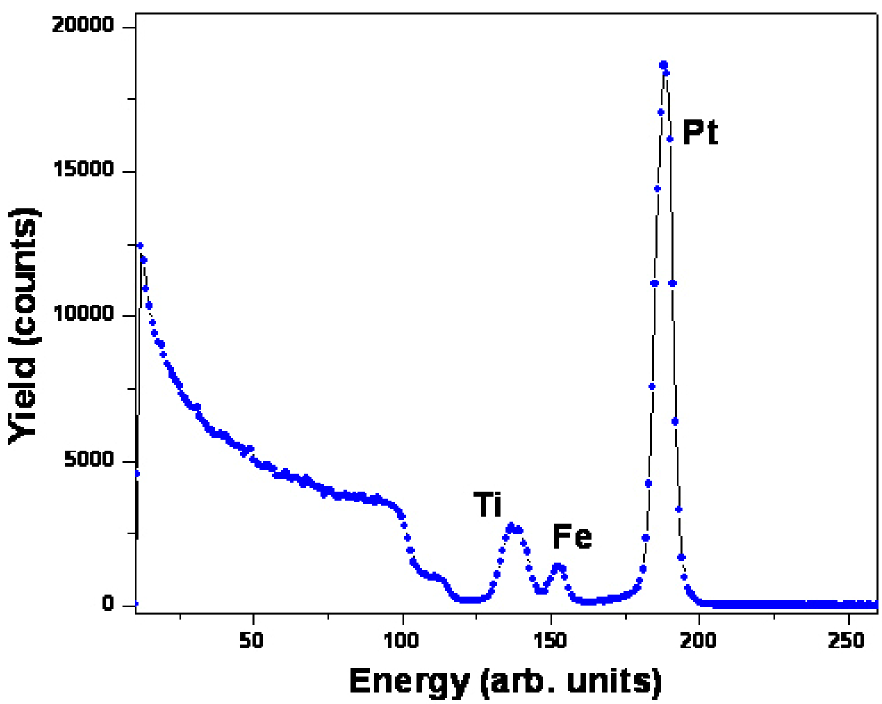

Figure 4-1. RBS spectrum of the FePt system.

4.4 Results and discussion

Experiments involving growth of FePt/TiN/Si(100) films were carried out at different temperatures. It was found that a low deposition temperature of 500° C produced optimal $L1_0$ order and epitaxial growth along [001] direction. Figure 4-2 shows the XRD scan of the sample grown at 500° C. There is only one family of TiN reflections (200) and (400) indicating that it grows epitaxially on Si (100). FePt has two prominent reflections, the (001) superlattice peak and the (002) fundamental peak. No peaks from any other planes of FePt are present. This indicates a strong orientation relationship along the [00l] direction i.e. the direction perpendicular to the plane of the film. The sharp FePt (001) superlattice peak whose intensity exceeds the fundamental FePt (002) peak indicates the presence of strong $L1_0$ order. The fundamental (002) peak also contains in part the slightly displaced (200) reflection indicating tetragonality due to the $L1_0$ structure. The (200) reflection indicates that the film is partially ordered. The extent of ordering can be determined using the order parameter (S), which is calculated as,

$$S^2 = (I_{001}/I_{002})_{exp} / (I_{001}/I_{002})_{cal}, \tag{1}$$

Where I_{001} and I_{002} are the integrated intensity of the (001) superlattice peak and (002) fundamental peak and $(I_{001}/I_{002})_{exp}$ and $(I_{001}/I_{002})_{cal}$ are the experimental and calculated peak intensity ratio, respectively. Following the procedure described by Cebollada et. al. [8], the order parameter was calculated to be S = 0.70. When the composition of the FePt system deviates from the equiatomic composition, the maximum theoretical order parameter can be estimated as $S_{max} = 1-2\Delta x$ [1], where Δx is the deviation from equiatomic composition 0.5. Following this equation S_{max} for the off-stoichiometric $Fe_{41}Pt_{59}$ system was estimated to be 0.82.

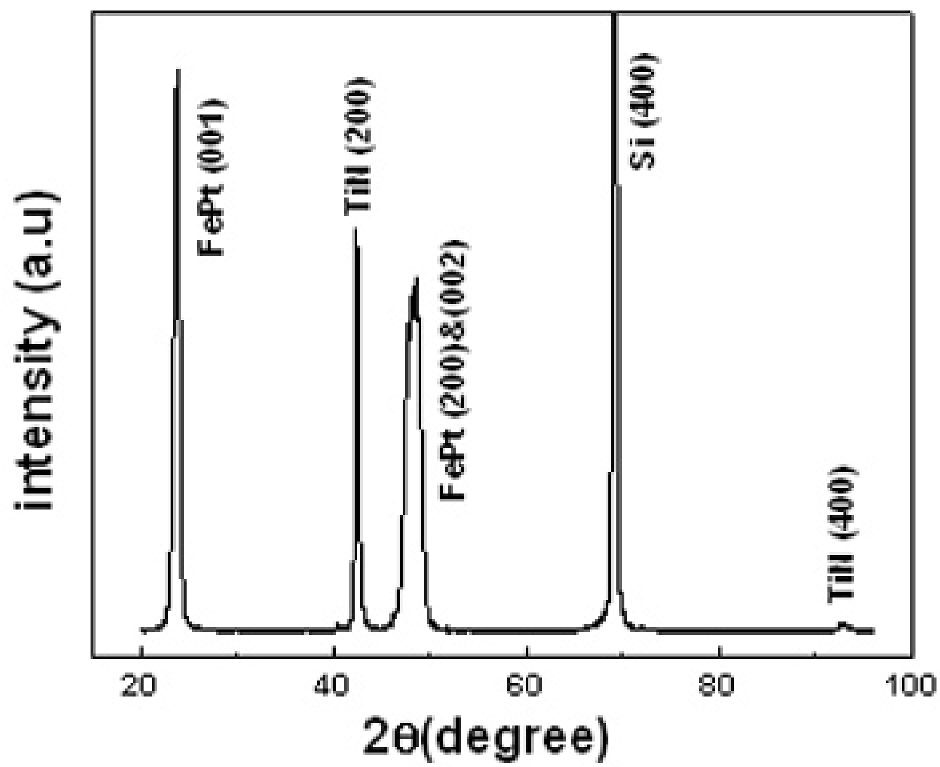

Figure 4-2. X-ray scan of the FePt thin film sample grown at 500 °C.

Epitaxial nature of the FePt film was further confirmed by TEM analysis. Figure 4-3a shows a low magnification crosssection TEM micrograph of the FePt film grown on a TiN template with Si (100) as the substrate. The FePt film is continuous and has a thickness of about 30 nm. The thickness of the TiN template is about 28 nm. The cross sectional selected area diffraction (SAD) pattern of this heterostructure along a <011> zone axis is shown in Fig. 4-3b. In all the directions marked in this SAD pattern the diffraction spots of Si (inner), TiN (middle) and FePt (outer) are aligned. This indicates an epitaxial relationship of the FePt film and the TiN template with the Si (100) substrate. It is essentially a cube on cube epitaxy with all three <100> axes of the film and the template parallel to the substrate. Thus, we obtain an orientation relationship as FePt (001) <001>║ TiN (100) <001>║ Si (100) <001>. Other than the regular FCC fundamental diffraction spots, the SAD also shows additional superlattice spots (labeled in white in Fig. 4-3b) that indicate the presence of $L1_0$ order in FePt. These spots can be seen along the [200] and [02-2] direction and are marked as (100) and (01-1). These results confirm earlier results obtained by XRD that showed ordering of the FePt system under study. Ordering of the FePt unit cell tends to make it slightly tetragonal in nature. The c/a ratio calculated for the $L1_0$ ordered FePt thin film in our study was 0.975, with a = 3.846 Å and c = 3.75 Å.

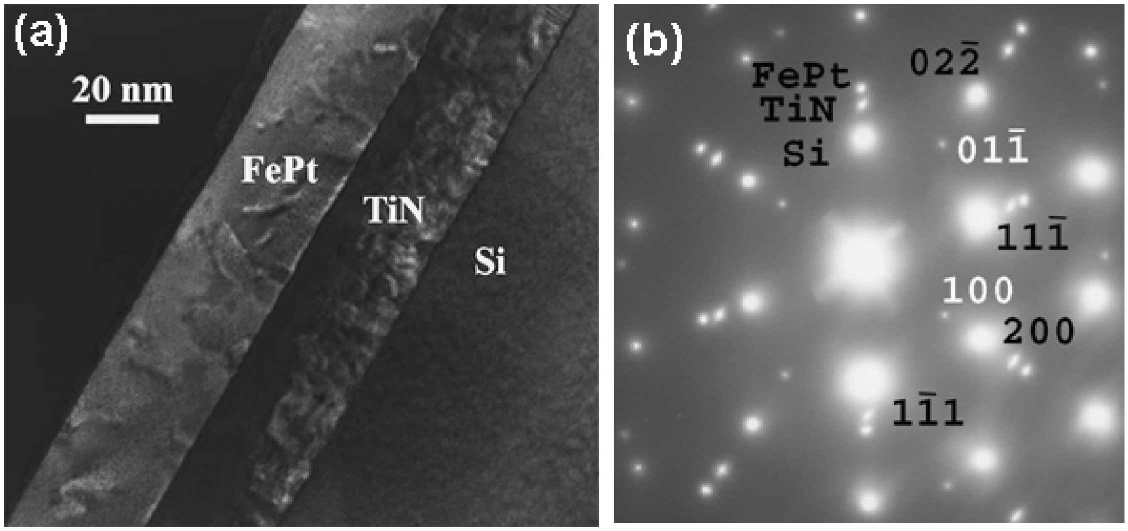

Figure 4-3. (a) Cross section TEM image of the continuous FePt thin film sample (b) The corresponding SAD pattern, in a <110> zone.

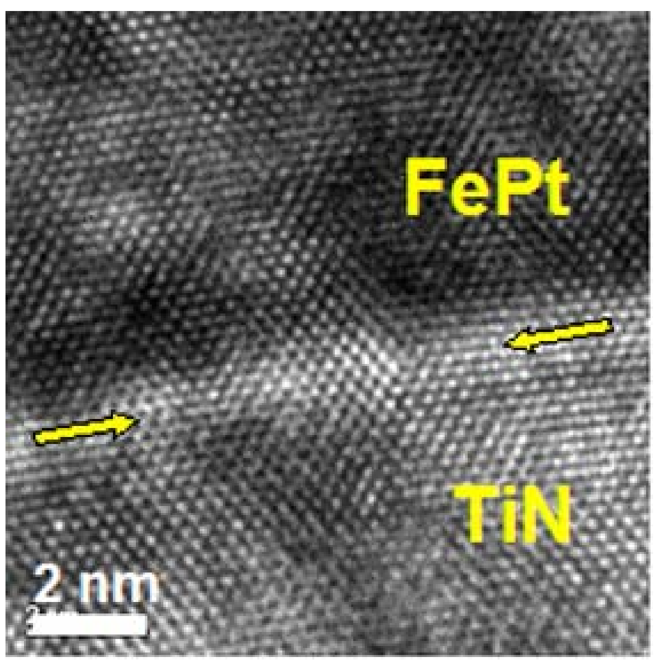

Figure 4-4. HRTEM image of the FePt/TiN interface in a <110> zone.

Figure 4-4 shows a HRTEM image of the FePt and TiN interface. The matching of atomic planes across the interface is clearly seen. The interface is sharp, clear and devoid of any interfacial reaction. The lattice parameter of TiN is calculated to be 4.24 Å and considering the lattice parameter of FePt to be 3.838 Å, the lattice mismatch between TiN and FePt is 9.5 %. Here it is to be noted that TiN (4.24 Å) and MgO (4.21 Å) have similar lattice parameters and hence lattice mismatch with FePt remains almost the same in both cases [9]. This means that TiN can effectively replace MgO, in order to induce $L1_0$ order during growth of FePt films. Thus, we can use a Si (100) substrate with a TiN template layer to successfully grow FePt films and can achieve the same results in terms of the $L1_0$ ordering as can be obtained by using MgO substrate.

The epitaxial growth of FePt on TiN poses a great challenge because of the large misfit involved (misfit strain = 9.5 %). Epitaxy in such large mismatch systems is achieved by domain matching epitaxy (DME), where integral multiples of lattice planes match across the interface [10]. Figure 4-5 is an FFT (fast Fourier transform) image showing planes perpendicular to the FePt/TiN interface. This FFT was obtained from the HRTEM image shown in Fig. 4-4 by masking all but the planes perpendicular to the interface. It is clear from Fig. 4-5 that 10/9 and 11/10 domains alternate to accommodate the 9.5 % misfit in the FePt/TiN system. The frequency with which the 10/9 and 11/10 domains alternate is given by the frequency factor α, which was calculated to be 0.547 [10]. With α = 0.547, the residual misfit is fully accommodated because, 10.547 x (a_{FePt}) = 40.479 matches quite well with 9.547 x (a_{TiN}) = 40.4793. Here, by a 10/9 domain we mean that 10 planes of FePt match with 9 planes of TiN and similarly in the 11/10 domain, 11 planes of FePt match with 10 planes of TiN. The domains themselves are separated by dislocations or half planes (marked in Fig. 4-5). In this context, epitaxy of TiN on Si is even more challenging because the misfit here is even larger, 22%. Epitaxy of TiN on Si is achieved by alternating 3/4 and 4/5 domains with equal frequency [10].

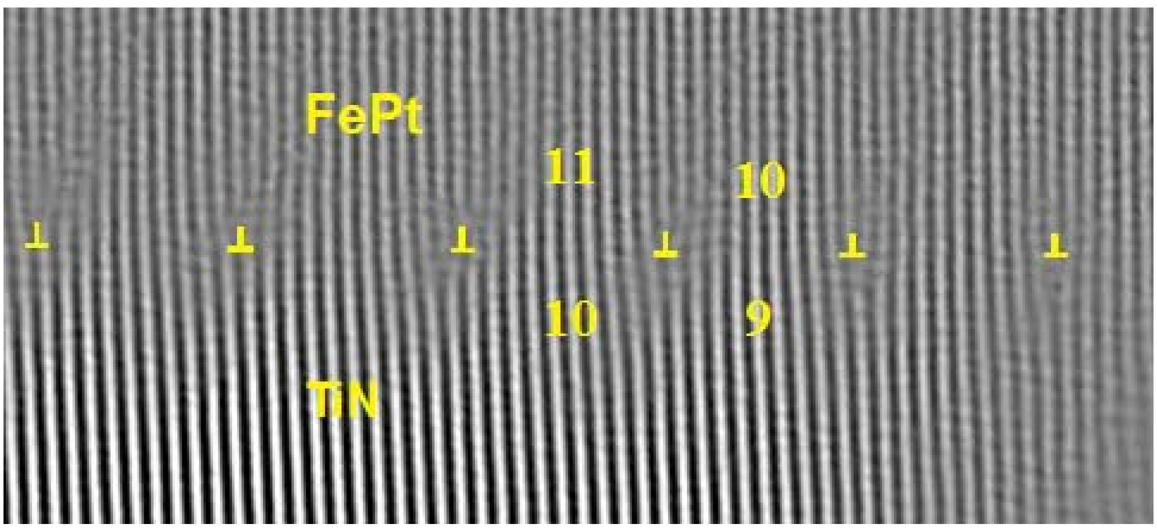

Figure 4-5. FFT image showing domain matching at the FePt/TiN interface.

Figure 4-6a shows the magnetization versus field curves at 300 K for the FePt thin film sample grown at 500° C. The perpendicular loop showed improved coercivity, remanence and squareness when compared to the parallel loop, indicative of the easy axis of magnetization being oriented perpendicular to the sample surface.

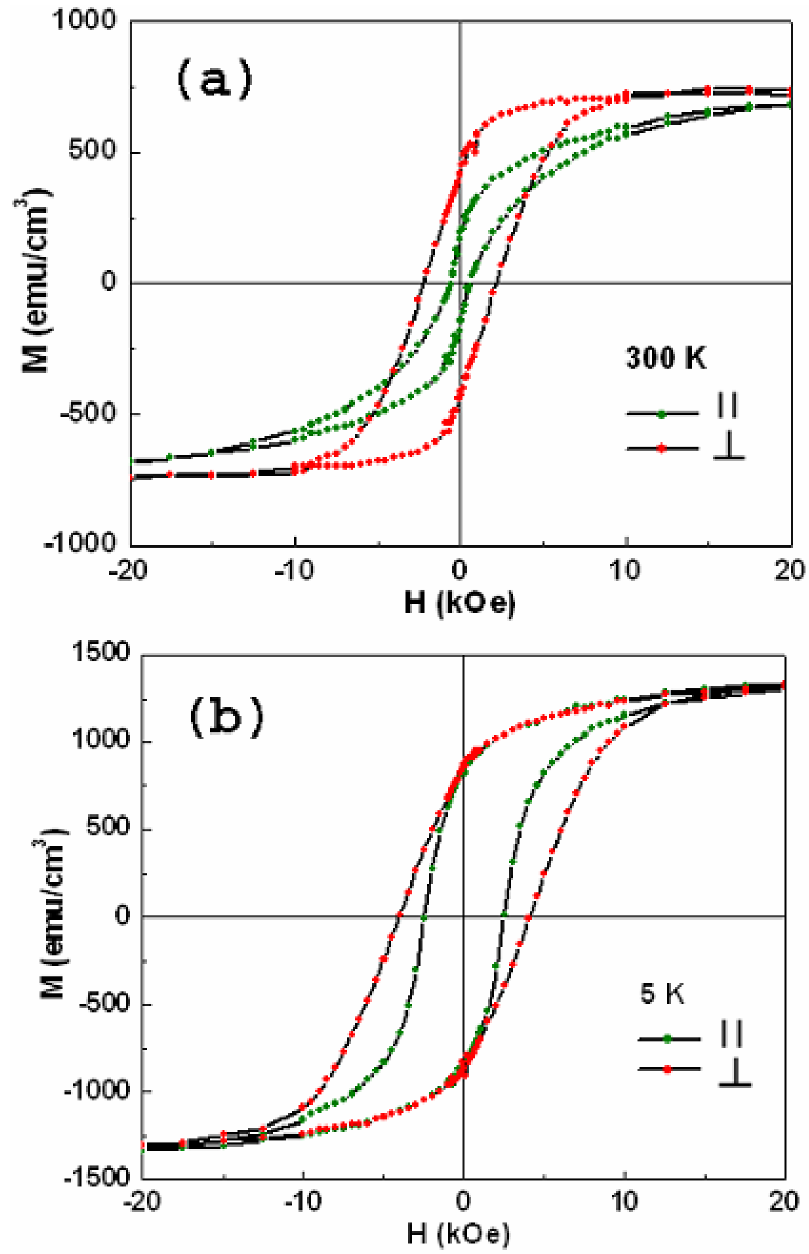

Figure 4-6. (a) Room temperature magnetic hysteresis loops of the FePt thin film sample grown at 500 °C in the perpendicular and in-plane directions. (b) MH loops at 5K.

In the direction perpendicular to the film plane, which is the easy axis of magnetization, the sample shows high coercivity ($H_c^{\perp}$ = 2250 Oe). The saturation magnetization was 740 emu/cm^3 and squareness was, M_r/M_s = 0.7. Some hysteresis behavior is also seen in the direction parallel to the film ($H_c^{\parallel}$ = 600 Oe). It is also evident from Fig. 4-6 that the perpendicular loop saturates at much smaller fields, whereas the parallel loop closes only at high fields. In-plane remanent magnetization can be attributed to the small fraction of FePt that remains in the disordered phase and some residual misoriented fraction of FePt that has its c-axis along the film plane. In addition to the room temperature measurements, magnetic properties of the FePt thin film were also evaluated at lower temperatures. Figure 4-6b shows hysteresis loops obtained in both the perpendicular and in-plane directions at 5 K. Here, the difference between the perpendicular and in-plane loops is not pronounced like the case of the room temperature data. This may be attributed to higher stresses in the film at low temperatures. The anisotropy due to stress can then negate some of the crystalline anisotropy [11]. The coercivity at 5 K in the perpendicular direction is 4060 Oe and in the in-plane direction it is about 2520 Oe.

When the growth temperature was increased to 600 °C, we observed marked improvement in anisotropic ordering and related magnetic properties. Figure 4-7 shows the XRD scan of the FePt thin film grown at 600 °C. The order parameter (S) calculated from equation (1) improved to 0.77. Magnetic hysteresis curves at room temperature for the sample grown at 600 °C are shown in Fig. 4-8. When compared to the sample grown at 500 °C, the squareness of the perpendicular loop increased remarkably. The squareness

(M_r/M_s) value was as high as 0.95, with remanence M_r = 740 emu/cm^3 and saturation magnetization M_s = 780 emu/cm^3. The coercivity in the perpendicular direction increased to $H_c^{\perp}$ = 2450 Oe. When compared to the perpendicular loop the in-plane magnetization was minimal, indicating large magnetic anisotropy. The perpendicular hysteresis loop for this system, ideal for magnetic storage, showed two opposite states of magnetization that switch at well-defined fields. The values of coercivity obtained in this study are appreciable keeping in mind the off-stoichiometric nature of the composition ($Fe_{41}Pt_{59}$). Similar values for coercivity have been reported in the literature for sputtered epitaxial FePt/MgO thin films synthesized at similar growth temperatures [1,2].

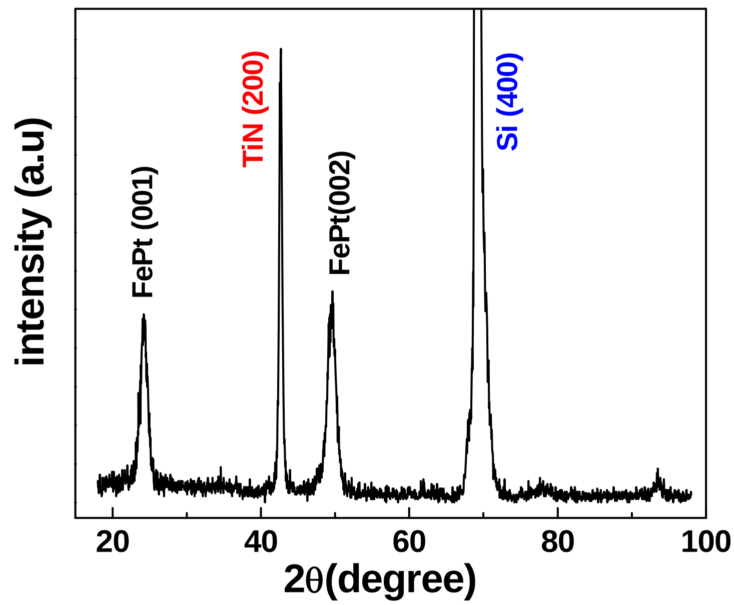

Figure 4-7. XRD scan of the FePt film grown at 600 °C.

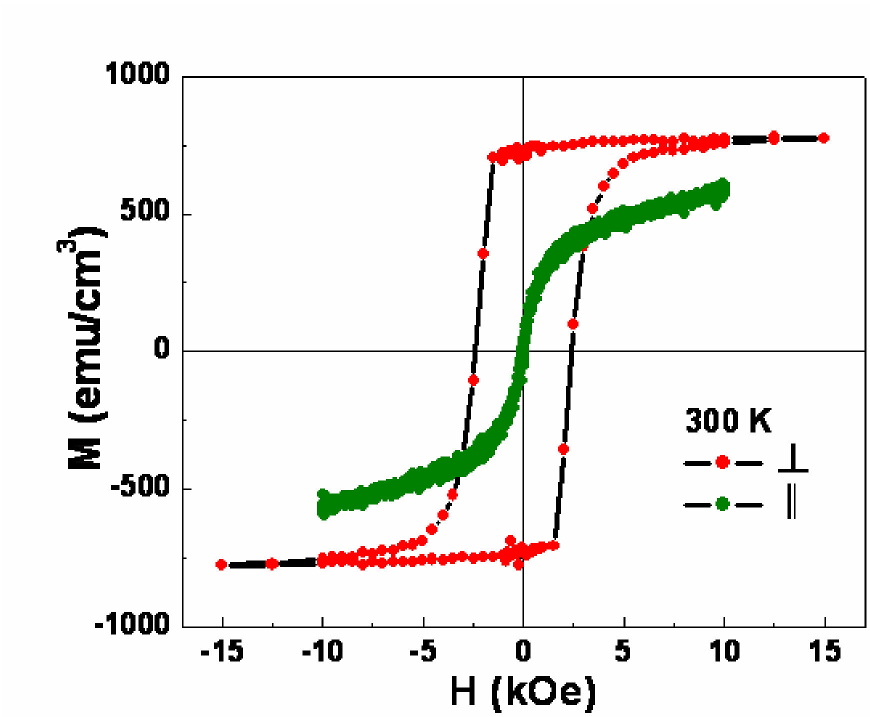

Figure 4-8. Room temperature magnetic hysteresis loops of the FePt thin film sample grown at 600 °C in the perpendicular and in-plane directions.

4.5 Conclusions

In summary, we have shown that $L1_0$ ordered epitaxial FePt (001) films can be grown at a moderate temperature of 500° C using pulsed laser deposition. The films were essentially grown on a Si (100) substrate with epitaxial TiN template layer. Growth on Si (100) can potentially prove to be useful in making devices that are compatible with the microelectronic devices. Favorable results in terms of the order parameter (S = 0.70) showed that TiN can be effectively used as a template to induce $L1_0$ order. The epitaxial relationship and presence of $L1_0$ order were studied by XRD and further confirmed by TEM. The following epitaxial relationship was obtained in the FePt structures: FePt (001) <001>‖ TiN (100) <001> ‖ Si (100) <001>. The 9.5 % misfit strain between FePt and TiN was relaxed by domain matching epitaxy where 10/9 and 11/10 domains alternate across the interface. Hysteresis loops along the direction perpendicular to the plane of the film showed high coercivity, remanence and squareness when compared to the loops that are parallel to the film plane. At 500 °C the perpendicular coercivity was 2250 Oe and the squareness was 0.7. A remarkable squareness of 0.95 was achieved when growth temperature was increased to 600 °C. Such magnetic properties are significant keeping in mind the off-stoichiometric nature of the film ($Fe_{41}Pt_{59}$).

References

1. K. Barmak, J. Kim, L.H. Lewis, K.R. Coffey, M.F. Toney, A.J. Kellock, and J. U. Thiele, J. Appl. Phys. **98**, 033904 (2005).
2. F. Casoli, F. Albertini, L. Pareti, S. Fabbrici, L. Nasi, C. Bocchi, and R. Ciprian, IEEE Trans. Magn. **41**, 3223 (2005).
3. Y.K. Takahashi, K. Hono, T. Shima, and K. Takanashi, J. Magn. Magn. Mater. **267**, 248 (2003).
4. D. Weller, A. Moser, L. Folks, M. E. Best, W. Lee, M. F. Toney, M. Schwickert, J. U. Thiele, and M. F. Doerner, IEEE Trans. Magn. **36**, 10 (2000).
5. T. Shima, T. Moriguchi, S. Mitani, and K. Takanashi, Appl. Phys. Lett. **80**, 288 (2002).
6. A. Gupta, H. Wang, A. Kvit, G. Duscher, and J. Narayan, J. Appl. Phys. **93**, 5210 (2003).
7. Y.K. Takahashi and K. Hono, Scripta Mater. **53**, 403 (2005).
8. A. Cebollada, D. Weller, J. Sticht, G.R. Harp, R.F.C. Farrow, R. F. Marks, R. Savoy, J. C. Scott, Phys. Rev. B. **50**, 3419 (1994).
9. An-Cheng Sun, P.C. Kuo, Jen-Hwa Hsu, H.L. Huang, and Jui-Ming Sun, J. Appl. Phys. **98**, 076109 (2005).
10. J. Narayan, and B.C. Larson, J. Appl. Phys. **93**, 278 (2003).
11. B. D. Cullity, Introduction to Magnetic Materials, Addison-Wesley, Readings, MA (1972).

Chapter 5

5 Growth, characterization and magnetic properties of epitaxial FePt nanodots on Si (100)

5.1 Abstract

In this chapter, we report on the pulsed-laser deposition of epitaxial FePt nanodots onto Si (100) substrates using TiN as a template buffer. X-ray diffraction studies show that the FePt nanodots are primarily oriented along the [001] direction and show $L1_0$ ordering with order parameter (S) equal to 0.75. The composition of the nanodots was $Fe_{41}Pt_{59}$. Cross sectional transmission electron microscopy revealed the following epitaxial relationship; FePt (001) <001>‖TiN (100) <001>‖Si (100) <001>. Plan view transmission electron microscopy analysis showed that the FePt nanodots are well separated and have an average size of 18 nm. Selected area electron diffraction patterns along the <110> and <001> zone axes were analyzed to study the $L1_0$ order in the FePt nanodots. Room-temperature magnetic-hysteresis measurements showed that the islands are predominantly magnetized in the perpendicular direction with higher coercivity ($H_c^{\perp}$ = 3200 Oe) as compared to the parallel direction ($Hc^{\parallel}$ = 1000 Oe). In this system, each nanodot acts as a single domain and assuming one bit of information is stored in each

nanodot, magnetic storage density can exceed one Terabits per square inch, corresponding to 250 million pages of information per chip.

5.2 Introduction

In recent years considerable attention has been focused on the synthesis and study of magnetic nanoparticles for high-density magnetic recording [1-7]. For this purpose, we require magnetic particles in the nano-regime with uniform size, composition and crystallographic orientation. Tailoring the dimensions of the magnetic particles to sizes comparable with characteristic magnetic length scales, like magnetic exchange length and domain width, can give rise to interesting properties [5-8]. Inherent properties of a magnetic system like saturation magnetization, Curie temperature and anisotropy are affected by reduction in size [5]. For the purpose of high density magnetic storage, the most relevant property that is associated with size reduction is the transition to single domain state and accompanying large increase in coercivity [6-8]. Also, well-separated magnetic nanoparticles have minimal magnetic coupling, leading to a better signal to noise ratio that is essential for magnetic recording applications.

The $L1_0$ ordered FePt material system is a promising candidate for magnetic recording applications owing to its excellent properties including, high uniaxial magnetocrystalline anisotropy, high coercivity, high saturation magnetization and good chemical stability [9]. The high magnetocrystalline anisotropy permits the use of smaller particles before the onset of superparamagnetism, which may translate into potentially larger recording densities. Hence the primary motivation to synthesize and study perpendicularly oriented FePt nanoparticles dispersed in a non-magnetic matrix is to combine favorable properties, which accompany size reduction, with superior magnetic properties of FePt and arrive at a system that is highly suitable for high-density perpendicular magnetic recording.

Different techniques like sputtering [4], MBE [10], ion-beam synthesis [2], electron-beam evaporation [11] and chemical synthesis [1] have been employed to synthesize FePt nanoparticles. Synthesis using chemical approaches requires an additional annealing step to impart texture and desired order in the nanoparticles. However, the annealing processes can be detrimental, as it can cause interfacial diffusion, destroy self-assembly and induce unwanted nanoparticle coarsening and agglomeration [12]. It is important to realize that physical vapor deposition methods based on substrate controlled epitaxy are more suitable for synthesizing crystallographically oriented FePt nanostructures.

We report here the synthesis of self-assembled epitaxial FePt nanoparticles by pulsed laser deposition (PLD) where desirable magnetic properties can be achieved without further annealing. PLD is a high energy non-equilibrium processing technique, where the energy of the ablated species can be as high as 10-100 eV [13]. This feature affords several advantages, including the ability to form novel phases, and to reduce processing temperatures. In particular, it is important to reduce ordering temperature (thermal budget) from an application point of view. It has been reported previously that off-stoichiometric FePt systems that are rich in Pt content tend to order at lower temperatures [14] and exhibit higher values of anisotropy [15]. Hence, the Pt-rich off-stoichiometric system $Fe_{41}Pt_{59}$ was chosen for this study. Accordingly, we will show that we can induce considerable $L1_0$ order at a low processing temperature of 500 ° C in the $Fe_{41}Pt_{59}$ system.

5.3 Experiment

The FePt nanodots were grown on an epitaxial TiN template with Si (100) as the substrate. Use of Si (100) substrate is significant as well as challenging because it permits integration with modern microelectronic devices. The TiN template is used to control the epitaxy and induce $L1_0$ ordering in the FePt nanodots. TiN is a nonmagnetic metal with resistivity close to 15 $\mu\Omega$ cm in single crystal form, and it also acts as an excellent diffusion barrier [16]. The FePt/TiN/Si heterostructure was synthesized by pulsed-laser deposition using KrF excimer laser with wavelength = 248 nm and pulse duration = 25 ns. A rotating multi-target assembly was used to grow the TiN template and FePt films. Substrate preparation of Si (100) involved the following steps; ultrasonic rinsing, cleaning with acetone, methanol rinse and then etching with Hf (49%) in order to dissolve the native oxide layer and obtain hydrogen-terminated Si (100). For the growth of a TiN template the following deposition parameters were used: base pressure 10^{-7} torr, temperature 600-620 °C and energy density ~2 J/cm^2. Growth parameters used for the FePt nanodots were as follows; base pressure 10^{-7} torr, temperature 500 °C and energy density ~5 J/cm^2. Ablation and deposition rates of Fe and Pt were studied individually.

For the growth of FePt, the target assembly included a segmented geometry of two individual pieces of Fe and Pt, appropriately crossed for a desired composition. The composition analysis was done by using Rutherford backscattering (RBS). The composition was found to be $Fe_{41}Pt_{59}$ (see chapter 4).

X-ray diffraction (XRD) was used to determine the growth orientation and texture of the samples. A Rigaku Geigerflex Diffractometer with Cu K_{α} radiation ($\lambda = 1.54$ Å) and a graphite monochromator was used for the XRD experiments. For in-depth crystallographic analysis, transmission electron microscopy (TEM) was performed using a JEOL 2010F TEM operating at 200 KV with a resolution of 0.18 nm, which was equipped with Gatan Image Filter (GIF) system. To determine the morphology and size of the FePt islands, both cross section and plan view TEM samples were studied. TEM samples were prepared by mechanical polishing, followed by dimpling and Ar-ion milling until electron transparency was attained. Magnetic property measurements were performed using a superconducting quantum interference device (SQUID).

5.4 Results and discussion

Figure 5-1 is an XRD pattern of the FePt nanodot sample showing a strong [001] orientation i.e. the c-axis is perpendicular to the sample surface. In this XRD pattern we see the FePt (002) fundamental peak, the FePt (001) superlattice peak, the TiN (200) and (400) template peaks and the Si (400) substrate peak. The occurrence of the FePt (001) superlattice peak indicates the presence of $L1_0$ ordering. The ordering can be quantified by the order parameter (S), which is defined as,

$$S^2 = (I_{001}/I_{002})_{exp} / (I_{001}/I_{002})_{cal}, \tag{1}$$

where I_{001} and I_{002} are the integrated intensity of the (001) superlattice peak and (002) fundamental peak and $(I_{001}/I_{002})_{exp}$ and $(I_{001}/I_{002})_{cal}$ are the experimental and calculated peak intensity ratio, respectively. Following the procedure described by Cebollada et. al. [17], the order parameter was then calculated to be, S = 0.75. Here it is important to note that the maximum order that can be achieved in the off-stoichiometric $Fe_{41}Pt_{59}$ system is S_{max} = 0.82 [18]. The XRD pattern in Fig. 5-1 also shows some minor structural imperfections like the FePt (200) peak. This indicates that a small fraction of the islands may either be disordered or may be misaligned such that their c-axis is parallel to the sample surface.

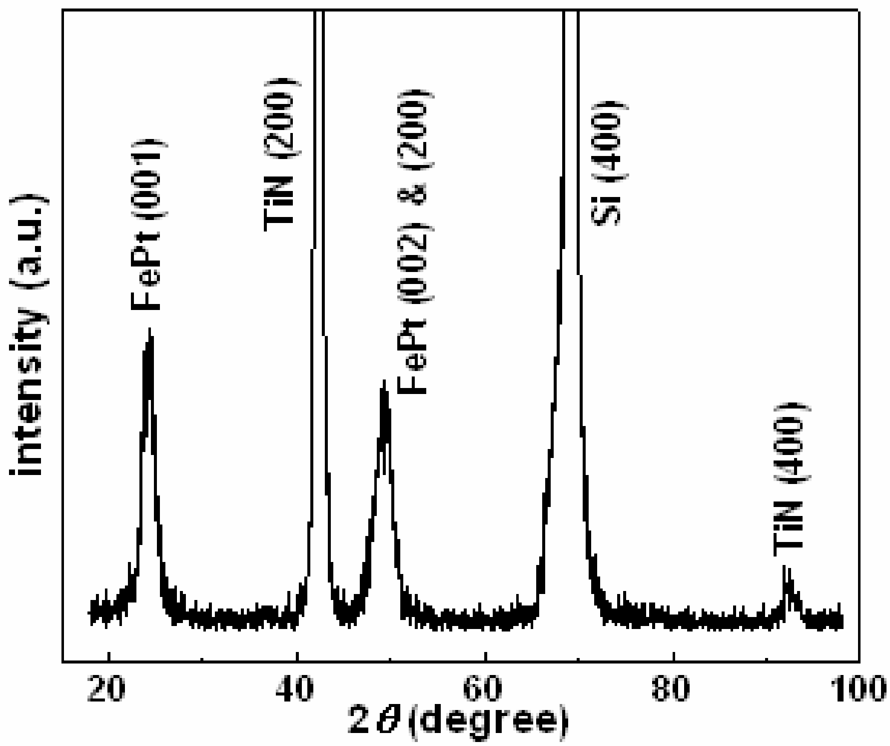

Figure 5-1. XRD pattern of the FePt nanodot sample grown on a Si (100) substrate using TiN as a template buffer.

Figure 5-2a shows a cross section TEM micrograph of the FePt islands, including the TiN template and the Si substrate. The FePt islands seem to have a trapezoidal shape with flat facets, similar to the observations by Kim et. al. [4]. The islands seem to be well separated and have an average thickness of about 5 nm. The SAD (selected area diffraction) pattern in a <110> zone axis from a region comprising the FePt island, the TiN template and the Si substrate is shown in Fig. 5-2b. In all the directions marked in this SAD pattern the diffraction spots of Si (inner), TiN (middle) and FePt (outer) are aligned. This indicates an epitaxial relationship of the FePt island and the TiN template with the Si (100) substrate. It is essentially a cube on cube epitaxy with all three <100> axes of the FePt island and the TiN template aligned with the Si substrate. From this we obtain an orientation relationship as follows; FePt (001) <001>║ TiN (100) <001>║ Si (100) <001>. The fundamental diffraction spots of FePt are labeled in black and the additional superlattice spots that arise due to $L1_0$ ordering are labeled in white. These spots can be seen along the [200] and [02-2] direction and are marked as (100) and (01-1). Ordering tends to make of the FePt unit cell slightly tetragonal in nature. The c/a ratio estimated for the $L1_0$ ordered FePt nanodot in our study was 0.968, with a = 3.85 Å and c = 3.73 Å. The lattice mismatch between TiN and FePt is 9.5 %. And between the TiN template and Si (100) substrate the misfit is 22 %. Epitaxy in such large misfit systems was achieved by domain matching epitaxy (see chapter 2 and chapter 4 for details).

Figure 5-2c is a cross section HRTEM (high resolution transmission electron microscopy) image showing a single FePt island and the TiN template. The interface between FePt and TiN is clear, sharp and devoid of any interfacial reaction. The two cross-sectional images (Fig. 5-2a and Fig. 5-2c) show that the FePt islands have well-defined edges with no indication of a wetting layer. Thus, formation of FePt islands on TiN follows a 3D Volmer-Webber mode of growth. It is important to note that short deposition times (about one minute) were employed to form these nanodots. This was done to inhibit the growth to the early stage, before the individual islands started to merge and form a continuous film. The values of surface energy also suggest a 3D-type of growth mode. Surface energy for relaxed geometries of (100) TiN (σ_{TiN}) is reported to be 1.28 J/m^2 [19] and for (001) FePt (σ_{FePt}) it is about 2.18 J/m^2 [20]. From these values it is clear that,

$$\sigma_{FePt} + \sigma_{interface} > \sigma_{TiN} \tag{2}$$

This condition suggests a Volmer-Weber type of growth mode.

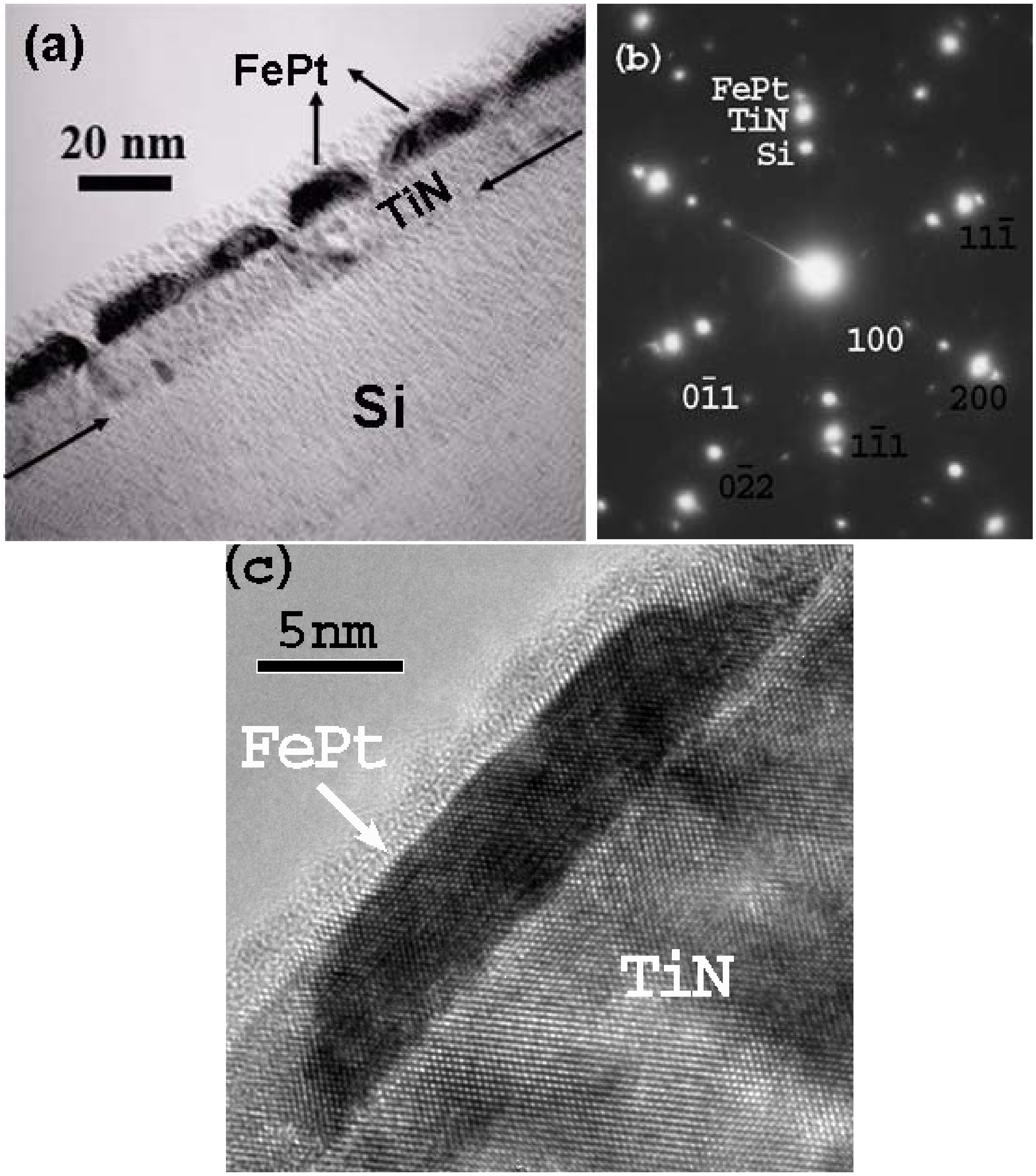

Figure 5-2. (a) Cross section TEM image showing the FePt nanodots, the TiN template and the Si substrate. (b) The corresponding SAD pattern in a <110> zone. (c) HRTEM image showing a single FePt nanodot and the TiN template.

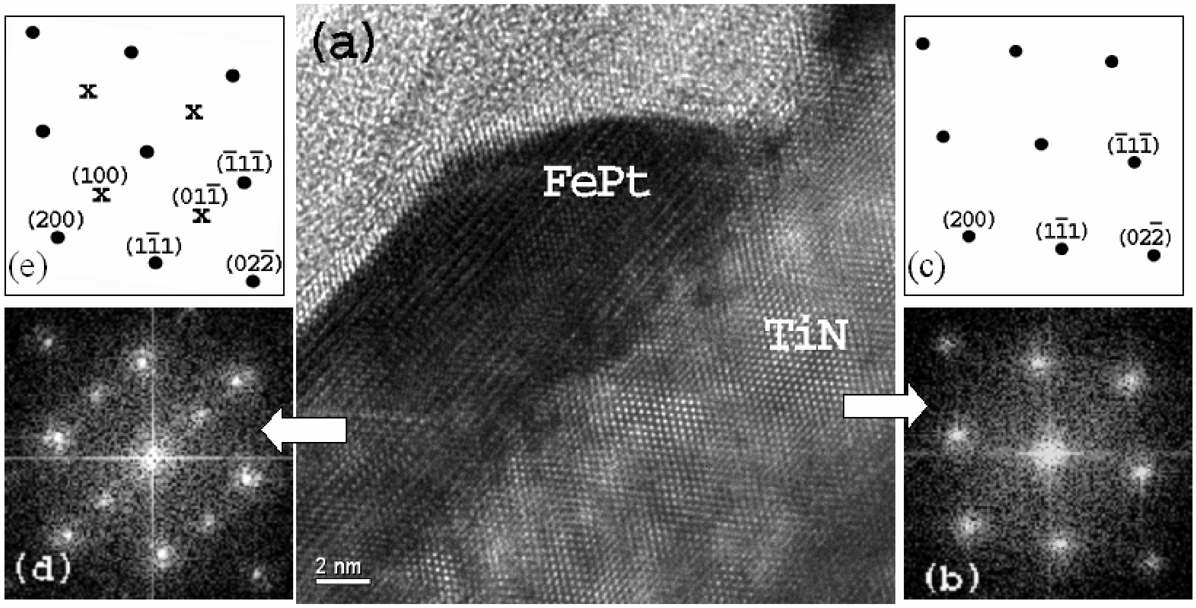

Figure 5-3. (a) HRTEM image showing part of the FePt nanodot and the TiN buffer layer (b) FFT from a region comprising TiN only (c) Corresponding indexed schematic of the TiN FFT. (d) FFT from a region comprising FePt only (e) Corresponding indexed schematic of the FePt FFT.

Figure 5-3a is a cross sectional HRTEM image showing part of the FePt nanodot and the TiN template. Figure 5-3b is a FFT (fast Fourier transform) image, from a region comprising TiN only, showing a regular FCC diffraction pattern in a <110> zone. This pattern has been indexed in a corresponding schematic in Fig. 5-3c. Figure 5-3d is a FFT image from a region including just the FePt nanodot. The corresponding indexed schematic is shown in Fig. 5-3e. It is clear that, in addition to the regular FCC spots found in Fig. 5-3b, Fig. 5-3d shows additional superlattice spots at (100) and (01-1) along the [200] and [02-2] directions. These $L1_0$ superlattice spots are marked as an "x" in Fig. 5-3e. The above analysis clearly establishes the fact that the FePt islands under study are $L1_0$ ordered.

Figure 5-4a is a plan view TEM image showing distinct, well separated FePt islands in the TiN matrix. The corresponding SAD pattern in the <001> zone is shown in Fig. 5-4b. We observe in this SAD pattern distinct double diffraction spots, i.e. each major diffraction spot is surrounded by other less intense symmetric spots. In this case, the double diffraction spots arise due to the overlap of the FePt and TiN planes during diffraction. The brighter spots belong to TiN, which has the larger lattice parameter (4.24 Å). Among the smaller spots surrounding the brighter TiN spot, some belong to FePt and the others correspond to the double diffraction occurring between TiN and FePt. It is important to note that there is no contribution from Si in this SAD pattern. This is attributed to the sample preparation process wherein we thin the sample from the substrate side and hence most of the Si is lost during thinning. Figure 5-4c is a corresponding representative schematic diffraction pattern (without double diffraction) for a <001> zone axis with all the diffraction spots indexed. Other than the regular FCC diffraction spots the SAD shows forbidden reflections or extra superlattice spots that arise due to the $L1_0$ order in the system. The regular FCC diffraction spots (marked as dark circles) that arise in the [001] zone axis are (020), (040), (200), (220), (240), (400), (420), (440). The additional/forbidden superlattice spots (marked as x) that appear due to $L1_0$ order are (110), (130), (330), (310), (330).

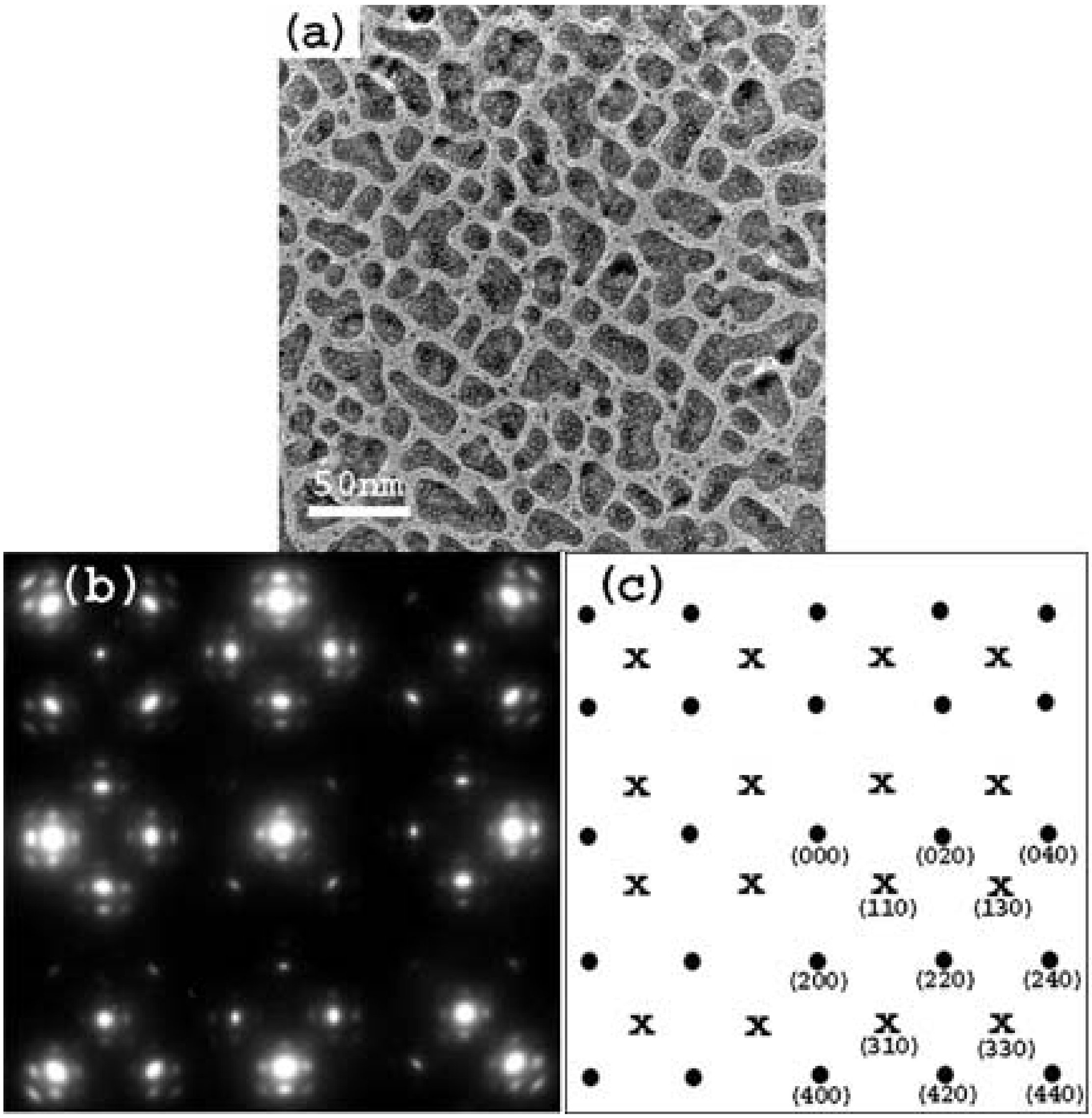

Figure 5-4. (a) Plan view TEM image of the FePt nanodots in a TiN matrix. (b) Corresponding diffraction pattern in a <001> zone. (c) Representative indexed diffraction pattern.

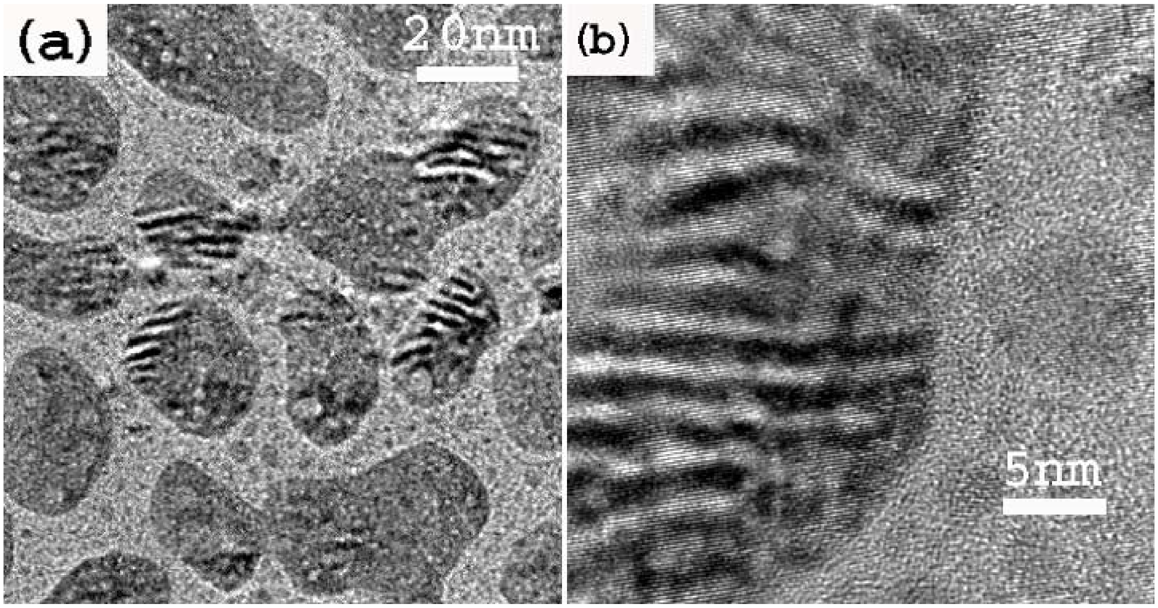

Figure 5-5. (a) HRTEM image showing FePt nanodots with Moiré fringes. (b) HRTEM image showing Moiré fringes within a single FePt nanodot.

Figure 5-5a is a high magnification plan view TEM image of the FePt islands. We observe Moiré fringes in few of the islands in this figure. Figure 5-5b is a HRTEM image showing Moiré fringes in the same region within a single FePt island. The Moires fringe arise due to the interference that occurs when the lattice planes of FePt and TiN overlap. The condition for the formation of a Moiré pattern is that a beam which has been diffracted once by each set of lattice planes is allowed to contribute to the TEM image formation. The formation of Moiré fringes in certain regions indicate that the islands are not fully relaxed. It is important to note that the majority of the islands (as seen in Fig. 5-4a and Fig. 5-5a) are devoid of Moiré fringes. This suggests that most islands are fully relaxed. The 9.5 % misfit strain between FePt and TiN is relaxed via domain matching epitaxy, by matching 10/9 planes of FePt and TiN across the interface. Figure 5-6 is a histogram showing the size distribution of the FePt islands. The total number of islands included in this plot is equal to 303. The average island size was calculated to be ~18 nm.

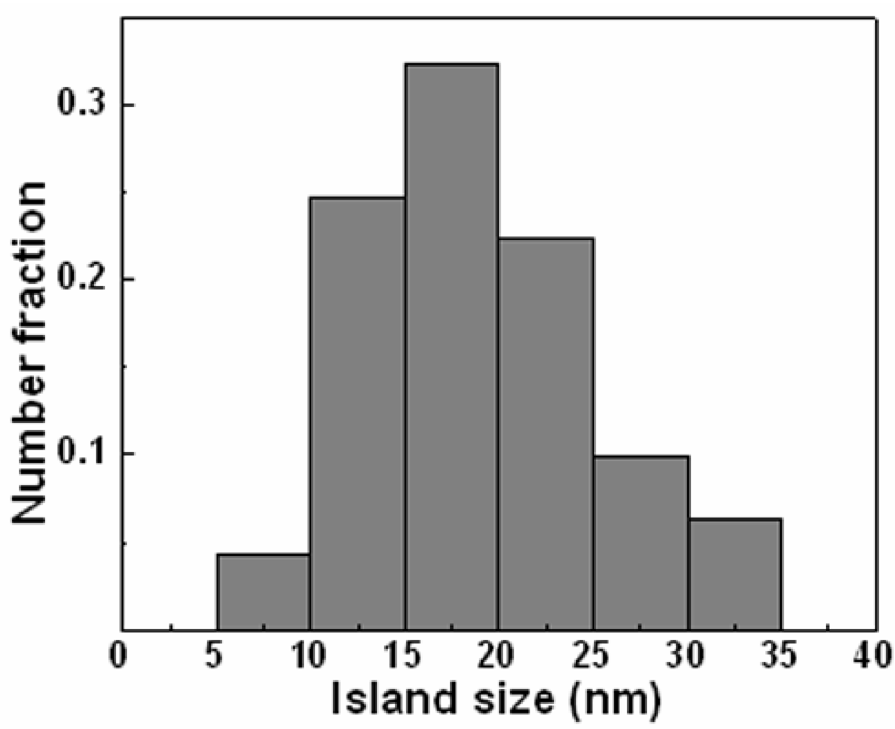

Figure 5-6. Histogram showing size distribution of the FePt nanodots.

From the above results it can be inferred that TiN can be used as a suitable matrix to grow self assembled FePt nanodots, whose size and crystal orientation can be controlled according to our requirement. The cross section and plan view TEM images and subsequent analysis confirm that the islands are $L1_0$ ordered, well separated and oriented such that the c-axis is perpendicular to the sample surface. Inter-particle separation is necessary to improve signal to noise ratio in the magnetic recording devices.

Perpendicular orientation is necessary to exploit the high degree of magnetic anisotropy present in the $L1_0$ ordered FePt system.

Magnetic properties were evaluated both in the direction perpendicular and parallel to the sample surface. It is important to note that the c-axis is the easy axis of magnetization for the $L1_0$ ordered FePt system. Figure 5-7a shows magnetization versus field curves at 300 K. The perpendicular loop shows higher squareness, remanence and coercivity when compared to the parallel loop. In the perpendicular direction the coercivity is $H_c^{\perp} = 3200$ Oe and the squareness is $M_r/M_s = 0.87$. Such values of coercivity and squareness are significant keeping in mind the off-stoichiometric composition ($Fe_{41}Pt_{59}$) and the low growth temperature involved (500 °C). In contrast, the parallel loop shows much smaller hysteresis ($H_c^{\parallel} = 1000$ Oe) and shows a propensity to saturate at much higher fields. The in-plane magnetization has a contribution from structural imperfections like the small amount of FePt (200) that has in-plane aligned c-axis. In-plane magnetization can also be attributed to the small fraction of FePt islands that may exist in a disordered phase. This is consistent with the XRD observations that show partial ordering (S = 0.75). There is a possibility to improve perpendicular coercivity by employing higher growth temperatures so that structural imperfections like FePt (200) can be completely removed (see chapter 4). Also it has been reported that higher growth temperature (700 °C) promotes 3D or island growth [21]. On the other hand it is also important to note that the magnetic recording industry prefers lower processing temperatures [22]. Therefore, in this work we have tried to optimize the competing parameters of coercivity and process temperature.

The perpendicular coercivity ($H_c^{\perp}$ = 3200 Oe) and processing temperature (500 °C) optimized in this work are appropriate for magnetic recording applications.

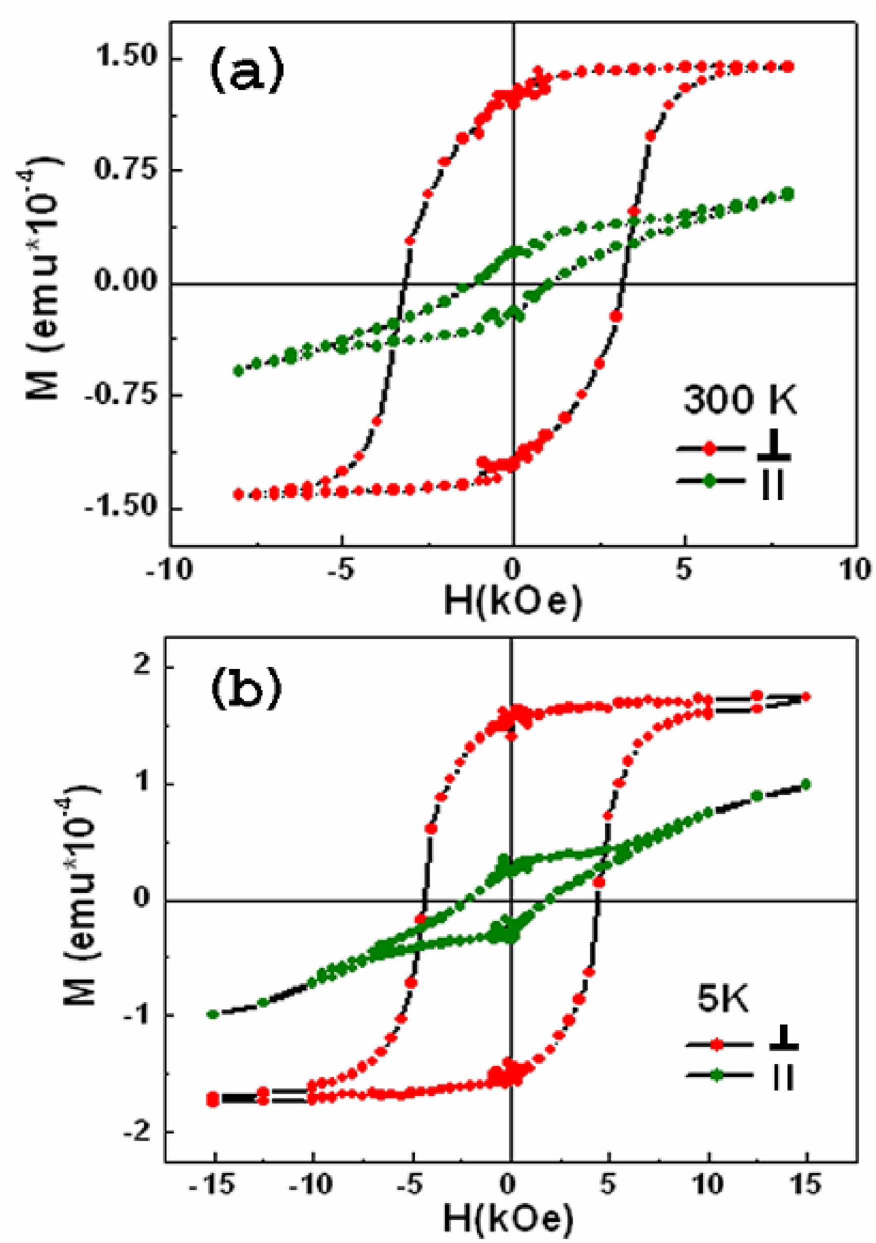

Figure 5-7. (a) Magnetic hysteresis loops of the FePt nanodot sample in the perpendicular and in-plane directions at 300 K. (b) Hysteresis loops at 5K.

In addition to the room-temperature data, magnetic measurements were also carried out at lower temperatures. When compared to the room temperature coercivities, the 5 K measurements (see Fig. 5-7b) showed higher coercivities both in the perpendicular and in-plane directions. The perpendicular coercivity at 5 K is 4420 Oe and the in-plane coercivity at the same temperature is 1980 Oe. In terms of magnetic anisotropy the 5 K results are consistent with the 300 K measurements. The perpendicular loop has higher coercivity, is square shaped and saturates at lower fields, where as the in-plane loop has lower coercivity and seems to saturate at much higher fields.

Further, we present some preliminary results of a multi-layered FePt nanodot structure, which is self-organized in three dimensions. Figure 5-8a is a cross section TEM image showing the tri-layered FePt structure grown at 500 °C. Two images from different regions of the TEM sample have been put together. Here, we have three layers of FePt islands stacked one on top of another with TiN buffer layers in between. The first layer of islands formed is clear and distinct. The quality of the second layer is inferior when compared to the first; most of the third layer is lost during the process of TEM sample preparation.

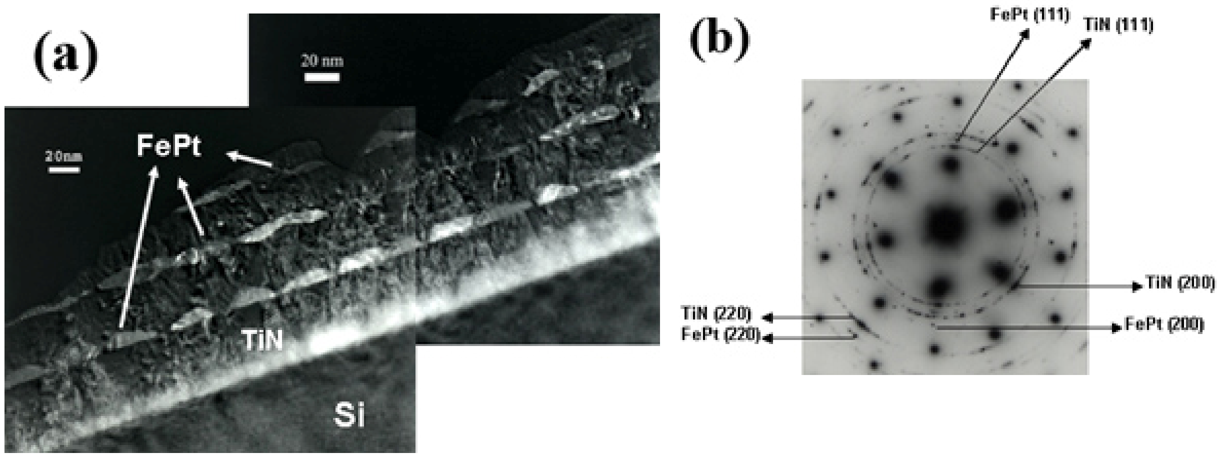

Figure 5-8. (a) Cross section TEM images of the tri-layered nanodot system captured from different parts of the TEM sample (b) The corresponding SAD pattern in a <011> zone (see text for description).

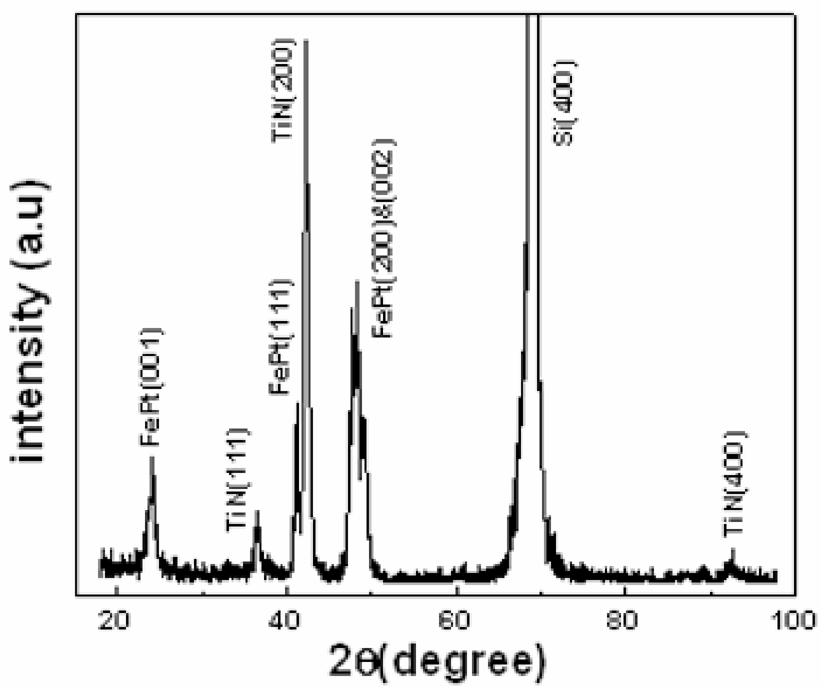

Figure 5-9. X-ray scan of the FePt tri-layered nanodot sample grown at 500 °C.

The X-ray results, shown in Fig. 5-9, contain reflections from FePt (001) and FePt (002). Occurrence of the superlattice (001) peak indicates the presence of ordering. Also seen are some structural imperfections such as the FePt (200) and FePt (111) peaks. The TiN buffer layer is mostly epitaxial with a strong (200) reflection, but there is also a hint of the TiN (111) reflection. Figure 5-8b shows a SAD pattern in a <110> zone. Faint discontinuous rings of FePt (111), (200) and (220) are observed. The discontinuous rings are typical of nanodots with a mixed orientation. The more prominent rings belong to TiN (111), (200) and (220). The single crystal spots belong to the Si substrate. We believe that the first layer of FePt nanodots grow epitaxially along [001]. The second and third layers progressively deteriorate in terms of their [001] epitaxy and start showing <111> orientations. This is because the first layer of islands have a perfectly epitaxial TiN [200] template to grown on. For the second and third layer of FePt nanodots the TiN template buffer layers are inferior in terms of their [200] orientation, because they have been grown over a discontinuous layer of FePt islands. Hence some fraction of the second and third layer of FePt nanodots instead of growing along [001], assume the more energetically favorable [111] orientation.

Magnetic hysteresis curves at room temperature are shown in Fig. 5-10. The perpendicular loop shows larger coercivity and squareness when compared to the parallel loop, indicating that most nanodots are [001] oriented. However, the [200] and [111] misoriented islands, contribute to in-plane magnetization, which is significant. The perpendicular coercivity is $H_c^{\perp}$ = 1650 Oe and the parallel coercivity is $H_c^{\parallel}$ = 570 Oe.

Ideally, we expect improved magnetic properties for this system due to the possible magnetic coupling between the islands of the multilayers. But these coercivity values are less than those obtained from the continuous film and the single layered island systems. This is attributed to the inferior epitaxial quality of the multi-layered system. We consider this work as a preliminary result and future work needs to be directed to improve epitaxial quality by optimizing the growth conditions.

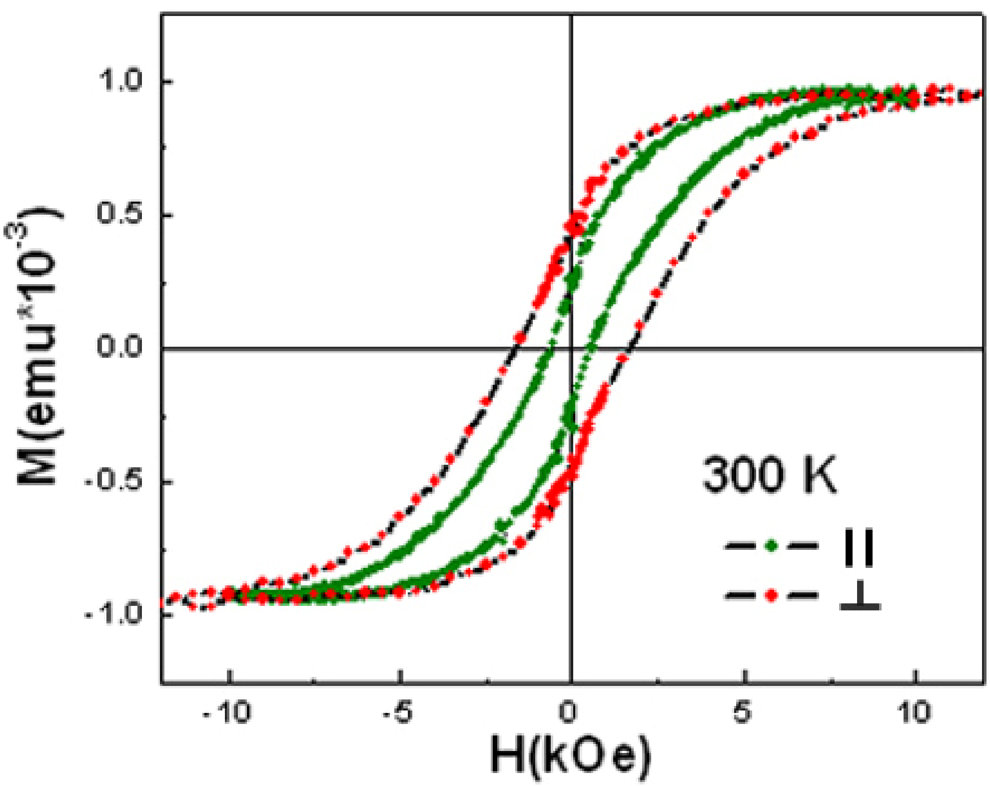

Figure 5-10. Room temperature (300 K) magnetic hysteresis loops of the FePt tri-layered nanodot sample in the perpendicular and in-plane direction.

5.5 Conclusions

In summary, we have shown that epitaxial, c-axis oriented and $L1_0$ ordered FePt nanodots can be synthesized using pulsed laser deposition. The nanodots were essentially grown on a Si (100) substrate with epitaxial TiN as a template buffer. The composition of these nanodots was $Fe_{41}Pt_{59}$, determined by RBS. XRD results showed strong c-axis orientation perpendicular to the sample surface. The order parameter (S) was estimated to be 0.75 from XRD data. Epitaxial nature of the nanodots was studied in detail using cross sectional and plan view TEM analysis. TEM results revealed that the nanodots are well separated and have an average size = 18 nm and thickness = 5 nm. It was also shown that each FePt nanodot is a single crystal, and is oriented along its c-axis and shows $L1_0$ ordering. Magnetic hysteresis measurements showed that the perpendicular loops have higher coercivity, higher squareness and higher remanence when compared to the parallel loops. The perpendicular coercivity ($H_c^{\perp}$) at 300 K in the range of 3200 Oe is highly desirable for magnetic recording applications.

References

1. S. Sun, C. B. Murray, D. Weller, L. Folks, and A. Moser, Science **287**, 1989 (2000).
2. C. W. White, S. P. Withrow, K. D. Sorge, J. D. Budai, J. R. Thompson, and L. A. Boatner, J. Appl. Phys. **93**, 5656 (2003).
3. J. A. Christodoulides, Y. Huang, Y. Zhang, G. C. Hadjipanayis, I. Panagiotopoulos, and D. Niarchos, J. Appl. Phys. **87**, 6938 (2000).
4. M-G. Kim, S-C. Shin, and K. Kang, Appl. Phys. Lett. **80**, 3802 (2002).
5. R. H. Kodama, J. Magn. Magn. Mater. **200**, 359 (1999).
6. O. Fruchart, J. P. Nozieres, W. Wernsdorfer, and D. Givord, Phys. Rev. Lett. **82**, 1305 (1999).
7. D. Kumar, J. Narayan, T. K. Nath, A. K. Sharma, A. Kvit, and C. Jin, Solid State Communications, **119**, 63 (2001).
8. B. D. Cullity, *Introduction to Magnetic Materials*, Addison-Wesley, Readings, MA 1972.
9. D. Weller, A. Moser, L. Folks, M. E. Best, W. Lee, M. F. Toney, M. Schwickert, J. U. Thiele, and M. F. Doerner, IEEE Trans. Magn. **36**, 10 (2000).
10. Z. Gai, J. Y. Howe, J. Guo, D.A. Blom, E. W. Plummer, and J. Shen, Appl. Phys. Lett. **86**, 023107 (2005).
11. K. Sato, B. Bian, T. Hanada, and Y. Hirotsu, Scr. Mater. **44**, 1389 (2001).
12. M. Tanase, N. T. Nuhfer, D. E. Laughlin, T. J. Klemmer, C. Liu, N. Shukla, X. Wu, and D. Weller, J. Magn. Magn. Mater. **266**, 215 (2003).

13. R. K. Singh and J. Narayan, Phys. Rev. B **41**, 8843 (1990).

14. T. Shima, T. Seki and, K. Takanashi, J. Magn. Soc. Jpn. **28,** 501 (2004).

15. T. Seki, T.Shima, K. Takanashi, E. Matsubara, and K. Hono, Appl. Phys. Lett. **82**, 2461 (2003).

16. A. Gupta, H. Wang, A. Kvit, G. Duscher, and J. Narayan, J. Appl. Phys. **93**, 5210 (2003).

17. A. Cebollada, D. Weller, J. Sticht, G.R. Harp, R. F. C. Farrow, R. F. Marks, R. Savoy, and J. C. Scott, Phys. Rev. B. **50**, 3419 (1994).

18. K. Barmak, J. Kim, L. H. Lewis, K. R. Coffey, M. F. Toney, A.J . Kellock, and J. U. Thiele, J. Appl. Phys. **98**, 033904 (2005).

19. Honghui Zhou, PhD Thesis, North Carolina State University (2004).

20. S. Hong and M. H. Yoo, J. Appl. Phys. **97**, 084315 (2005).

21. Y. K. Takahashi, K. Hono, T. Shima, and K. Takanashi, J. Magn. Magn. Mater. **267**, 248 (2003).

22. Y. K. Takahashi and K. Hono, Scr. Mater. **53**, 403 (2005).

Chapter 6

6 Structure-magnetic property correlations in the epitaxial $Fe_{50}Pt_{50}$ system

6.1 Abstract

We present findings on the effect of microstructure on magnetic properties of the epitaxial $Fe_{50}Pt_{50}$ system. Epitaxial c-axis oriented FePt was synthesized on Si (100) using TiN as a template buffer. The microstructure was progressively varied from a 9 nm nanoparticle system to a 30 nm thick continuous thin film. We found that individual nanoparticles showed higher coercivity than the continuous thin film. Within the nanoparticle regime coercivity increased with increasing particle size. The highest coercivity of 13,500 Oe was realized for a bead-like microstructure, when the individual nanoparticles just begin to merge to form a continuous thin film.

6.2 Introduction

Over the past couple of decades there has been an ever increasing demand for digital information storage. To cope with this need, hard disks with minimum size are required to store maximum information. In this context, considerable attention has been focused on the synthesis and study of magnetic nanoparticles for high-density magnetic recording applications [1]. Interesting properties are observed when the dimensions of magnetic particles are tailored to sizes comparable with the characteristic magnetic length scales such as magnetic exchange length and domain-wall width [2]. Inherent properties of a magnetic system like saturation magnetization, Curie temperature, anisotropy and domain reversal are affected by reduction in particle size. For the purpose of high density magnetic storage, the most relevant property that is associated with the size reduction is transition to single domain state that manifests changes in coercivity, remanence and domain reversal mechanisms. Also, well-separated magnetic nanoparticles will have minimal magnetic coupling, leading to better signal to noise ratio that is essential for magnetic recording applications [3].

With the current technology, that uses CoCrPt ($k_u = 2\times10^6$ erg/cm^3) as the recording medium and a longitudinal magnetic recording approach, one can get to areal densities as high as 100 Gbit/in^2. However, to get beyond this limit one must look for new materials and improved recording techniques. The FePt system is an attractive candidate for high-density storage due to its extremely high uniaxial magnetocrystalline anisotropy energy ($k_u = 7\times10^7$ erg/cm^3) [4]. The high magnetocrystalline anisotropy permits the use of smaller size particles before the onset of superparamagnetism; this directly leads to higher recording densities. Additionally, the c-axis aligned FePt system is well suited for perpendicular recording. A four-fold increase in storage density can be realized by employing the perpendicular magnetic recording approach [5]. It is important to realize that physical vapor deposition methods based on substrate controlled epitaxy are more suitable for synthesizing c-axis oriented FePt nanostructures. In this chapter we present a systematic study of the effect of microstructure on coercivity for the FePt system. These structures were processed by pulsed laser deposition (PLD). Since PLD is a high energy non-equilibrium processing technique (the energy of the ablated species can be as high as 10-100 eV) the processing temperatures for FePt growth could be reduced to 500 °C. As a part of this study, we have perfected the epitaxial growth of c-axis FePt on single crystal Si (100) substrates. This aspect of our research holds tremendous future promise in terms of integration of magnetic devices with Si (100) based technology. To date most researchers have used MgO as the substrate for growing epitaxial c-axis oriented FePt [6]. However, MgO would be unsuitable from a viewpoint of practical applications, because of its high single-crystal cost, limited wafer size, hygroscopic nature and poor mechanical properties. We achieved FePt growth along the magnetically hard c-axis using epitaxial TiN as the template buffer. TiN is metallic (ρ = 15 $\mu\Omega$.cm), non-magnetic and also acts as a diffusion barrier between FePt and Si.

6.3 Experiment

The FePt/TiN/Si heterostructure was synthesized by pulsed-laser deposition (PLD). For PLD, a KrF excimer laser with 248 nm wavelength and 25 ns pulse duration was used. Growth parameters for FePt are as follows; growth temperature = 500 °C, energy density = 4-5 J/cm^2, base pressure = 10^{-7} torr and growth rate = 0.08 nm/s. X-ray diffraction measurements were done using a Rigaku Geigerflex diffractometer with Cu

$K\alpha$ (wavelength = 0.154 nm) radiation and a graphite monochromator. Transmission electron microscopy (TEM) was performed using a JEOL 2010F TEM operating at 200 KV with a point to point resolution of 0.18 nm. Magnetic measurements were performed using a superconducting quantum interference device (SQUID). The composition was determined to be Fe_{50} Pt_{50} by Rutherford backscattering spectrometry (RBS).

6.4 Results and discussion

The synthesis of the heteroepitaxial FePt/TiN/Si(100) structure poses a great challenge because of the large misfit strains (ε) involved, $\varepsilon_{FePt/TiN}$ = 9.5 % and $\varepsilon_{TiN/Si}$ = 22 %. Epitaxy in such large mismatch systems was achieved by a new paradigm of thin film growth called domain matching epitaxy (DME), where integral multiples of lattice planes match across the interface [7]. In the case of FePt/TiN epitaxy 10/9 and 11/10 domains alternate (with a frequency factor of 0.547) to accommodate the 9.5% misfit in the system [8]. Here, by a 10/9 domain we mean that 10 planes of FePt match with 9 planes of TiN. Epitaxy of TiN on Si, which has a 22% misfit, was achieved by alternating 3/4 and 4/5 domains with almost equal frequency. Figure 6-1 shows the XRD patterns of two different microstructures; (a) 30 nm thick films and (b) 18 nm sized nano-islands. There is only one family of TiN reflections (200) and (400) indicating that it grows epitaxially on Si (100). FePt has three prominent reflections, the (001) and (003) superlattice peaks and the (002) fundamental peak. The superlattice reflections show up due to the presence of $L1_0$ order in the FePt film. The X-ray scan of the nano-island sample (Fig. 6-1b) shows lower intensity FePt peaks, because the amount of material deposited in this case is much less when compared to the continuous thin film.

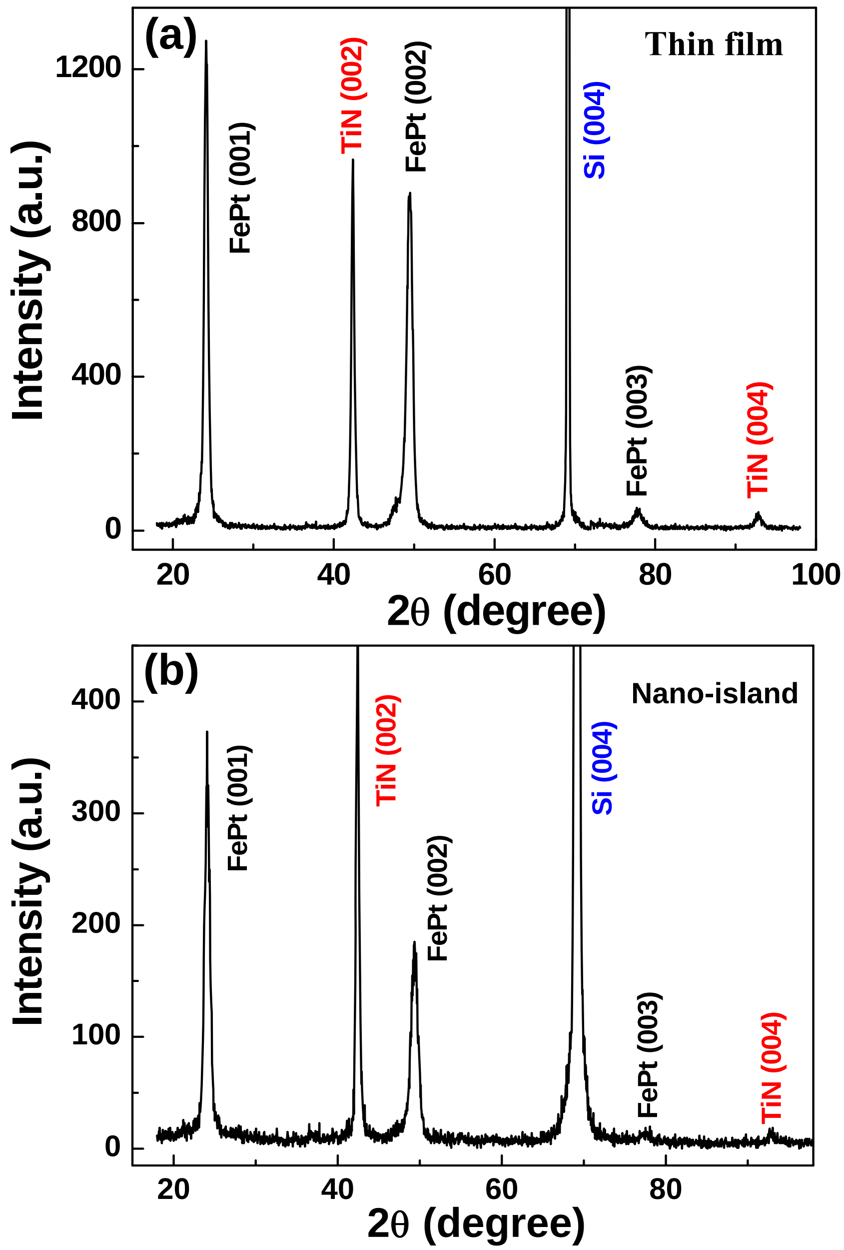

Figure 6-1. (a) X-ray scan of the 30 nm thick continuous thin film (b) X-ray scan of the 18 nm nano-island system.

The order parameter for all the samples in this study was in the range of $S = 0.92 \pm 0.04$. The order parameter (S) was calculated using the following equation [9]:

$$S^2 = (I_{001}/I_{002})_{exp} / (I_{001}/I_{002})_{cal}, \quad (1)$$

where I_{001} and I_{002} are the integrated intensity of the (001) superlattice peak and (002) fundamental peak and $(I_{001}/I_{002})_{exp}$ and $(I_{001}/I_{002})_{cal}$ are the experimental and calculated peak intensity ratio, respectively.

Epitaxy and order in the system was confirmed by plan-view and cross-section TEM. Selected area electron diffraction patterns (shown as insets in Fig. 6-2) along the <110> and <001> zones were analyzed to reveal the following epitaxial relationship; FePt (001) <001>║TiN (100) <001>║ Si (100) <001>. In this study different microstructures were synthesized and studied as shown in Fig. 6-2. Starting from the smallest particle size of 9 nm (Fig. 6-2a), the particle size was steadily increased to 18 nm (Fig. 6-2b) and further up to 100 nm (Fig. 6-2c). The shape and size of the 9 nm system seems to be more uniform than the 18 nm system. In the 9 nm system the individual nanoparticles are more widely spaced, when compared to the 18 nm system which has a more dense packing. At about 90 nm the individual particles just begin to merge and form a bead-like microstructure. As the growth time is increased further the individual particles merge completely to form a continuous film as shown in Fig. 6-2(d).

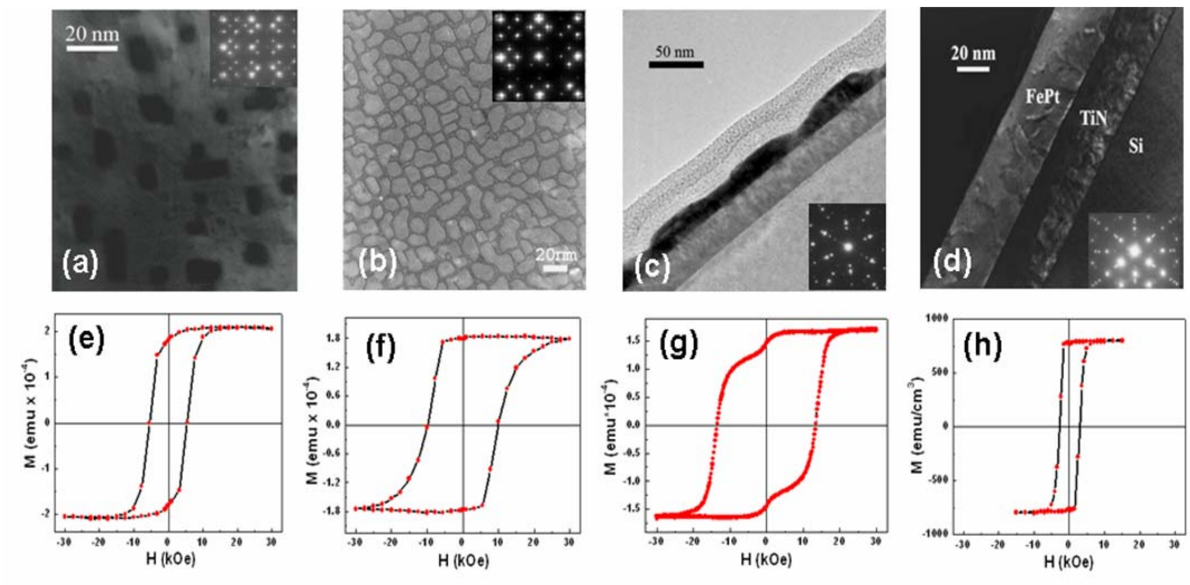

Figure 6-2. TEM images of the FePt microstructures with corresponding SAED patterns (a) 9 nm nano-island (b) 18 nm nano-island (c) 90 nm nano-island (d) continuous thin film with thickness = 30 nm. The corresponding perpendicular hysteresis loops are shown in (e)-(h).

Here it is important to note that, FePt grows via the 3D-Volmer Weber growth mode on TiN. The values of surface energy also suggest a 3D-type of growth mode. Surface energy for relaxed geometries of (100) TiN (σ_{TiN}) is reported to be 1.28 J/m^2 [10] and for (001) FePt (σ_{FePt}) it is about 2.18 J/m^2 [11]. From these values it is clear that,

$$\sigma_{FePt} + \sigma_{interface} > \sigma_{TiN} \tag{2}$$

This suggests a Volmer-Weber type of growth mode. In this study, it is important to realize that for short deposition times, individual 3D islands are formed that finally merge to form continuous films at longer growth times. The island size at which merger occurs can be controlled by the growth temperature. At 500 °C, islands 90 nm in size begin to merge. Preliminary experiments at higher temperatures close to 600 °C have shown that the islands are still separated at a particle size of about 150 nm. The magnetic properties vary according to the microstructure, as shown in figures 6-2e to 6-2h. Shown in these figures are the hysteresis loops perpendicular to the sample surface. The squareness of these loops falls in the range of 0.95 ± 0.03. As the particle size increases from 9 nm to 18 nm, the coercivity improves from 5800 Oe to 10,000 Oe. For the 90 nm bead-like structure, where the islands are just beginning to merge, the coercivity is as high as 13,500 Oe. And finally for the 30 nm thick continuous film the coercivity drops to 3000 Oe. This trend is plotted in Fig. 6-3, which follows the classical curve between coercivity and particle size. On this curve, the two points D_1 and D_2 are of prime importance. D_1 is the particle size at which superparamagnetism sets in and D_2 is the particle size at which the system transforms from a single domain state to a multi domain state. For the FePt system simple theoretical calculations can be applied to evaluate D_1 [12] and D_2 [13].

$$D_1 = (47.77kT/k_u)^{1/3} = 3\ \text{nm} \tag{3}$$

Where T is the temperature and k_u is the anisotropy constant (7×10^7 erg/cm^3). At temperature T = 300 K we calculate D_1 = 3 nm.

$$D_2 = 24(Ak_u)/NM^2_s = 155\ \text{nm} \tag{4}$$

Where A is the stiffness constant = 10^{-6} erg/cm, N is the demagnetizing factor = 7.81. For FePt D_2 was calculated to be 155 nm. So when the particle size is between D_1 = 3 nm and D_2 = 155 nm, the FePt particle is a single domain. Hence the first three microstructures in our study, the 9 nm, 18 nm and 90 nm systems, fall within the single domain state. And within the single domain state, coercivity seems to increase with the particle size. In a single domain particle coercivity depends on the anisotropy energy k_uV, where k_u is the anisotropy constant and V the volume. As the volume (size) of the particle increases, the anisotropy energy increases and it becomes increasingly difficult to reverse the spins, resulting in higher coercivity. The continuous film, shown in Fig. 6-2d, contains multiple domains and hence the coercivity drops sharply. In a multi-domain state the domain reversal occurs by growth of a favorably oriented domain (i.e. one that has its net moment directed closest to the applied magnetic field direction) at the expense of other un-favorable domains. Domain reversal by growth of domains in a multi-domain state requires much smaller fields when compared to domain rotation that requires overcoming the anisotropic forces in a single domain state. Hence, multi-domain particles have lower coercivity. Moreover, the system in Fig. 6-2d is a perfect epitaxial single crystalline thin film, with minimal defects. Defects can act as domain pinning sites. The absence of defects in 6-2d decreases the coercivity even further.

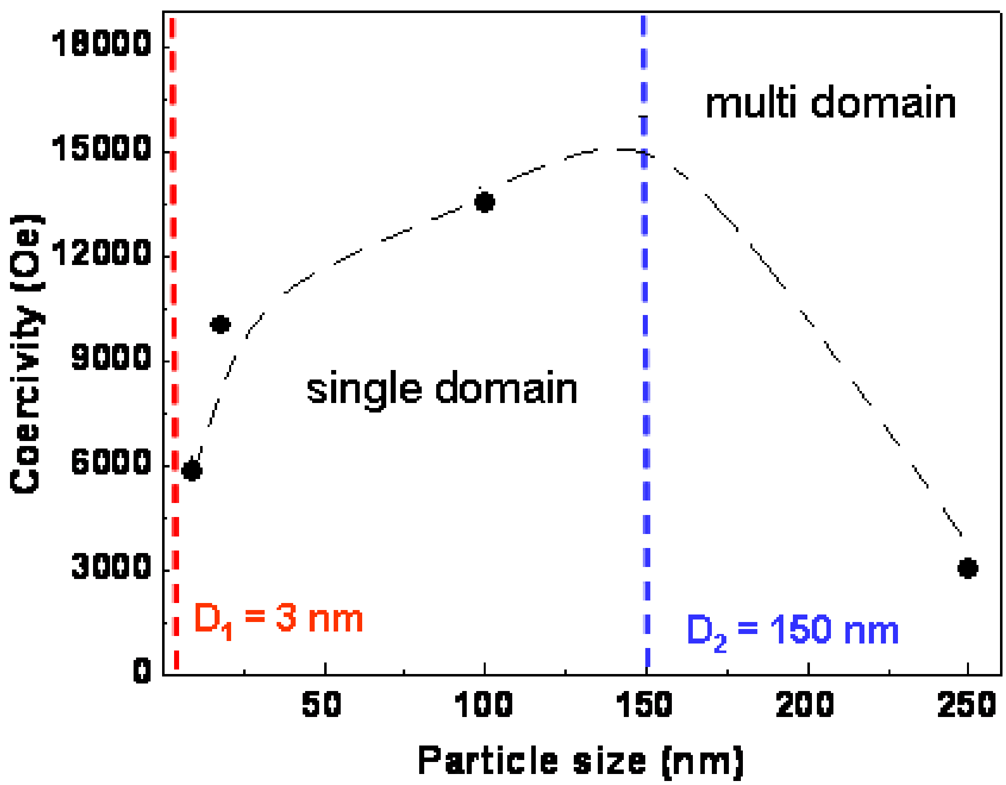

Figure 6-3. Plot between coercivity and particle size. The figure also shows the single and multi domain regions in the FePt system.

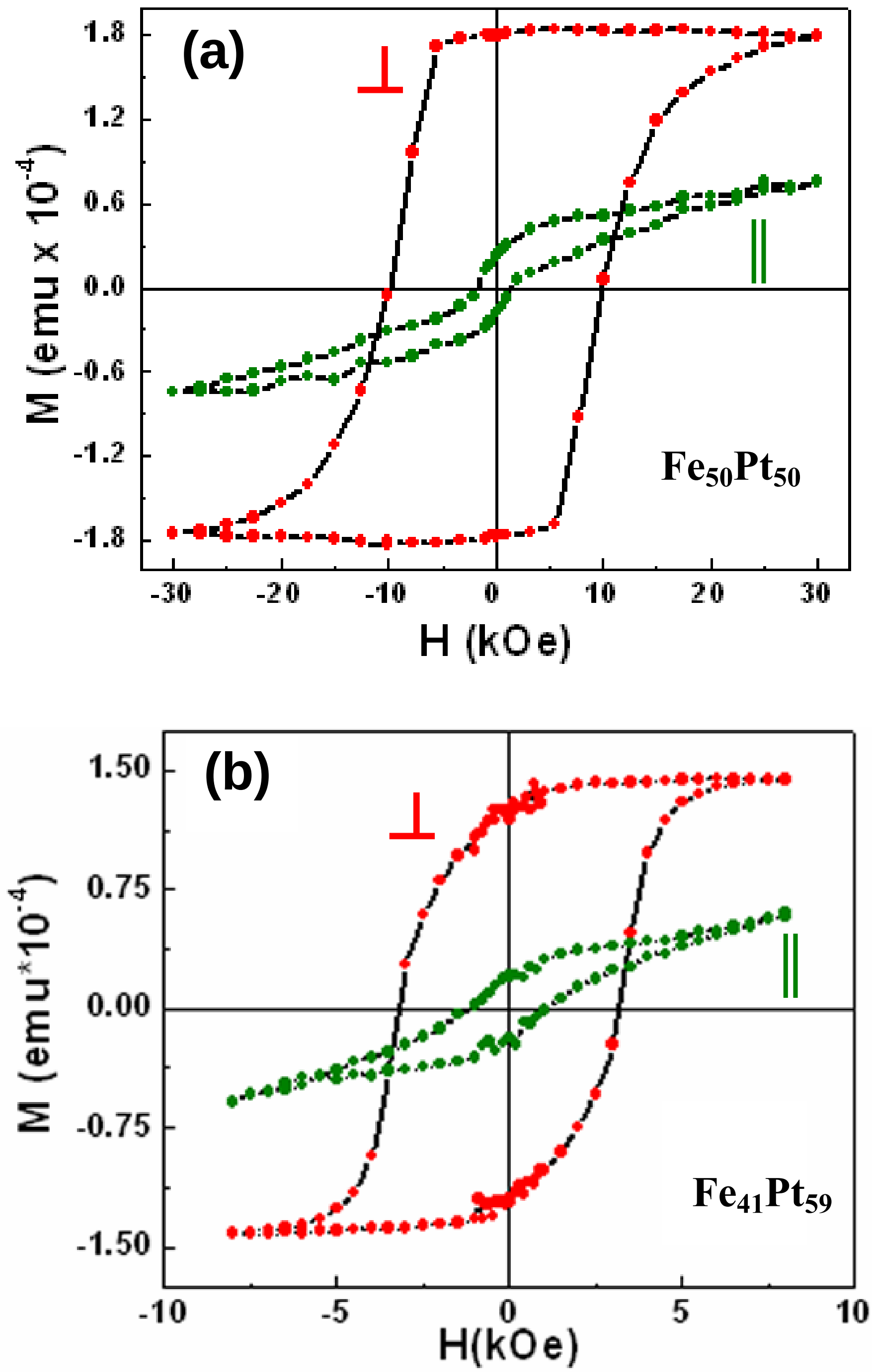

Figure 6-4. (a) Magnetic hysteresis curve for the 18 nm nano-island system with composition $Fe_{50}Pt_{50}$ (b) Hysteresis loop for the $Fe_{41}Pt_{59}$ composition.

The best microstructure in terms of magnetic storage would be the 18 nm sized system shown in Fig. 6-2b. If we assume one bit of information to be stored in each island, a storage capacity of 1 Terabit/in^2 can be realized for this system. For a $Fe_{50}Pt_{50}$ composition this microstructure has a perpendicular coercivity of about 10,000 Oe (Fig. 6-2f). The current read/write technology in the magnetic industry may not be able to handle such high coercivities. The current technology is built to operate on systems with coercivities in the range of 2000-5000 Oe. Keeping this in mind, the Pt rich off-stoichiometric $Fe_{41}Pt_{59}$ system discussed in previous chapter and reproduced in Fig. 6-4 may be ideal. For both the 50:50 and 49:51 systems the in-plane magnetic loops are also shown. Due to the high degree of c-axis orientation, the perpendicular loops have high coercivity, remanence and squareness when compared to the in-plane loops. In-plane magnetization can be attributed to structural imperfections like small fraction of FePt islands existing in the disordered phase.

6.5 Conclusions

In summary, we have studied the variation of coercivity with microstructure for the epitaxial $Fe_{50}Pt_{50}$ system. Growth of the high misfit FePt/TiN/Si(100) heterostructure was accomplished by domain matching epitaxy. It was shown that individual nanoparticles being in a single domain state have larger coercivity than continuous thin films. Within the nanoregime, coercivity increased with increasing particle size. The continuous thin film showed the lowest coercivity because of its multi domain state and lack of defects or pinning sites. We also showed that by varying the composition, we can control the coercivity and hence can tailor the system for diverse applications.

References

1. S. Sun, C. B. Murray, D. Weller, L. Folks, and A. Moser, Science **287**, 1989 (2000).
2. R. H. Kodama, J. Magn. Magn. Mater. **200**, 359 (1999).
3. N. A. Spaldin, Magnetic materials: Fundamentals and device applications, Cambridge University Press (2003).
4. D. Weller, A. Moser, L. Folks, M. E. Best, W. Lee, M.F. Toney, M. Schwickert, J. U. Thiele, and M.F. Doerner, IEEE Trans. Magn. **36**, 10 (2000).
5. K. Ouchi, and N . Honda, IEEE Trans. Magn. **36**, 16 (2000).
6. K. Barmak, J. Kim, L.H. Lewis, K.R. Coffey, M.F. Toney, A.J. Kellock, and J.U. Thiele, J. Appl. Phys. **98**, 033904 (2005).
7. J. Narayan, and B.C. Larson, J. Appl. Phys. **93**, 278 (2003).
8. G.R. Trichy, D. Chakraborti, J.T. Prater, and J. Narayan, Journal of Physics D: Applied Physic, in press (2007).
9. A. Cebollada, D. Weller, J. Sticht, G.R. Harp, R. F. C. Farrow, R. F. Marks, R. Savoy, and J. C. Scott, Phys. Rev. B. **50**, 3419 (1994).
10. Z. Honghui, PhD Thesis, North Carolina State University (2004).
11. S. Hong and M. H. Yoo, J. Appl. Phys. **97,** 084315 (2005).
12. B. D. Cullity, Introduction to Magnetic Materials, Addison-Wesley, Readings, MA (1972).
13. G. Q. Li, H. Takahoshi, H. Ito, H. Saito, S. Ishio, T. Shima, and K. Takanashi, J. Appl. Phys. **94,** 5672 (2003).

Chapter 7

7 Magnetoresistance of the $L1_0$ ordered epitaxial FePt system

7.1 Abstract

The magnetoresistance of highly ordered (001) epitaxial FePt thin films has been investigated. The $Fe_{50}Pt_{50}$ films were grown by pulsed laser deposition and showed a bead-like microstructure. This system showed a maximum MR of 0.57 % at room temperature, when the field was perpendicular to the current. The MR loops showed hysteresis behavior consistent with the MH loops. Anisotropy in resistance was observed when the orientation was changed such that the field was parallel to current flow. The MR behavior in the FePt system has been attributed to spin dependent electron scattering and scattering due to domain walls.

7.2 Introduction

The FePt system has been the focus of numerous research studies in recent years owing to its superior magnetic properties [1 and references therein]. The high uniaxial magnetocrystalline anisotropy (7×10^7 erg/cm^3) renders this system suitable for ultra high density storage and recording applications [2]. Though much work has been done on FePt for storage purposes, its magnetoresistance (MR) properties have been left largely unexplored. Such a study will be useful for fabricating devices that require both magnetic storage and sensor applications.

Within the limited literature available, there are studies that report MR behavior of FePt, both in the thin film and granular forms [3-5]. The microstructure, extent of $L1_0$ order and magnetization direction affect the MR properties in the FePt system [3-5]. Ishio et. al. [3] have reported a GMR of 0.18 % in equiatomic sputtered thin films. In a FePt-Ag composite film a GMR as high as 0.7 % has been reported by Zhang et. al [4].

In this chapter, we report on the MR studies of epitaxial FePt thin films, with a bead-like microstructure, as a function of temperature. The strength of this study stems from the use of Si (100) as the substrate. Using Si enables potential integration of our structures with modern day microelectronic devices. In order to align the FePt structures along the magnetically hard c-axis, a TiN template buffer layer was used. Additionally, TiN also acts as a diffusion barrier between the FePt film and the Si substrate.

7.3 Experiment

The FePt thin films were synthesized by pulsed laser deposition. A KrF excimer laser with wavelength = 248 nm and pulse width = 25 ns was used for this purpose. Growth parameters for FePt are as follows: base pressure = 10^{-7} torr, energy density = 5 J/cm^2 and temperature = 500 °C. The synthesis of the heteroepitaxial FePt/TiN/Si (100) structure poses a great challenge because of the large misfit strains (ε) involved, $\varepsilon_{FePt/TiN}$ = 9.5 % and $\varepsilon_{TiN/Si}$ = 22 %. Epitaxy in such large mismatch systems was achieved by a new paradigm of thin film growth called domain matching epitaxy (DME) [6]. The epitaxial concepts and domain matching of the FePt/TiN [7] and TiN/Si [6] system have been discussed else where.

The FePt samples were characterized in detail by X-ray diffraction and transmission electron microscopy (TEM). For transmission electron microscopy, a JEOL 2010F microscope with a point to point resolution of 1.8 nm was used. The MH and MR measurements were performed using a Quantum Design physical property measurement system (PPMS) equipped with a vibrating sample magnetometer (VSM) setup. A four probe arrangement was used for transport measurements. The bias currents used were in the range of 400-500 μA. The MR measurements (up to H = ±70 KOe) were performed in two orientations: (A) the perpendicular orientation where the field was perpendicular to the current and the sample surface and (B) the in-plane orientation where the field was parallel to the current and sample surface. In both the orientations the direction of the current remains the same i.e., parallel to the sample surface.

7.4 Results and discussion

This section is divided into two parts. The first section will discuss MR results of the bead-like $Fe_{50}Pt_{50}$ thin film. In the second section preliminary MR results pertaining to a $Fe_{41}Pt_{59}$ multilayer structure will be discussed.

Section 1:

Figure 7-1a shows the cross section TEM image of the $Fe_{50}Pt_{50}$ sample under study. It shows a bead-like microstructure, when the individual nanoislands just begin to merge to form a continuous thin film. The FePt growth on TiN follows a Volmer-Weber (3D) mode of growth. During the initial stages of growth individual 3D islands are formed and for longer deposition times these islands grow and eventually merge to form a continuous thin film (see chapter 6 for more details). The beads/islands have an average size of 90 nm and they are about 22 nm thick at the center of the bead. Figure 7-1b is the corresponding SAD pattern. The alignment of the FePt, TiN and Si spots in all the directions indicates perfect cube-on-cube epitaxy. The epitaxial relationship is given as FePt (001) <001>‖TiN (100) <001>‖ Si (100) <001>. X-ray scans showed strong [001] growth orientation and presence of superlattice peaks. The order parameter was calculated to be 0.90.

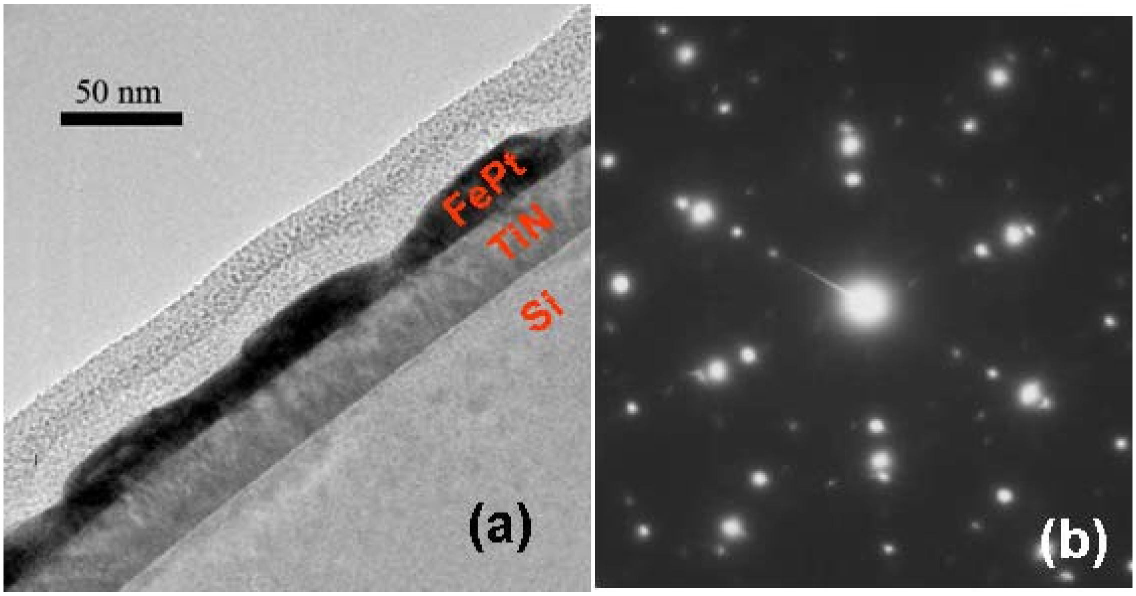

Figure 7-1. (a) Cross section TEM image of the bead-like FePt thin film. (b) The corresponding SAD pattern in a <110< zone.

Figure 7-2 shows the MH loop at 300 K for the $Fe_{50}Pt_{50}$ sample under study. The perpendicular loop showed improved coercivity, remanence and squareness when compared to the parallel loop, indicative of the easy axis of magnetization being oriented perpendicular to the sample surface. The perpendicular coercivity was as high as 13500 Oe and in the in-plane direction the coercivity was 5400 Oe. In-plane remanent magnetization can be attributed to the small fraction of FePt that remains in the disordered phase and some residual misoriented fraction of FePt that has its c-axis along the film plane.

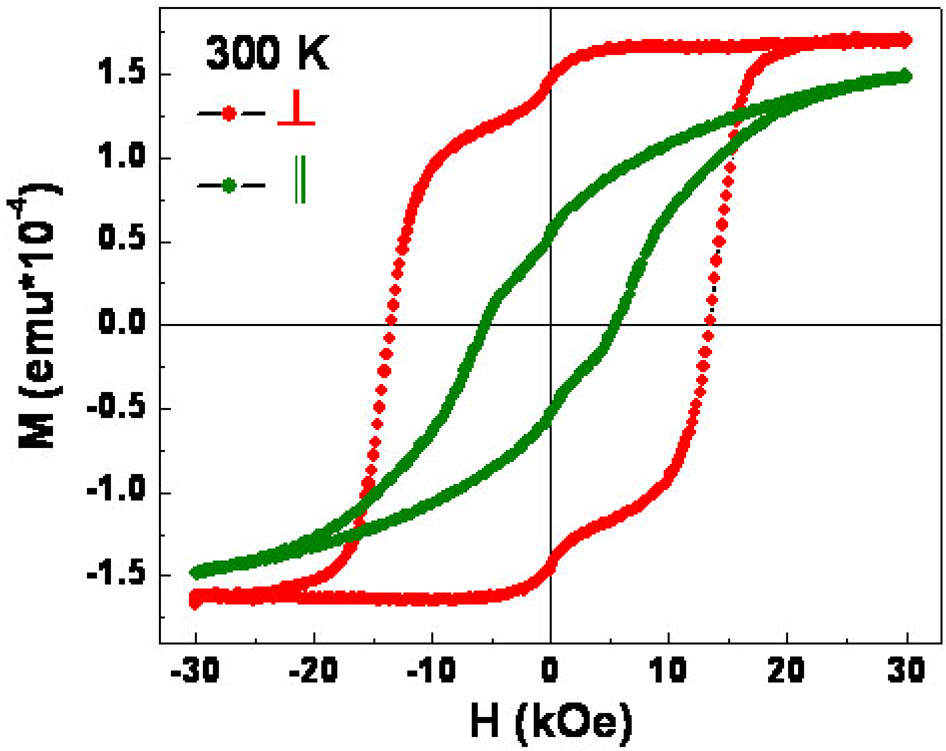

Figure 7-2. Perpendicular and in-plane MH loops for the bead-like FePt thin film at room temperature.

The MR results are shown figures 7-3a to 7-3d. The magnetoresistance was calculated using the following equation,

$$MR\% = \frac{(R - R_c)\times 100}{R_c} \qquad (1)$$

Where R is the resistance at any field and R_c is the resistance at H_c (coercive field). It is important to note that maximum resistance is observed at H_c. Hence, in this study we define MR in terms of the resistance at coercive field. Figures 7-3a and 7-3b show the MR behavior in the perpendicular orientation, i.e. the magnetic field is perpendicular to the current and the sample surface. It is important to realize that in this case the field is along the magnetic easy axis of the sample. The FePt system shows negative magnetoresistance, i.e. resistance decreases with increasing field. In Fig. 7-3a as the field is swept from -70 KOe to 70 KOe, the MR follows the red curve peaking at H_c. Then as the field is swept in the reverse direction (from 70 KOe to -70KOe), the MR follows a different path along the green curve. This shows that we have hysteresis in the system. Comparing Fig. 7-3a and the perpendicular loop in Fig. 7-2 we find that the hysteresis behavior is consistent, in that the coercive field remains the same ($H_c^{\perp}$ = 13500 Oe). At 300 K and a 70 KOe field the maximum MR obtained was 0.57 % (see Fig. 7-3a). Close to zero field the system shows a switching effect, i.e. the resistance changes sharply with change in field. This can be attributed to the presence of a soft magnetic phase in the system (arising due to non-uniformity in the FePt partice size or presence of Fe particulates), that also shows up as kink in the MH loop (see Fig. 7-2). Figure 7-3b shows the MR measurement in the same orientation at 10 K. At this lower temperature the trends in the MR behavior remain the same. The data is much smoother and the switching effect is pronounced. The maximum value of MR increases to 0.74 %.

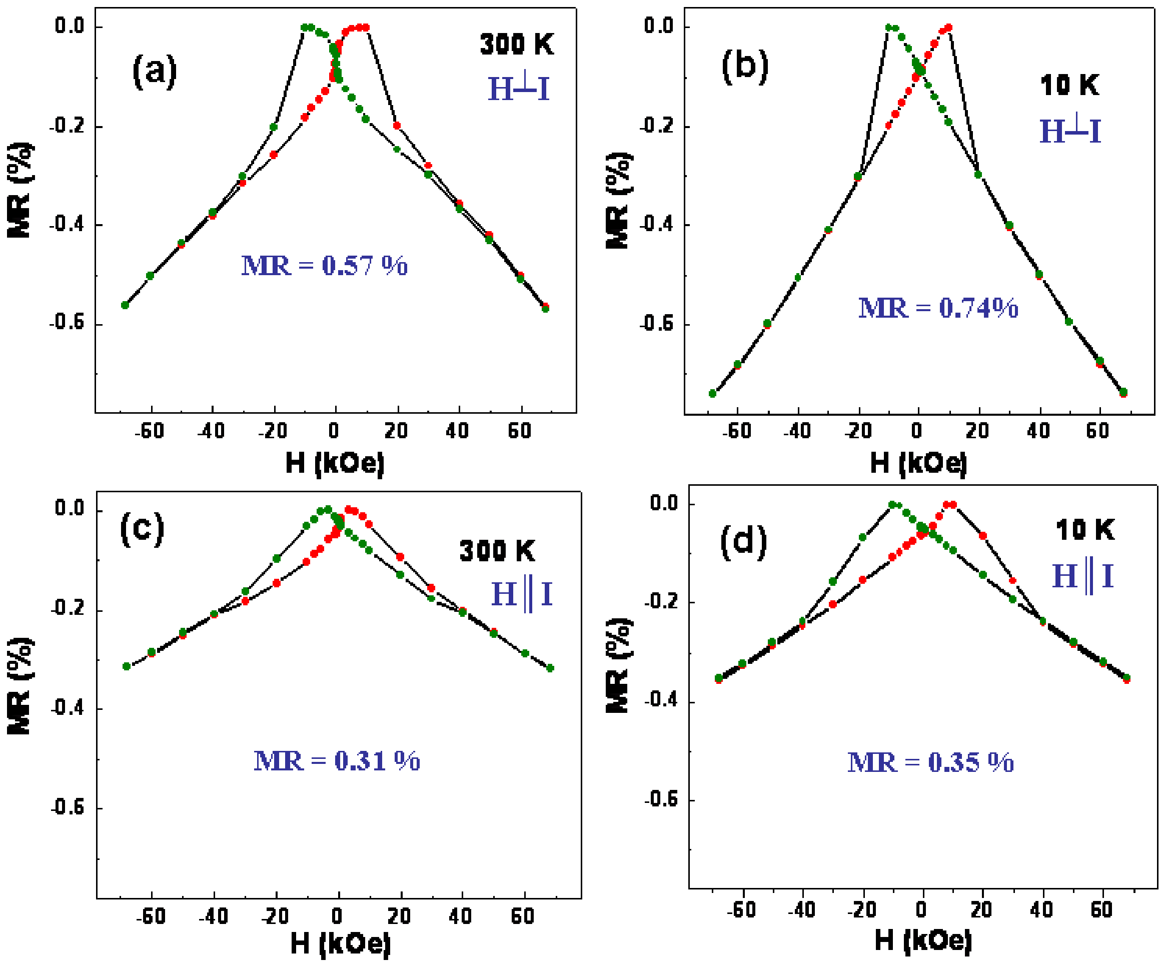

Figure 7-3. Magnetoresistance of the bead-like $Fe_{50}Pt_{50}$ thin film in the perpendicular (H┴I) and in-plane (H║I) orientation at 300 K and 10 K (see text for more details).

The MR results for the in-plane orientation are shown in figures 7-3c and 7-3d. Here, the magnetic field is parallel to the current and the sample surface, which means that the field is along the hard axis of the sample. In the in-plane orientation the MR values are lower, when compared to the perpendicular orientation. In the in-plane orientation the field tries to align the spins along their hard axis. This can be difficult to accomplish because, the spins like to stay fixed along their easy axis (energetically more favorable). So even at a high field of 70 KOe, not all the spins are aligned along the hard axis and some spins remain in the easy axis orientation. This means ordering in terms of the spins is not complete in the in-pane orientation. Hence, the MR effect in the in-plane orientation is less when compared to the perpendicular orientation. This At the 300 K the maximum MR is 0.31 % (Fig. 7-3c) and at 10 K the MR improves slightly to 0.35 % (Fig. 7-3d). The trends in the MR curve remain the same, i.e. the curves show hysteresis behavior, switching effects and they peak at coercive field. The hysteresis behavior in Fig. 7-3c reveals a coercivity of about 5100 Oe, which is consistent with the in-plane MH loop in Fig. 7-2.

The $L1_0$ ordered FePt system has a huge anisotropy constant, $K_u = 7 \times 10^7$ erg/cm^3. The higher the anisotropy constant the smaller will be the domain wall width. The domain wall thickness (δ_w) can be calculated as,

$$\delta_w = \pi \left[\frac{A}{K_u} \right]^{0.5} = 9 \text{ nm} \tag{2}$$

Where A is the stiffness constant and its value for the FePt system is about 10^{-6} erg/cm. The domain wall thickness for the FePt system was calculated to be 9 nm. It is important to realize that for FePt, the domain wall thickness is comparable to the spin diffusion length at room temperature [3,8]. Therefore, small domain wall widths can be the cause of MR in the $L1_0$ ordered FePt system.

Spin dependent electron scattering is one possible mechanism to explain the trends shown in figures 7-3a to 7-3d. At coercive field the spins in the system are oriented such that they nullify each other so that the resultant magnetic moment is zero. The randomness of the spins results in increased scattering of the electrons. Hence, resistance is a maximum at coercive field. When the field is increased beyond coercive values the spins in the system align themselves along the field direction. So at higher fields the spins are more ordered, i.e. less electron scattering occurs and resistance drops leading to a negative magnetoresistance effect. It is also important to note that in our study the MR curves do not seem to saturate even at 70 KOe magnetic fields. Similar behavior for the FePt system has been observed by Allia et. al. [8] and Zhang et. al. [4].

The MR beahvior in the FePt system can also be attributed to electron scattering by domain walls. It is known that a system with multi domains will show higher resistivity than a single domain system [5,9]. Change in resistance can also be attributed to randomness of the spins in the domain, within which electrons may get deflected at different angles due to a Hall effect [5,10]. In the bead-like structure in our system, each bead is sized about 90 nm. For the FePt system a single domain can exist up to a size of 150 nm (see chapter 5). So it is safe to assume that each bead will be a single domain, with domain walls existing at the junction between two beads. (Future work to study the domain pattern and confirm this result by magnetic force microscopy is in progress.) Therefore, at low fields the sample contains more domain walls and thus shows higher resistance. At higher fields when less number of domain walls exist the resistance values drop. Based on the above discussion the MR behavior of the FePt system can be attributed to a combined effect of domain wall and spin dependent electron scattering.

Figure 7-4 shows the anisotropy in resistance for the perpendicular and in-plane orientations at room temperature. The red loop illustrates the trend in resistance vs field for the perpendicular orientation. i.e. when the field is perpendicular to the current and the sample surface. The green loop illustrates the in-plane orientation, when the field is parallel to the current and sample surface. Higher resistance values were consistently observed in the in-plane orientation, when compared to the perpendicular orientation. A similar trend was also observed at a low temperature of 10 K. This result can be attributed to the magnetic domain structure. Yu et. al. [5] have observed that for well ordered FePt films, the domains align perpendicular to the current in the in-plane orientation leading to higher resistance values. Also, when compared to the perpendicular orientation, the orientation of the magnetic dipoles in the in-plane condition manifests a larger scattering cross-section for the current (conducting electrons). Hence, resistance values in the in-plane orientation are higher.

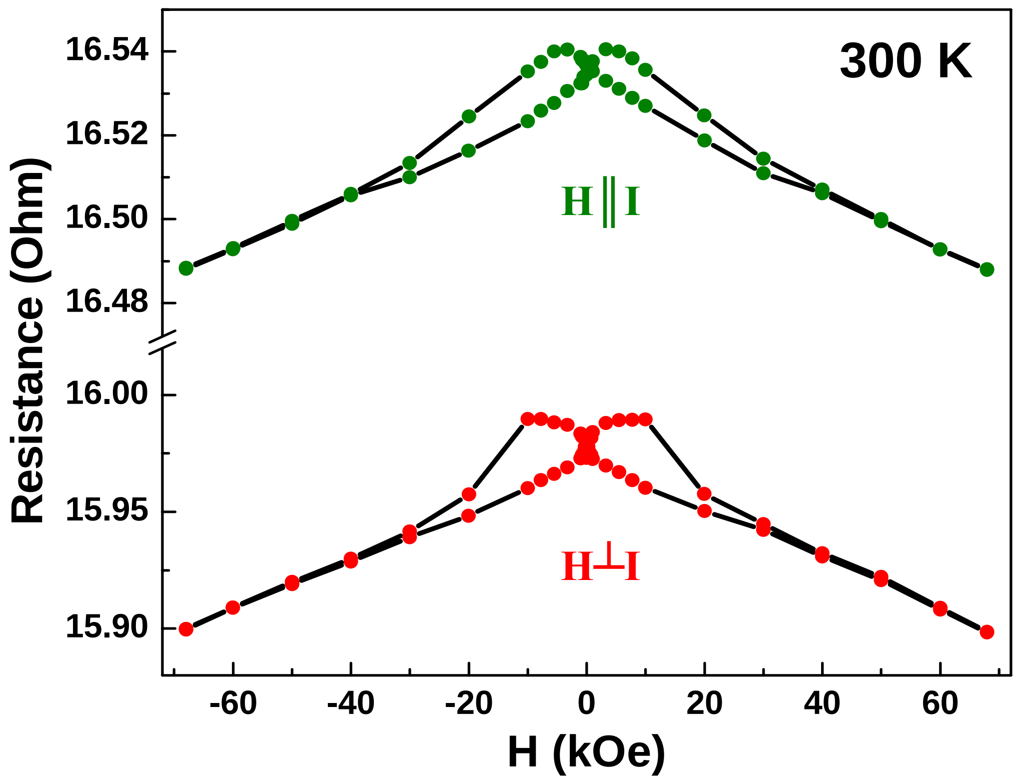

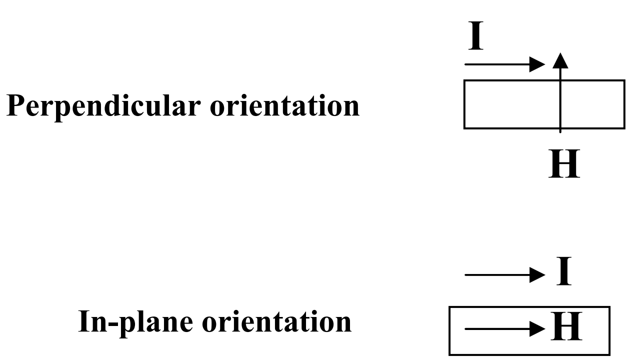

Figure 7-4. Anisotropy in resistance for the perpendicular and in-plane orientations at room temperature.

Section 2:

Some preliminary magnetoresistance studies were also performed on an off-stoichiometric $Fe_{41}Pt_{59}$ multi-layered thin film system. Figure 7-5 is a cross section TEM image of the multi-layered sample. The different layers and their thickness are clearly marked in this figure. Essentially, the structure consists of two FePt layers that sandwich a TiN layer in between. The two FePt layers have similar thickness, equal to 12 nm. The TiN barrier layer is 22 nm thick. The XRD scan of this sample is shown in Fig. 7-6. Careful XRD and TEM diffraction pattern analysis has shown that the inner (first) FePt layer is [001] oriented, i.e. it has its c-axis oriented perpendicular to the sample surface. The top (second) FePt layer deteriorates in terms of its [001] epitaxy and has a [111] orientation. This is because the first FePt layer has a perfectly epitaxial TiN (200) template to grown on. The second FePt layer has to grow on the TiN barrier layer, which is inferior in terms of its [002] orientation. Hence the second FePt layer instead of growing along [001], assumes the more energetically favorable [111] orientation. It is important to realize that the first and second layers will have different individual coercivity values due their different crystallographic orientations.

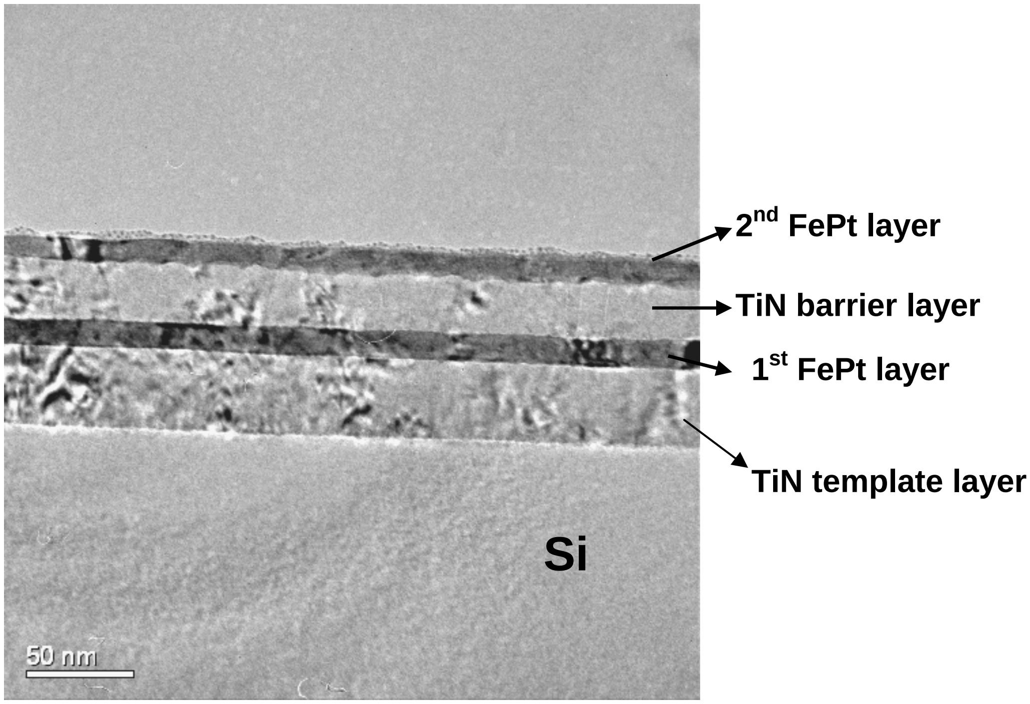

	Thickness (nm)
1st FePt layer	12
2nd FePt layer	12
TiN barrier layer	22
TiN template layer	35

Figure 7-5. Cross section TEM image of the $Fe_{41}Pt_{59}$ multi-layered system. The thicknesses of the layers are also shown.

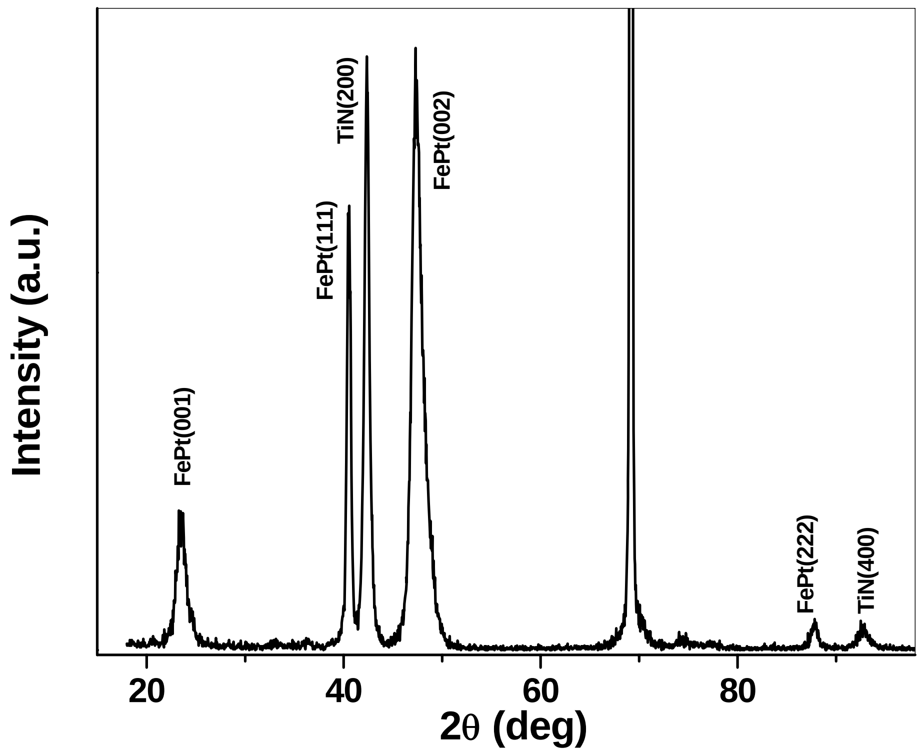

Figure 7-6. XRD scan of the $Fe_{41}Pt_{59}$ multi-layered system.

Figure 7-7 shows the MR results of the multi-layered $Fe_{41}Pt_{59}$ sample. Figures 7-7a and 7-7b show the MR behavior in the perpendicular orientation, i.e. the magnetic field is perpendicular to the current and the sample surface. At 10 K, the MR behavior is shown in Fig. 7-7b. In this case, the $Fe_{41}Pt_{59}$ multi-layered system shows negative magnetoresistance at all fields. The MR loops show hysteresis, i.e. as the field is swept from -70 KOe to 70 KOe the MR follows the red curve and when field is swept in the opposite direction it follows a different path along the green curve. At 10 K the maximum MR in the perpendicular orientation is about 1.12 %. When the temperature is reduced to

2 K, the trend in MR changes drastically (see Fig. 7-7a). In this case, at fields close to zero the system shows positive magnetoresistance, i.e. resistance increases with increase in field. Positive MR is observed up to the coercive field of about 5.8 KOe. At higher fields beyond ± 5.8 KOe the system shows negative magnetoresistance. The maximum MR obtained in the perpendicular orientation at 2 K is about 1.07 %. Again the MR measurements show hysteretic behavior. The red and the green curve show the forward and reverse field cycles in the MR experiment. It is important to note that there is an asymmetry in the red and the green curves on either side of the origin. The peaks on either side of the origin in the red curve (and the green curve) show different MR values. This could be due to the difference in the coercivities of the top and the bottom FePt layers. Figure 7-7c shows the MR measurement at 2 K in the in-plane orientation. The maximum MR decreases slightly to 0.85 %, but the trend remains the same as in the perpendicular orientation. Further experiments that include MFM studies (to study domain formation), change in TiN barrier layer thickness and change in the current direction (perpendicular to surface through the FePt layers) are in progress in order to fully understand and explain these interesting trends in MR at lower temperatures for the multilayered system.

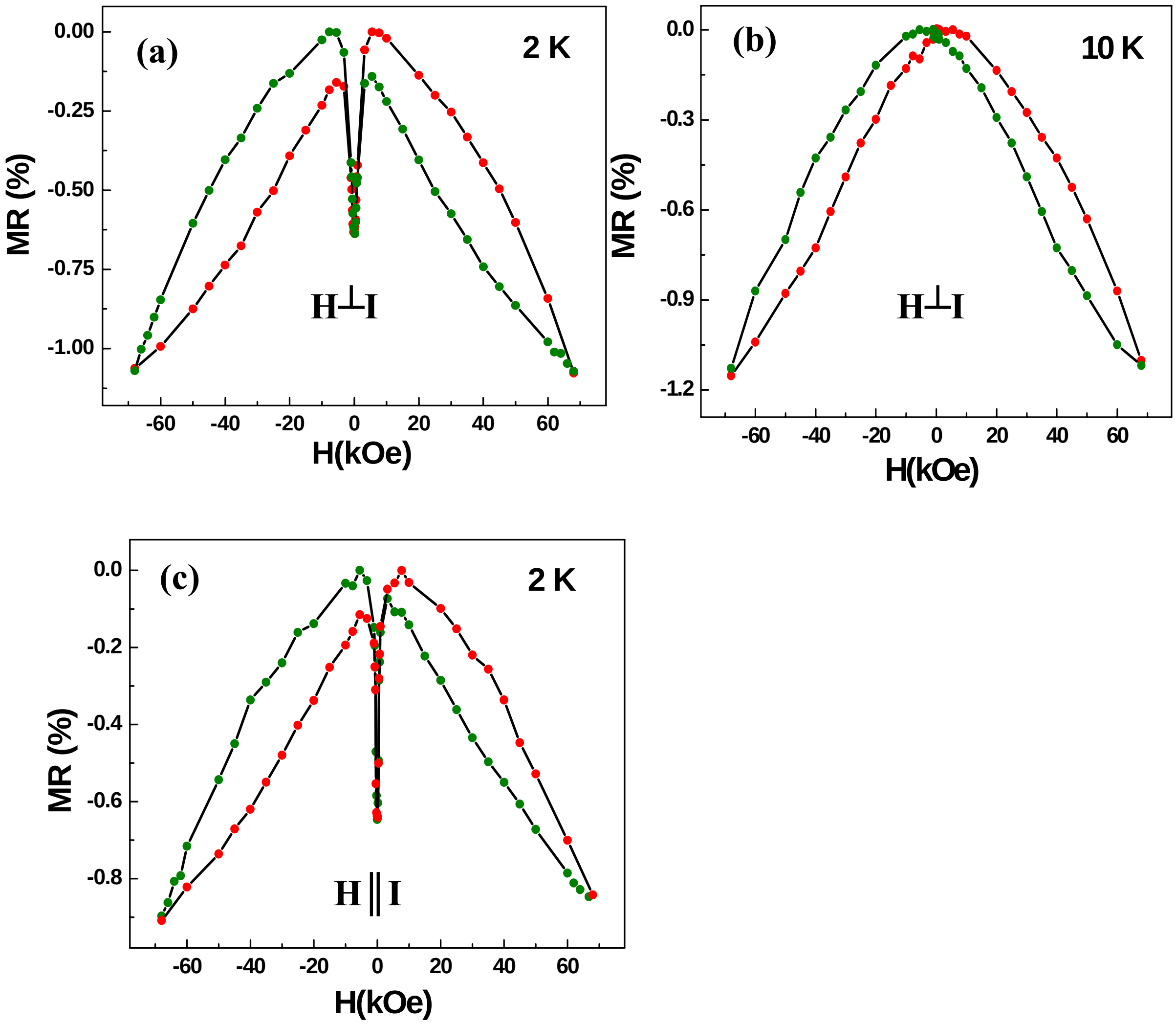

Figure 7-7. MR behavior of the $Fe_{41}Pt_{59}$ multi-layered system in the perpendicular and in-plane orientations at 2 K and 10 K.

7.5 Conclusions

The MR behavior of an epitaxial $Fe_{50}Pt_{50}$ thin film with a bead-like microstructure was studied. A negative MR was observed in a temperature range of 10 to 300 K. The MR behavior was studied in two orientations: field perpendicular to thecurrent and field parallel to the current. The maximum MR at room temperature in perpendicular orientation was 0.57 %. The MR loops showed hysteretic behavior with maximum resistance occurring at H_c. The values of coercivity in the MR and MH measurements were consistent. The presence of MR in the FePt system was attributed to thin domain walls, whose thickness is comparable to spin diffusion lengths. The negative MR effect was explained based on spin and domain wall dependent electron scattering.

References

1. K. Barmak, J. Kim, L.H. Lewis, K.R. Coffey, M.F. Toney, A.J. Kellock, and J.U. Thiele, J. Appl. Phys. **98**, 033904 (2005).
2. D. Weller, A. Moser, L. Folks, M. E. Best, W. Lee, M.F. Toney, M. Schwickert, J. U. Thiele, and M.F. Doerner, IEEE Trans. Magn. **36**, 10 (2000).
3. S. Ishio, T. Yoshino, H. Saito, T. Suzuki, and K. Ohuchi, J. Magn. Magn. Mater. **239**, 217 (2002).
4. Z. Zhang, K. Kang, N. Omoto, and Tsuzuki, IEEE Trans. Magn. **39**, 2827 (2003).
5. Y. Yu, U. Ruediger, A.D. Kent, R.F.C. Farrow, R.F. Marks, D. Weller, L. Folks, and S. S. P. Parkin, J. Appl. Phys. **87**, 6854 (2000).
6. J. Narayan and B. C. Larson, J. Appl. Phys. **93**, 278 (2003).
7. G. R. Trichy, D. Chakraborti, J. Narayan, and J. T. Prater, J. Phys. D: Appl. Phys. **40**, 7273 (2007).
8. P. Allia, F. Celegato, M. Coisson, P. Tiberto, F. Vinai, F. Albertini, F. Casoli, and S. Fabbrici, J. Magn. Magn. Mater. **316**, e35 (2007).
9. U. Ruediger, J. Yu, L. Thomas, S. S. P. Parkin, and A. D. Kent, Phys. Rev. B **59**, 11914 (1999).
10. L. Berger, J. Appl. Phys. **49**, 2156 (1978).

8 Summary

This work demonstrates that the epitaxial c-axis oriented FePt system can be used as a magnetic media for ultra-high density storage applications. Significantly, we showed that epitaxial FePt can be integrated with Si (100). This holds tremendous future promise, because Si is the base material of the semiconductor industry and its usage facilitates potential integration of our magnetic structures with the present day microelectronic devices. Effectiveness of the TiN template to control c-axis growth and induce $L1_0$ order in the FePt system was demonstrated. Extensive XRD and TEM analysis was done to study the epitaxy and $L1_0$ order in the FePt system. The following epitaxial relationship was obtained: FePt (001) <001‖TiN (100) <001>‖Si (100) <001>. Growth of the high misfit FePt/TiN/Si(100) heterostructure was accomplished by domain matching epitaxy. The 9.5 % misfit strain between FePt and TiN was accommodated by alternating 10/9 and 11/10 domains with a frequency factor of 0.547.

The variation of coercivity with microstructure for the epitaxial FePt system was studied in detail. FePt was synthesized both as continuous thin films and individual discrete nanoparticles. The microstructure was progressively varied from a 9 nm nanoparticle system to a 30 nm thick continuous thin film. The FePt islands were formed by self assembly and follow the 3D Volmer-Weber kind of growth mode. For longer deposition times the nanodots merged to form continuous thin films. Magnetic hysteresis measurements showed that all the samples were predominantly perpendicularly magnetized with higher coercivity, squareness and remanence when compared to the in-plane loops. Within the nanoparticle regime coercivity increased with increase in particle size. The highest coercivity of 13,500 Oe was obtained for a bead-like microstructure, when the individual nanoparticles just begin to merge to form a continuous thin film. The continuous thin film showed the smallest coercivity because of its multi-domain state and lack of defects or pinning sites. The best microstructure in terms of magnetic storage was the 18 nm sized nanoparticle system, with a perpendicular coercivity of 10,000 Oe. A storage capacity of 1 Terabit/in^2 can be realized for this system, if we assume one bit of information to be stored in each nanoparticle. All the samples studied showed perpendicular hysteresis loops with remarkable squareness (≥ 0.95). Such systems are ideal for magnetic storage because they show two opposite states of magnetization that switch at well defined fields. It was found that the coercivity of the FePt system can be controlled via the composition. For the 18 nm system, the perpendicular coercivity was decreased from 10000 Oe to 3200 Oe by changing the composition from $Fe_{50}Pt_{50}$ to $Fe_{41}Pt_{59}$. A negative magnetoresistance (MR) of 0.57% was observed at room temperature for the $Fe_{50}Pt_{50}$ bead-like thin film system. The MR loops showed hysteretic behavior with maximum resistance at H_c. The values of coercivity in the MR and MH measurements were consistent. The presence of MR in the FePt system was attributed to thin domain walls, whose thickness is comparable to spin diffusion lengths. The negative MR effect was explained based on spin and domain wall dependent electron scattering.

9 Suggestions for future work

The following ideas can be pursued as an extension to this study.

1. Further, optimization of the FePt nanoisland size and shape (self assembly) by controlling experimental parameters such as laser energy density, repetition rate and substrate temperature.
2. A thin film of FePt (1-3 nm thick) can be deposited at a lower temperature. The continuous film will break-up to form islands when annealed at a higher temperature. This effect can be used as an alternative processing route and can be studied in detail.
3. At a low temperature of 2 K, the multi-layered FePt system showed both positive and negative MR behavior (see chapter 7). More experiments and analysis need to be performed to explain this behavior.